THESIS FOR THE DEGREE OF DOCTOR OF PHILOSOPHY

At the heart of Quantum Materials:

Magnetism as a means and an end from a muon perspective

Konstantinos Papadopoulos

Department of Physics
Chalmers University of Technology
Gothenburg, Sweden 2024

At the heart of Quantum Materials: Magnetism as a means and an end from a muon perspective

Konstantinos Papapdopoulos
ISBN 978-91-8103-021-1

Doktorsavhandlingar vid Chalmers tekniska högskola
Ny serie nr 5479
ISSN 0346-718X

Department of Physics
Chalmers University of Technology
SE-412 96 Gothenburg
Sweden
Telephone +46 (0)31 772 1000

This work was funded by the Swedish Research Council (VR) through a Starting Grant (Dnr. 2017-05078) and the Area of Advance-Materials Science of Chalmers University of Technology.

Printed by Chalmers Reproservice
Gothenburg, Sweden 2024

Abstract

Functional materials are at the center of solid state physics research and technological innovation in our era. In order to create (semi)autonomous, high precision and lightning-fast devices it is necessary to explore, modify and control the intrinsic properties of matter. This thesis focuses on quantum materials with strongly correlated physical entities, where properties may also be defined by geometry and can not thoroughly be described by classical physics. The magnetic and electrical properties of these materials are predominantly studied at an atomic level in order to understand the evolution of interactions between electron spins, charges and structure as well as dependencies from external parameters. Magnetic interactions are considered not only in the research subjects of this thesis but also in the employed experimental technique. Therefore, Chapter 2 is dedicated to a brief introduction in certain aspects of magnetism.

Positive muon spin rotation, relaxation and resonance (μ^+SR) is the principal experimental technique used in the presented studies. In essence this technique employs elementary particles called muons as magnetic probes in the studied samples. The reaction of muons to the local magnetic fields, which arise from the electronic structure or the atomic nuclei of solids, conveys direct or indirect information of phase transitions, dynamics or specific processes in the materials. In Chapters 3 and 4 the background and practicalities of the μ^+SR technique will be elaborated to a sufficient extend that covers the scope of this thesis.

The presented research encompasses a diverse array of materials with distinct structural characteristics and magnetic or electronic properties, which have been investigated utilizing μ^+SR and complementary experimental techniques. A detailed introduction to each material and a summary of the experimental results can be found in Chapter 5.

Concerning magnetic materials, the studies comprised $LaSr_{1-x}Ca_xNiReO_6$ and $CrCl_3$ polycrystalline samples, as well as CoFeB/Ru/Pt superstructures. In the case of the double perovskite, three-dimensional magnet $LaSr_{1-x}Ca_xNiReO_6$, a dense and dilute magnetic phase were discovered above the critical temperature of magnetic order. The difference in size between the Sr and Ca cations alters the magnetic interaction between Ni and Re sub-lattices and as a result, the magnetically ordered phase. The magnetic phase diagram of the layered, two-dimensional magnet $CrCl_3$ was similarly studied. The μ^+SR analysis identified a dynamic layered antiferromagnetic ordering phase followed by a short range ordered ferromagnetic phase. Both studies exemplify the substantial advantage of measurements in zero external magnetic field with μ^+SR. An alternative configuration with low energy μ^+SR and adjustable muon implantation depth was employed to study the magnetic phases of multilayered CoFeB/Ru/Pt superstructures. A magnetic-skyrmion phase was identified and the persisting dynamics down to 50 K were studied in relation to an unexpected weak dependence on externally applied magnetic fields.

Regarding ionic motion in non-magnets, a customized muon study was conducted on hybrid, organic-inorganic perovskite $(CH_3NH_3)PbX_3$ (X=Br, Cl) single crystals, which constitute promising photovoltaic materials. Molecular fluctuations were studied across the structural phases of the materials with and without illumination. μ^+SR results in these two environments indicate that molecular fluctuations and the type of halide ion are defining parameters on structural stability and carrier lifetimes, both of which are essential in solar cell applications.

Keywords: magnetism, ion dynamics, phase transitions, muon spectroscopy, correlated systems, quantum materials.

Sammanfattning

Funktionella material är i centrum för forskningen och tekniska innovationen inom fasta tillståndets fysik i vår tid. För att skapa (semi)autonoma, hög precision och blixtsnabb enheter är det nödvändigt att utforska, modifiera och kontrollera materians inneboende egenskaper. Denna avhandling handlar om kvantmaterial med starkt korrelerade fysiska enheter, där egenskaperna kan också definieras av geometrin och kan inte grundligt beskrivas av klassisk fysik. De magnetiska och elektriska egenskaperna hos dessa material studeras huvudsakligen på atomnivå för att förstå hur interaktionerna utvecklas mellan elektronspinn, laddningar och struktur samt beroenden av externa parametrar. Magnetiska interaktioner beaktas inte bara i forskningspersoner i denna avhandling används även av den experimentella tekniken. Kapitel 2 är därför avsett för ett introduktion i vissa aspekter av magnetism.

Positiv myonspinn rotation, avslappning och resonans (μ^+SR) är den huvudsakliga experimentella tekniken som användes i de presenterade studierna. I huvudsak använder denna teknik elementarpartiklar kallade myoner som magnetiska sonder i de studerade proverna. Myoner interagerar med de lokala magnetfälten, som beror på den elektroniska strukturen eller av kärnan av fasta ämnen, ger direkt eller indirekt information om fasövergångar, dynamik eller specifika processer i materialen. I kapitlen 3 och 4 beskrivs bakgrunden och de praktiska delarna av μ^+SR-tekniken.

Den aktuella forskningen omfattar ett brett spektrum av material med tydliga strukturella egenskaper och magnetiska eller elektroniska egenskaper, som har undersökts med hjälp av μ^+SR och kompletterande experimentella metoder. En detaljerad introduktion till varje material och en sammanfattning av försöksresultaten finns i kapitel 5.

När det gäller magnetiska material omfattade studierna $LaSr_{1-x}Ca_xNiReO_6$ och $CrCl_3$ polykristallina prover och överbyggnader av CoFeB/Ru/Pt. För den tredimensionell perovskit magneten $LaSr_{1-x}Ca_xNiReO_6$, upptäcktes en tät och utspädd magnetisk fas över den kritiska magnetiska temperaturen. Skillnaden i storlek mellan Sr- och Ca-katjoner förändrar den magnetiska interaktionen mellan Ni och Re jonerna och därmed den magnetiskt ordnade fasen. Den magnetiska fas diagram av skiktade, tvådimensionella magneten $CrCl_3$ studerades på liknande sätt. μ^+SR analys identifierade en dynamisk skiktad antiferromagnetisk fas följt av en kort ordnat ferromagnetisk fas. Båda undersökningarna visar på den betydande fördelen med mätningar i miljö fri från magnetfält med μ^+SR. En alternativ konfiguration med låg energi μ^+SR och justerbart myonimplantationsdjup användes för att studera de magnetiska faserna hos de flerskiktade överbyggnaderna av CoFeB/Ru/Pt. En magnetskyrmion och en bestående dynamik ner till 50 K studerades i relation till den till ett oväntat svagt beroende av externt pålagda magnetfält.

När det gäller joniska rörelser i icke-magneter genomfördes en anpassad myonstudie på hybrid, organisk-oorganisk perovskit $(CH_3NH_3)PbX_3$ (X=Br, Cl) enkla kristaller, som utgör lovande solcellsmaterial. Molekylära fluktuationer studerades i hela konstruktionsfaserna av materialen med och utan belysning. μ^+SR resultat i dessa två miljöer tyder på att molekylära fluktuationer och typen av halogenidejon definierar parametrar för strukturell stabilitet och bärvågens livslängd, vilka båda är väsentliga i solcellstillämpningar.

Acknowledgements

As I reflect on the years of my PhD studies, I see a collage of timeless moments that have unfolded along a winding trail from start to finish. It is these moments and the people who have been a part of them that I would like to pay tribute to. These people include those that picked up this trail with me from the beginning, those I have met along the way, and those who have crossed my path.

First of all, I would like to thank my supervisors, Yasmine Sassa, Lars Börjesson and Martin Månsson for giving me the opportunity, the gear and the freedom to walk the tracks of this research project. In times the path was bumpy and difficult to tread but I believe determination and our shared core values helped me to push forward. Lars, thank you for our discussions on the project and science in general. I felt inspired and encouraged after every single one of our meetings. Martin, I consider you as a role-model in problem-solving and fast, effective decision-making. Dear Yasmine, thank you for your honesty, your understanding and for always being open to a discussion. As I told you before, during this journey you helped me not only to develop the factual knowledge needed for this project but also a set of skills that I am sure will be useful in my future. For this I will be forever grateful.

In every step of the way, I was certain I had the support of two excellent scientists, Ola Kenji Forslund and Jun Sugiyama. Their comments have always given me insight and clarity into μSR results and the conclusions of my subjects. All I needed to do was simply ask, which I wish I would have done more frequently. Ola, I am grateful for the time spent together in and out of the framework. I am glad to call you a friend and I hope we stay connected since then, now and beyond.

During all beamtimes and meetings I wish you, Elisabetta Nocerino, were always present. You were the glue that helped us all work together. Even in chaotic COVID-19 beamtimes we pulled through, and I am sure you have the strength to tackle every obstacle. Nami Matsubara thank you for the beamtimes spent together. Our effortless communication and your knowledge in crystallography were always very helpful. Gediminas Simutis it was always a pleasure to discuss with you. Your insightful comments had furthered my understanding of μSR results and I wish we could collaborate more. Gaia di Berardino and Anton Zubayer thank you for the support and long days and nights spent together at PSI and J-PARC. Neither earthquakes nor a pandemic could stop us! Ugne Miniotaite, Rasmus Palm and Frank Elson thank you for being the workforce in our μSR experiments from distance. Every member of the team was ready to actively support and cover each other.

The teamwork for these projects would be handicapped without the support from all beamline scientists from ISIS, PSI and TRIUMF. Stephen Cottrell and Koji Yokoyama thank you for setting up the hybrid perovskite experiment at ISIS. Our discussions during that time and during the preparation of the manuscript were pivotal for this publication. Daniel Andreica, Chennan Wang, Ritu Gupta and Rustem Khasanov your instructions helped me acquire the skills and experience to conduct muon experiments at PSI. Donald Arseneau, Bassam Hitti and Gerald Morris, thank your for being always on call when we had an issue and always came up with solutions. My time in TRIUMF had been most didactic towards the particulars of the μSR instrumentation.

Nicolas Reyren, Marisa Medarde, Andreas Suter and Thomas Prokscha you have sacrificed your time to help and support me with my thin film and double perovskite projects, and yet we have not really met each other. I wish I will sometime get the opportunity to meet you in person. Alexei Kalaboukhov, Peter Svedlindh, Lars Öhrström and Francoise

Amombo Noa gave me guidance and support with magnetometry and XRD measurements. I was at least able to meet, discuss with you and thank you properly.

Back to base in Chalmers, the Division of Material Physics [(K)MF] was always a calm and friendly environment. I want to thank my examiner Aleksandar Matic, for your pragmatic approach on every issue, and Ezio Zanghellini, our well of resources and intel in the lab. I would also like to thank all of my colleagues and office mates. It always amazes me when I meet people from different cultural backgrounds with whom I share a point of view. The appropriate time for coffee and lunch is not one of them.

To my dearest parents, John and Rena in Athens, I am grateful for always supporting my decision, even if you don't like it. It's hard to be away from you, especially through difficult times. I'm looking forward to seeing you soon. Luckily I have my other half here with me. Dimitra you are my rudder and you care for me more than I care for myself sometimes. I am sorry for my ramblings about magnets and for zoning out in front of the pc. Now, Kalouta and the mountains are calling.

Konstantinos Papadopoulos, Göteborg, 2024/02/28

Figure 0.1: Beamtime at J-PARC featuring (from left to right) Prof. Yasmine Sassa, Konstantinos Papadopoulos, Dr. Nami Matsubara, Anton Zubayer, Dr. Titus Masese, Dr. Elisabetta Nocerino, Dr. Ola Forslund and Prof. Martin Månsson.

List of Papers

I. **Intertwined magnetic sublattices in the double perovskite compound $LaSrNiReO_6$**

Ola Kenji Forslund, Konstantinos Papadopoulos, Elisabetta Nocerino, Gerald Morris, Bassam Hitti, Donald Arseneau, Vladimir Pomjakushin, Nami Matsubara, Jean-Christophe Orain, Peter Svedlindh, Daniel Andreica, Somnath Jana, Jun Sugiyama, Martin Månsson, and Yasmine Sassa
Physical Review B, 102, 144409 (2020)

II. **Influence of the magnetic sublattices in the double perovskite $LaCaNiReO_6$**

Konstantinos Papadopoulos, Ola Kenji Forslund, Elisabetta Nocerino, Fredrik O.L. Johansson, Gediminas Simutis, Nami Matsubara, Gerald Morris, Bassam Hitti, Donald Arseneau, Peter Svedlindh, Marisa Medarde, Daniel Andreica, Jean-Christophe Orain, Vladimir Pomjakushin, Lars Börjesson, Jun Sugiyama, Martin Månsson and Yasmine Sassa
Physical Review B, 2022, 106.21: 214410

III. **Photophysical ion dynamics in hybrid perovskite $MAPbX_3$ (X=Br, Cl) single crystals**

Konstantinos Papadopoulos, Ola Kenji Forslund, Stephen Cottrell, Koji Yokoyama, Pabitra K. Nayak, Francoise M. Amombo Noa, Lars Öhrström, Elisabetta Nocerino, Lars Börjesson, Jun Sugiyama, Martin Månsson, and Yasmine Sassa
Advanced Physics Research, 2024, 2300120

IV. **Magnetic phases of a skyrmion host candidate superlattice CoFeB/Ru/Pt probed with low energy muon-spin spectroscopy**

Konstantinos Papadopoulos, Ola Kenji Forslund, Yuqing Ge, Lars Börjesson, Fernando Ajejas, Vincent Cros, Zaher Salman, Nicolas Reyren, Thomas Prokscha, and Yasmine Sassa
Manuscript

V. **Spin dynamics in the Van der Waals magnet $CrCl_3$**

Ola Kenji Forslund, Konstantinos Papadopoulos, Elisabetta Nocerino, Gaia Di Berardino, Chennan Wang, Jun Sugiyama, Daniel Andreica, Alexander N. Vasiliev, Mahmoud Abdel-Hafiez, Martin Månsson, Yasmine Sassa
Manuscript

Contribution Report

I. I performed the μ^+SR experiment with the assistance and support of the co-authors. I analyzed the data with OKF, discussed the results and conclusions of the μ^+SR and magnetometry measurements and assisted in the preparation of the manuscript.

II. I planned and performed the μ^+SR experiments with the assistance and support of the co-authors. PS, MM and I performed the magnetometry measurements. I analyzed all data with the support of OKF, YS and JS. I discussed results with co-authors and authored the submitted manuscript.

III. I planned and performed the μ^+SR, calorimetry and X-ray diffraction experiments with the assistance and support of the co-authors. I analyzed all the data and discussed the possible interpretations of the results with OKF and YS. I prepared the manuscript together with OKF and I implemented the comments of all the co-authors for submission.

IV. I analyzed the μ^+SR experimental data and discussed the results with co-authors. I prepared the original manuscript and, with support from OKF, YG and NR, subsequent versions of it.

V. I executed the μ^+SR experiments with the assistance of EN and GDB. I prepared a preliminary analysis and discussed with OKF the experimental results, interpretations and conclusions of the manuscript.

Papers not included in the thesis

I. **Magnetism and ion diffusion in honeycomb layered oxide $K_2Ni_2TeO_6$**

Nami Matsubara, Elisabetta Nocerino, Ola Kenji Forslund, Anton Zubayer, Konstantinos Papadopoulos, Daniel Andreica, Jun Sugiyama, Rasmus Palm, Zurab Guguchia, Stephen P. Cottrell, Takashi Kamiyama, Takashi Saito, Alexei Kalaboukhov, Yasmine Sassa, Titus Masese and Martin Månsson
Scientific Reports 10, 18305 (2020)

II. **Lithium diffusion in LiMnPO4 detected with $\mu^{\pm}$SR**

Jun Sugiyama ,Ola Kenji Forslund, Elisabetta Nocerino, Nami Matsubara, Konstantinos Papadopoulos, Yasmine Sassa, Stephen P. Cottrell, Adrian D. Hillier, Katsuhiko Ishida, Martin Månsson and Jess H. Brewer
Physical Review Research 2, 033161 (2020)

III. **Cation Distributions and Magnetic Properties of Ferrispinel $MgFeMnO_4$**

Nami Matsubara, Titus Masese, Emmanuelle Suard, Ola Kenji Forslund, Elisabetta Nocerino, Rasmus Palm, Zurab Guguchia, Daniel Andreica, Alexandra Hardut, Motoyuki Ishikado, Konstantinos Papadopoulos, Yasmine Sassa, and Martin Månsson
Inorganic Chemistry 59, 24, 179790-17980 (2020)

IV. **Structural Transition with a Sharp Change in the Electrical Resistivity and Spin–Orbit Mott Insulating State in a Rhenium Oxide, $Sr_3Re_2O_9$**

Daisuke Urushihara, Toru Asaka, Koichiro Fukuda, Masanobu Nakayama, Yuki Nakahira, Chikako Moriyoshi, Yoshihiro Kuroiwa, Ola K. Forslund, Nami Matsubara, Martin Månsson, Konstantinos Papadopoulos, Yasmine Sassa, Kazuki Ohishi, Jun Sugiyama, Yoshitaka Matsushita, and Hiroya Sakurai
Inorganic Chemistry 60, 2, 507-514 (2021)

V. **Multiple unconventional charge density wave transitions in $LaPt_2Si_2$ superconductor clarified with high-energy X-ray diffraction**

Elisabetta Nocerino, Irene Sanlorenzo, Konstantinos Papadopoulos, Marisa Medarde, Jike Lyu, Yannick Maximilian Klein, Arianna Minelli, Zakir Hossain, Arumugam Thamizhavel, Kim Lefmann, Oleh Ivashko, Martin von Zimmermann, Yasmine Sassa and Martin Månsson
Communications Materials 4, 77 (2023)

Table of Contents

Chapter 1

Introduction

Archaeological discoveries have traced the development of the first alloys and compound materials beyond 4000 BCE. The construction of iconic structures such as the pyramids and the infrastructure of the Roman Empire relied on the use of lime mortar [1, 2], while bronze defined an entire historical era [3]. A reshaping of the world was sparked by the invention of gunpowder by Chinese monks in the 9th century CE [4]. In 1876, F. Braun demonstrated his lead sulfide semiconductor point-contact rectifier, paving the way for the current Digital Age [5]. These examples illustrate that human societies have evolved and adapted through a keen interest in materials and craftsmanship [6], ultimately leading to deeper paths of understanding the microscopic nature of matter and the interactions that define its properties.

At first a collection of independent studies, Solid State Physics became a distinct field in the 1940s, promoted by F. Seitz's work *Modern Theory of Solids* [7], which focused on the application of the discoveries in atomic physics to explain the properties of materials. Solid materials can be either amorphous or crystalline. Crystals are composed of a structured arrangement of one or more atoms, called the basis, which is periodically repeated in a lattice [8]. The symmetries respected by such systems and their internal interactions reflect many of the properties of these materials. When a system is altered, typically by a change in temperature, pressure, an applied field, an implanted particle or modifications to the basis, it can transition between more symmetrical disordered phases and ordered phases where specific symmetries are broken. A typical example is the phase transition of water, where an ordered solid ice state with lower symmetry is established below the melting temperature [Fig. 1.1]. A similar case is the formation of an ordered magnetic structure in a solid. Each of these ordered phases is characterized by an appropriate order parameter that describes which of the various lower symmetries the material has selected. Furthermore, within these broken-symmetry phases, there may exist regions of topological defect where the symmetry is restored. These regions play an important role in determining the dynamics of the system.

The establishment of the quantum theory of solids with the concept of electron wave functions in a periodic potential by F. Bloch [9] has led to the development of various models for the electronic structure in crystalline solids. If independent electrons are considered, approximations such as those suggested by D. R. Hartree and V. Fock [10], provide an adequate description of the electronic structure. However, the dynamic coupling between lattice, charge, spin and orbital degrees of freedom cannot be overlooked, since they may provide further breaking of symmetries, leading to new phases. Strongly correlated systems often exhibit complex phase diagrams with a multitude of electronic and magnetic phases, which stem from a delicate balance between various interactions, such as those found in the extensive family of transition-metal complexes [11]. These correlations can be

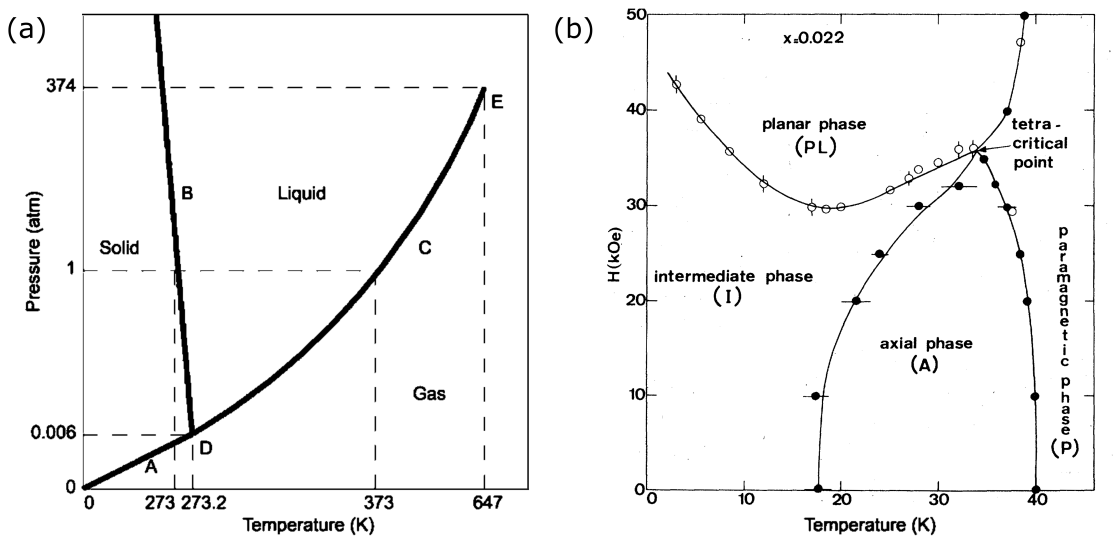

Figure 1.1: (a): The phase diagram of water. The high symmetry of the liquid phase is broken when water crosses over to the ordered solid state (B), where symmetry operations are defined by the structure of the crystal lattice. In contrast, no change in symmetry is observed in the liquid-gas transition and beyond the critical point (E) only density distinguishes the two phases. **(b):** The magnetic phase diagram of $K_2Mn_{1-x}Fe_xF_4$ for a specific iron concentration (x), as a function of temperature and applied magnetic field. The randomly oriented magnetic moments of the paramagnetic phase (P) become long-range ordered in magnetic phases with lower symmetry. Adapted from [17].

so strong that transitions from a metallic to insulating state or other complex states (e.g superconductivity) may occur [12, 13]. The influence of quantum effects remains prominent over a wider range of energy and length scales and is enhanced in lower dimensions, as in the case of graphene and low-dimensional magnets [14, 15]. Moreover, strongly interacting electrons can give rise to collective excitations known as quasiparticles. In magnetically ordered systems, collective excitations form magnons and their topologically protected relatives, such as magnetic skyrmions, merons, etc. Both are of great interest in the field of information storage and processing, due to their energy-efficient control and manipulation [16]. It is evident now that correlations between different degrees of freedom in solids has led to the formation of a diverse group of multifunctional materials with new physical properties, collectively known as 'quantum materials'. The analysis of their emerging phases and comprehension of the underlying interactions that drive them poses a great challenge in current Solid State Physics research, but their unprecedented capabilities have the potential to revolutionize energy and information technologies.

Correlated many-body systems can be analyzed using various theories, models and experimental data, but misinterpretations are common in complex cases. A.C. Doyle and R. Coase appear to complement each other in this struggle; "*It is a capital mistake to theorize before one has data*", yet "*if you torture the data long enough, it will confess to anything*". There are numerous probing techniques available for studying crystalline solids, each of which interacts with the sample through externally controlled parameters and collects data within a specific range of physical quantity scales. In order to effectively study a material, it is necessary to consider the probe interaction and its sensitivity boundaries.

The primary technique employed in the experimental studies presented in this thesis is positive muon spin rotation, relaxation, and resonance (μ^+SR) [18]. The working principle of μ^+SR is the implantation of 100% spin-polarized muons in matter, which interact with local internal magnetic fields of electronic or nuclear origin. The results represent volume fractions in the material, however they lack element specificity. Depending on the nature of the material sample and the targeted physical property a specific μ^+SR experimental configuration is selected. Muons function as magnetic probes. However, apart from magnetic samples the presented studies also include a nonmagnetic semiconducting material, which demonstrates the ability of μ^+SR to also study ion dynamics. All measurements were contacted either in true zero magnetic field or under applied field, in a wide temperature range down to 2 K. The time resolution of the technique ranges from 10^{-5} to 10^{-12} s. In order to verify and support the μSR results, numerical calculations were performed, as well as supplementary or complimentary measurements with various techniques, probing the samples in different length and time regimes.

1.1 Thesis outline

The topic of research in this thesis is the emergence of phases in a collection of distinct samples and in response to variations in temperature, externally applied magnetic field, or chemical substitution. The static and dynamic processes of these systems were primarily studied with a magnetic probe, by the use of the μSR technique. In fact, the majority of the studied materials are magnetic. Therefore, the following chapters are mainly focused on magnetism and the experimental approach.

In Chapter 2, fundamental concepts of magnetism and correlation effects are introduced at both the microscopic and macroscopic levels, which are often used to describe the internal processes and physical phenomena that occur in the studied systems.

Chapter 3 focuses on the working principles of μSR and the experimental procedure. Furthermore, a selection of experimental results is presented and their treatment is discussed.

Chapter 4 provides an overview of the various μSR experimental set-ups and their specific details.

Chapter 5 consists of sections dedicated to each study presented in the appended papers. Each section begins with an introduction that establishes the background and motivation for the research, followed by a summary of the primary experiment and the main results.

Chapter 6 concludes the thesis with a brief reflection on the research process, followed by highlights of the presented articles with some recommendations for future studies.

Chapter 2

Basic Concepts and Theory

This chapter focuses on selected concepts in magnetism. These will provide the reader with further insight into the experimental findings presented in this study, which primarily involve magnetic materials and employ the magnetic probe of spin-polarized muons. The following discussion will focus on fundamental quantities of a system and their interactions, as perceived in a microscopic level. Along its course, we will touch upon cases of correlated degrees of freedom and how they may influence the state of a system. A selection of magnetic interactions that promote a solid material towards a magnetically ordered state will be presented. Finally, a magnetic phase will be viewed collectively, as manifested in a life-size material.

2.1 Origins of magnetism

The fundamental quantity of magnetism responsible for yielding a net magnetization in a material is the magnetic moment. Initially, let us suppose an individual atom and examine certain of its internal and external interactions. From classical electrodynamics, the magnetic dipole moment created from the orbital motion of an electron around a nucleus is defined as $\boldsymbol{\mu_L} = -\frac{|e|}{2m}\mathbf{L}$. Bohr in his quantum model [19] only accepted orbitals with integer multiples of $\hbar$ for the angular momenta. The quantum mechanical description proposes a volume in space where the electron has a probability to be found, instead of a fixed orbital. The solution of the Schroedinger equation determines discrete values of $\mu_L = -\frac{|e|}{2m}\sqrt{l(l+1)}\hbar$ and its z component $\mu_{Lz} = -\frac{|e|}{2m}m_l\hbar$, with quantum numbers l,m_l depending on the electronic state [Fig. 2.1 (a)]. The value $m_l = 1$ corresponds to the magnetic moment at the ground state, called *Bohr's magneton*: $\mu_B = \frac{e\hbar}{2m} = 9.27 \cdot 10^{-24} J/T$. Similar to the classical magnetic moment, a *Larmor precession* with a characteristic *Larmor frequency* will be caused by a present magnetic field. However, the purely quantum-mechanical, intrinsic angular momentum of an electron, called spin, is also a fundamental source of magnetism. The spin of an electron creates correspondingly a magnetic moment $\boldsymbol{\mu_S} = -g_S\frac{|e|}{2m}\mathbf{S}$. The total angular momentum of an electron can now be defined as $\mathbf{J} = \mathbf{L} + \mathbf{S}$ and the generated magnetic moment as $\boldsymbol{\mu_J} = -g_J\frac{|e|}{2m}\mathbf{J}$, where g_J is a proportionality constant called *Lande factor*. The total angular momentum will precess around an externally applied magnetic field, also with a quantized projection along the field direction [Fig. 2.1 (b)].

Let us first consider the simplest case of a hydrogen atom with only one electron surrounding the nucleus. The ground and excited electronic eigenstates will be described by orbitals of different energy, size, shape and coordination depending on the n, l and m_l quantum numbers [Fig. 2.1 (c)]. In each volume there exists a probability density function

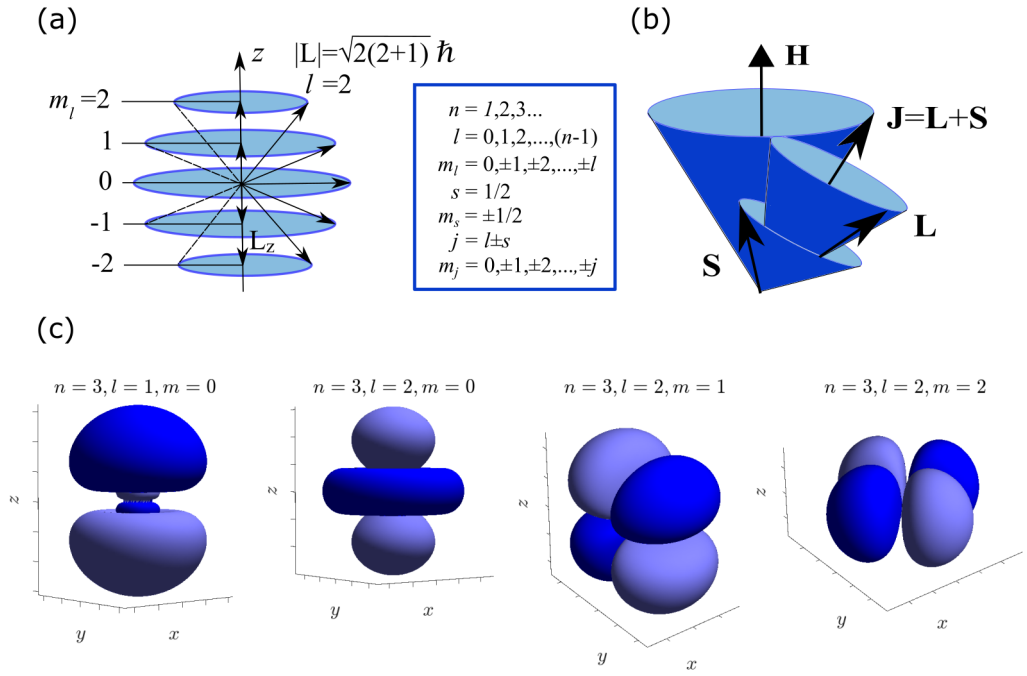

Figure 2.1: **(a):** The orbital angular momentum of an electron is quantized (l), as well as its projection along the z direction (m_l). From the uncoupled basis the states are specified by the quantum numbers (n, l, m_l, m_s). **(b):** In L-S coupling the orbital **L** and spin **S** angular momentum are combined to produce the total angular momentum **J**. The projection of **J** along z is also quantized. From the coupled basis, the good quantum numbers are now (n, l, j, m_j). When an external magnetic field is present, the magnetic energy contribution is proportional to J_z. Adapted from [20]. **(c):** Selected hydrogen-like orbitals. The lobes represent the electron cloud and the colors, a change of the wavefunction sign.

of finding the electron in an elementary volume $d\tau$. In many-electron atoms, where electronic shells are partially filled, the electronic ground state can be effectively approximated by the L-S coupling, according to Hund's rules and Pauli's exclusion principle [21, 22]. The atoms in question are lightweight and the strength of the spin-spin and orbit-orbit coupling surpasses that of the spin-orbit coupling. For heavier atoms, as in the case of 5d, 6d transition metals and rare earth elements, another coupling scheme, namely j-j coupling, describes electronic arrangements in better agreement with experimental results. In the *j-j* scheme, spin-orbit coupling (SOC) is added, splitting the L and S states into a number of levels with different J, known as *fine structure*. This interaction takes the form:

$$H_{LS} = -\boldsymbol{\mu_S} \cdot \mathbf{B_l} = \lambda \sum_i \mathbf{L}_i \cdot \mathbf{S}_i \tag{2.1}$$

, where λ is the coupling constant and $\mathbf{B_l}$ the effective magnetic field generated by the orbiting electrons.

So far we have considered an isolated atom, but a real material consists of a number of particles close to the Avogadro number and it can be subjected to various forces from its environment. When an external magnetic field **B** is imposed on the atomic system,

the atom will respond depending on whether or not it possesses a magnetic moment. If unpaired electrons exist, there will be a net paramagnetic moment which will try to align with **B** yielding an interaction:

$$H_P = -\boldsymbol{\mu} \cdot \mathbf{B} = \boldsymbol{\mu_B}(\mathbf{L} + g\mathbf{S}) \cdot \mathbf{B} \tag{2.2}$$

This paramagnetic response creates an energy splitting of the original orbitals, known as *Zeeman effect* [23]. However, the splitting of states depends also on SOC and therefore the relative strength between the H_{LS} and H_z interactions. If all electronic shells are filled there exists no net magnetic moment, however the applied field induces a diamagnetic moment that resists magnetization. The interaction is described as:

$$H_D = \frac{e^2}{8m_e} \sum_i (\mathbf{B} \times \mathbf{r}_i)^2 \tag{2.3}$$

, where $\mathbf{r_i}$ represent the electron positions in the atom. The diamagnetic effect is a weak effect but present in all materials.

In a crystal, ions also interact with the electrostatic environment created by their neighboring ligands [24, 25]. Transition metal coordination complexes, such as those featuring an octahedral framework (Papers I,II,V), are typical cases to consider. This collection of interactions at each ion's position ($\mathbf{r}$) results in the presence of an non-spherical electrostatic field known as the crystal field:

$$V(\mathbf{r}) = \int \frac{\rho(\mathbf{r'})}{|\mathbf{r} - \mathbf{r'}|} d\mathbf{r'} \tag{2.4}$$

, where $\rho(\mathbf{r'})$ the charge density of the surrounding electrons. The degeneracy of orbitals with a given value of orbital angular quantum number is removed with the application of a crystal field which depends on the symmetry of the local environment. In the case of the octahedral transition metal complexes, the *d*-orbitals are split into a three-fold degenerate t_{2g} state of lower energy, and double degenerate e_g state of higher energy. The e_g orbitals are presented in Figure 2.1(c) for $(n = 3, l = 2, m = 0, 2)$. The three t_{2g} orbitals point between the x, y, z axes as illustrated for the $(n = 3, l = 2, m = 1)$ case.

Eventually, the Hamiltonian which describes an atom can be described as its original Hamiltonian with added perturbations considering the previous interactions as:

$$H_{per} = H_o + H_{LS} + H_P + H_D + H_{cr} \tag{2.5}$$

The first term is a sum of the kinetic, potential and Coulomb energy of the Z electrons in the atom. The second term accounts for the spin-orbit interaction. The third term includes the *Zeeman* interactions with the external magnetic field. The fourth term describes the diamagnetic effect. The fifth term describes the crystal field potential energy. The competition between momentum coupling, the Zeeman effect and the crystal field (CF) interaction determines the ground state. In rare earths, where SOC is larger than CF, Hund's third rule is valid. In 4d and 5d transition metals SOC and CF are comparable and the arrangement of state is the result of an aggregate score. If CF dominates, then Hund's rules cannot be applied. The L-S coupling is broken up and the crystal field splitting of the L levels results in a time averaged orbital momentum $< L >= 0$. This phenomenon is known as orbital quenching and is typically observed in 3d transition metals [26]. Additionally, a multitude of systems and typically transition metal complexes may distort their geometry in order to remove the degeneracy of unequally occupied orbitals and lower their overall energy. This coupling between orbitals and lattice distortions is

called the Jahn-Teller effect. It can be of static or dynamic nature, and in the case of these distortions acting cooperatively they may drive a macroscopic symmetry lowering in the crystal.

Inside the atomic nucleus, protons and neutrons respectively possess a nuclear spin. The total spin of the nucleus **I** is the vector sum of the nucleon spins. Nucleons have quantum numbers analogous to electrons and follow a set of arrangement rules. The nuclear magnetic dipole moment is $\boldsymbol{\mu_n} = -g_N \frac{|e|}{2m_P}\mathbf{I}$ and its z component $\mu_{nz} = g_n \frac{|e|}{2m_P} m_I \hbar = g_n \mu_{Bn} m_I$. In this case m_P is the proton mass, g_N is the nuclear g-factor and $\mu_{Bn} = 5.049 \cdot 10^{-27} J/T$ the nuclear magneton. The nuclear moment has a ∼2000 times smaller value than the electronic moment due to the larger proton mass. However, certain sensitive techniques such as nuclear magnetic resonance (NMR), Moessbauer spectroscopy and μSR can detect it, therefore even nonmagnetic materials (Paper III) can be studied based on their nuclear moment. The nuclear g-factor may assume positive or negative values, resulting in nuclei exhibiting a magnetic moment either parallel or antiparallel to their spin. This contrasts with electrons, where the magnetic moment is consistently antiparallel to their spin. The nuclear moment also interacts with a field $\mathbf{B_e}$ generated by all electronic magnetic moments, similarly to SOC [22]. The field $\mathbf{B_e}$ is proportional to the total angular momentum **J** and the corresponding hyperfine Hamiltonian can be written as:

$$H_{hf} = A(\mathbf{I} \cdot \mathbf{J}) \tag{2.6}$$

, where A is a constant measuring the strength of the interaction. A new total angular momentum should now be defined as $\mathbf{F} = \mathbf{I} + \mathbf{J}$ and the representation requires two new quantum numbers f and m_f. The presence of the hyperfine interaction drives a splitting of the f states, known as the *hyperfine structure*.

The spin is an important quantum mechanical property of all fundamental particles and crucial in explaining the nature and properties of matter. If we consider a system of N particles in thermal equilibrium, the probability distribution of a particle existing in a particular quantum state as a function of energy, depends on their spin number. The particles that make up matter have half-integer spin, they obey the *Fermi-Dirac* statistics and thus called fermions [27]. Even if the orbital angular momentum is removed, the particles can possess a magnetic moment due to their spin, which is inversely proportional to their mass [Table 2.1] . This fact enables us to perform experiments that involve the spin of muons, electrons and the nuclei, in ways that reveal intrinsic properties of materials.

Particle	Mass	Charge	Spin
u-quark, c-quark, t-quark	2.3 MeV, 1.275 GeV, 173.07 GeV	2/3	1/2
d-quark, s-quark, b-quark	4.8 MeV, 95 MeV, 4.18 GeV	−1/3	1/2
electron(e), muon(μ), tau(τ)	0.511 MeV, 105.7 MeV, 1.777 GeV	−1	1/2
neutrinos: ν_e, ν_μ, ν_τ	< 2.2 eV, < 0.17 MeV, < 15.5 MeV	0	1/2

Table 2.1: Fundamental particles with half-integer spin. A corresponding antiparticle is also expected. Ordinary matter is constructed of electrons, u and d quarks. The nucleons, proton (p) and neutron (n), consist of {u,u,d} and {d,d,u} quarks respectively.

2.2 Magnetic interactions

The discussion so far concerned the emergence of a local magnetic moment at an independent atom, and the ways in which it can be adapted by the presence of an existing crystal field or an external magnetic field. However, the appearance of spontaneous magnetization in magnetic materials requires neighbouring moments to interact and self-organize in long-range order.

From a classical point of view, magnetic moments can interact by magnetic dipole-dipole interactions. The dipolar effect depends on the magnitude, the relative direction and the distance between the dipoles, and can be described as:

$$H_{D-D} = \sum_{i \neq j} \left[\frac{\boldsymbol{\mu}_i \cdot \boldsymbol{\mu}_j}{r_{ij}^3} - 3 \frac{(\boldsymbol{\mu}_i \cdot \mathbf{r}_{ij})(\boldsymbol{\mu}_j \cdot \mathbf{r}_{ij})}{r_{ij}^5} \right] \tag{2.7}$$

Dipolar interactions may play an important role at low temperatures and in specific magnetic systems; however, they are too weak to create magnetic ordering at high temperatures. Alternatively, the *Heisenberg* model [28, 29] is based on *Coulomb* interaction and utilizes an effective spin-Hamiltonian term to describe the interaction between strong local magnetic moments:

$$H_{ex} = -\sum_{i \neq j} J_{ij} (\mathbf{S}_i \cdot \mathbf{S}_j) \tag{2.8}$$

, where J_{ij} is the exchange coupling integral of the i^{th} and j^{th} electron spin, and $\mathbf{S_i}$ is the quantum mechanical spin operator. The exchange coupling can be determined from first-principles calculations or obtained experimentally. For nearest neighbour spins the interaction is known as direct exchange and J_{ij} can be treated as a constant J, while it decreases rapidly with distance [Fig. 2.2(a)]. A positive $J > 0$ value favors parallel spin alignment, as observed in ferromagnetic (FM) order. For negative $J < 0$ values, an antiparallel alignment is predicted, characteristic of an antiferromagnetic (AFM) order [Fig. 2.2(c)].

Direct exchange interactions require the overlap of electronic orbitals between magnetic atoms, and are therefore short ranged. Alternative exchange mechanisms exist, in which the coupling is achieved indirectly, through non-magnetic atoms or itinerant electrons [Fig. 2.2(a)]. In transition metal complexes, examples of which are the systems studied in Papers I,II,V, a non-magnetic ion is found in between two magnetic ions. Hybridization between the transition metal and non-magnetic atom orbitals leads to a superexchange interaction via a virtual hopping of electrons [Fig. 2.2(b)]. The interaction can result in either an FM or AFM alignment, which is predicted by a set of empirical rules by *Goodenough*, *Kanamori* and *Anderson* (GKA) [30, 31]. Besides superexchange, also double exchange interaction appears between magnetic ions in different oxidation states. A real hopping of electrons occurs between orbitals only if the spin direction is preserved, therefore double exchange favors FM ordering. Delocalized electrons in metallic materials can also be associated with magnetic moments and result in a paramagnetic response or spontaneous magnetization through spin-split bands. Furthermore, a localized magnetic moment can produce an oscillating magnetization in space, which spin-polarizes the itinerant electrons (Paper IV). Depending on the distance, the polarization reaching another localized magnetic moment can result in either FM or AFM coupling, which is known as the RKKY interaction after *Ruderman*, *Kittel*, *Kasuya* and *Yosida* [26, 32].

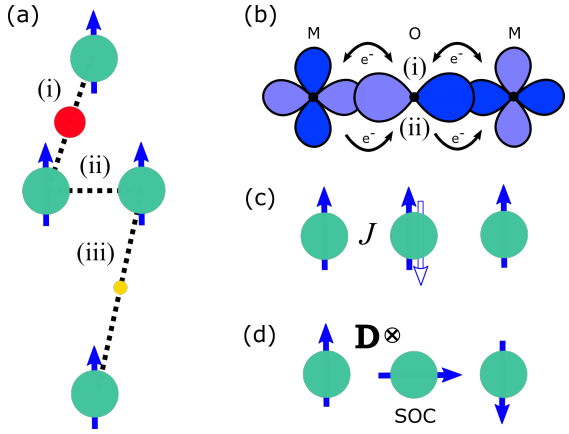

Figure 2.2: (a): Exchange interactions can be direct (ii) in neighbouring atoms with overlapping orbitals, or indirect (i),(iii) through non-magnetic atoms or itinerant electrons. **(b):** Superexchange (i) and double exchange (ii) interactions are prevailing in ionic solids, where electrons of metal ions (M) can hop through overlapping orbitals with an intermediate non-magnetic atom (e.g O). **(c):** The symmetric exchange interaction in the Heisenberg model determines a ferro- or antiferromagnetic coupling of magnetic moments depending on J. **(d):** The antisymmetric DM interaction, which arises due to SOC, promotes a chiral configuration of moments. That is, the magnetization rotates around an axis defined by $\mathbf{D}$.

In the most general case the *Heisenberg* model is symmetric and isotropic. The spins are represented as three-dimensional vectors arranged in a three-dimensional space. If anisotropy is introduced, the model is transformed to describe the reduced dimensionality of the spins or the lattice, and the coupling constants (J_x, J_y, J_z) are varied depending on the interaction at each direction. An anisotropic Heisenberg spin model along the z-direction can have the form:

$$H_{an} = -\sum_{i \neq j} (\zeta S_i^z S_j^z + J \mathbf{S}_i \cdot \mathbf{S}_j) - \sum_i A_i (S_i^z)^2 \tag{2.9}$$

, where ζ, A and J represent the anisotropic and isotropic exchange couplings. This hamiltonian encodes the magnetocrystalline anisotropy towards an easy direction of magnetization, which is an intrinsic property of a crystal. Its source is found in SOC dependence on the crystal lattice structure, which breaks the rotational symmetry of exchange. Many anisotropic and antisymmetric exchange terms have been developed to describe the various anisotropies that may exist in real 3D and 2D magnetic systems [33]. The *Dzyaloshinskii-Moriya* (DM) interaction [34, 35] forms such an antisymmetric anisotropic exchange term:

$$H_{DM} = \sum_{i \neq j} \mathbf{D}_{ij} \cdot (\mathbf{S}_i \times \mathbf{S}_j) \tag{2.10}$$

promoting the perpendicular arrangement of neighbouring spins [Fig. 2.2(d)]. The coupling vector $\mathbf{D_{ij}}$ appears when the inversion symmetry of the system is broken, and determines the orientation of the spin-spin configuration. The DM interaction can take place either in bulk systems, where the inversion symmetry breaks due to the crystalline structure, or in multilayered systems, where the symmetry usually breaks by the change of

atoms at the interfaces. The combination of symmetric and antisymmetric exchange can give rise to chiral magnetic structures, such as magnetic skyrmions (Paper IV). From this short description of exchange interactions it is evident that the configuration of intrinsic magnetic moments depends strongly on the electronic structure of the magnetic ions, the crystal lattice geometry and the dimensionality of the system. Therefore, depending on the chemical composition and intrinsic or extrinsic anisotropies, a system can naturally select a magnetization direction although the hamiltonian does not. This spontaneous symmetry breaking reflects a transition to a magnetically ordered phase.

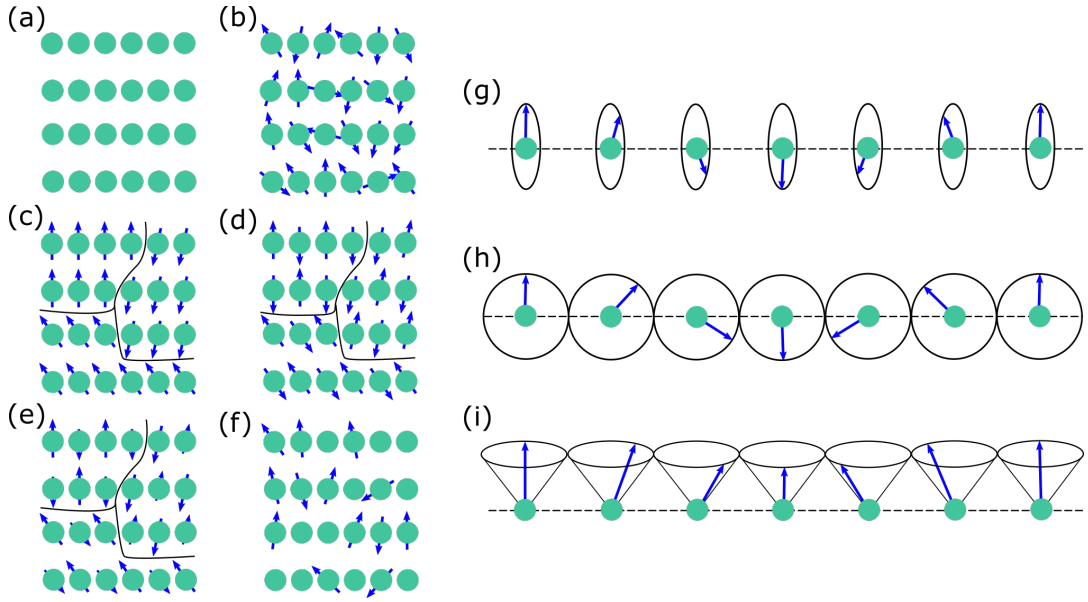

Figure 2.3: The sum of active interactions between magnetic moments can lead to a variety of ordered phases. In zero magnetic field a material can be **(a)** diamagnetic, **(b)** paramagnetic, **(c)** ferromagnetic, **(d)** antiferromagnetic, **(e)** ferrimagnetic, **(f)** spin glass. **(g)** helical, **(h)** cyclical, **(i)** conical spiral. Their combination can create periodic modulations such as spin density waves (SDWs) and skyrmion quasiparticles. The illustrations were inspired from [36].

2.3 Magnetic materials

The collective interactions between magnetic moments and the effect of their environment can lead to different types of magnetic ground states, resulting in materials with characteristic physical properties. Diamagnetic materials resist magnetization. Paramagnets can be magnetized by an external field, however they do not retain their magnetization when the field is removed. Ferromagnetic and ferrimagnetic materials have a spontaneous net magnetization while antiferromagnetic materials, although ordered, present no net magnetization. Spin glasses comprise random but frozen arrangements of mangetic moments. Cyclical or helical spin arrangements can create periodic modulations such as spin density waves (SDWs) or skyrmion quasiparticles [Fig. 2.3].

A straightforward and insightful method to investigate the type of magnetic order in a material is to measure the magnetization or magnetic susceptibility as a function of

temperature or applied magnetic field. When this material is placed in a magnetic field $\mathbf{H}$, it will interact with a given energy $U = -\mu\mathbf{H}$, and become magnetized $\mathbf{M} = \frac{d\mu}{dV}$. The net magnetization is given by $\mathbf{M} = \chi\mathbf{H}$, where χ is the magnetic susceptibility of the material. For $\chi < 0$ the material resists magnetization, while for $\chi > 0$ it embraces magnetization. The magnetization and magnetic susceptibility can be determined by a variety of theoretical models depending on the closest approximation to the studied system [26]. Therefore, the experimental results can be directly correlated with the underlying microscopic mechanisms of magnetism. However, magnetism involves processes in different time and space scales, ranging between $10^{-15} - 10^{9}$ s and $10^{-10} - 1$ m. The use of experimental techniques with various probes and resolutions allows us to create a clearer picture of the magnetic phases and their evolution [37].

Cooling the material leads to a decrease of thermal fluctuations, typically enabling the system to reach a magnetically ordered state. However, there exist additional important parameters, which can determine a phase transition. By modifying the externally applied magnetic field, applying pressure, altering the chemical composition or altering the sample geometry, we can induce anisotropies and alter the magnetic interactions in the system. The emergence of magnetic states can be deduced thermodynamically from the free energy F of the partition function $Z = \exp(-F/k_B T)$. At a phase transition, various physical quantities undergo substantial changes, which lead to dramatic shifts of the free energy. In the critical region, the behavior of the system is described by a set of critical exponents. The order parameter is a statistical function that changes values at each phase. In magnetism the representative order parameter is the magnetization density:

$$m(T) = \frac{1}{V}\lim_{H\to 0} M(H,T) \propto \begin{cases} 0 & , T > T_C \\ H^{\frac{1}{\delta}} & , T = T_C \\ |t|^{\beta} & , T < T_C \end{cases} \tag{2.11}$$

, where $t = (T - T_C)/T_C$ is the reduced temperature. The singular behavior of the order parameter along the coexistence line and the critical isotherm is characterized by the critical exponents β and δ respectively. To explain the magnetization phenomena we have to reconsider the dipole-dipole interactions [38], which were deemed too weak to explain the interactions among nearest neighbors in comparison to exchange interactions. In a material that consists of an enormous number of spins though, the long ranged dipolar interactions rearrange the spin ordering into magnetic domains. The spin magnetic moments will be coupled to the electronic charge density through SOC, therefore their orientation with respect to the crystal lattice will affect their energy. This is where magneto-crystalline anisotropy comes into play, defining the energy required to align the magnetic moments into different directions. Depending on the shape of material grains, surfaces, dimensionality or applied stresses, more anisotropies arise, which create, alter or thermodynamically shift magnetic phases.

Chapter 3

The muon perspective

In this chapter, we introduce the muon particle and identify the properties which favor the use of muons in material studies. Our primary focus is on the principal experimental method, namely positive muon spin rotation, relaxation or resonance (μSR). The main steps of the experimental procedure are presented, covering the production of a spin-polarized muon beam and the interaction of muons with a sample under various experimental modules. The spin of muons implanted in a sample interacts with the magnetic field distribution of its local environment. These interactions yield information about the static and dynamic magnetic environment in our samples. In the following section we focus on the interpretation of the exported data, lay out the basic fitting functions employed in the experimental data analysis, and discuss their physical meaning.

3.1 What is a muon?

The muon is an elementary particle classified within the lepton family of the Standard Model [39]. It carries a negative charge identical to that of an electron but possesses a mass two hundred times greater. A crucial feature of the muon is its spin of 1/2, resulting in a magnetic moment which allows it to magnetically interact with its environment and sense magnetic fields down to the mT scale. This interaction is partly encoded in the gyromagnetic ratio (γ_μ), an important constant that describes how fast the magnetic moment will preccess at a particular magnetic field. Like all particles, the muon has an antiparticle, here denoted as positive muon (μ^+). The main properties of μ^+ are presented in Table 3.1, since it is the key element of the μ^+SR experimental technique discussed in the greatest part of this chapter. Furthermore, the muon is a radioactive particle. The brief lifetime of μ^+ ends by a decay via the weak force into a positron and two neutrinos following specific conservation laws, which allows us to monitor the muon's magnetic interactions with matter.

charge	spin	magn. moment	$\gamma/2\pi$	lifetime	mass
$+e$	1/2	$3.18\mu_p$ $4.836 \times 10^{-3}\mu_B$	135.53 MHzT^{-1}	2.197 μs	$206.768m_e$ $0.1124m_p$ 105.7 MeV

Table 3.1: Positive muon properties.

3.2 The life of a muon

At the time of its discovery in cosmic rays and in the decade that followed, the muon was regarded as an extraterrestial stranger and a misfit in any established scheme for the fundamental constituents of matter and force. However, within the evolving paradigm of modern particle physics, the muon eventually found its place among a long list of recently discovered particles. The advancement of particle accelerators has elevated the muon to a prominent status, serving as a valuable probe in both atomic and sub-atomic physics, with a potential to fundamentally reshape our comprehension of nature in the future.

3.2.1 In the wild

The study of cosmic radiation has a long history dating back to 1785 when *Charles Augustin de Coulomb* observed spontaneous discharges in electrometers within the atmosphere. This phenomenon was later attributed to ionizing species carried by a penetrating radiation from space. *Victor Hess*, in his pivotal experiments between 1911-12, conclusively identified cosmic radiation [40].

(a) (b)

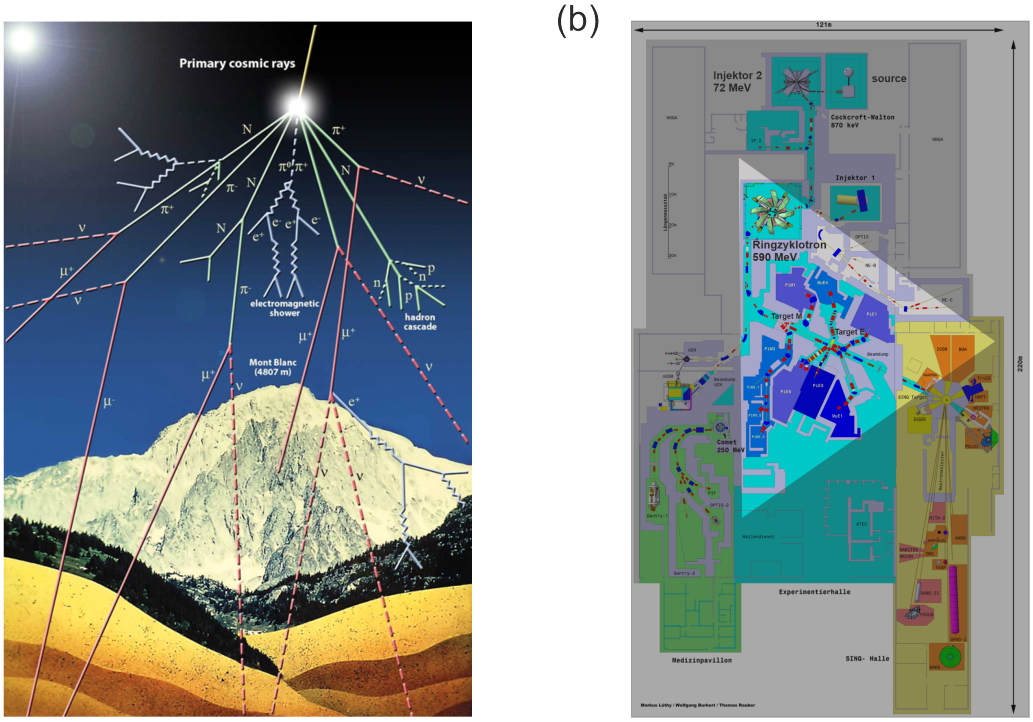

Figure 3.1: **(a)**: Cosmic rays reach and interact with the Earth's upper atmosphere producing a shower of secondary particles. The pion decay produces a muon that will reach the Earth's surface if its energy is sufficient. Adapted from [41]. **(b)**: In the high intensity proton accelerator complex at SμS, PSI, protons are produced from a source and accelerated at two cyclotrons (Injektor 2, Ringzyklotron). The proton channel is then directed towards the pion production targets (M, E). The decaying pions produce muons with the desired characteristics, which are then focused and guided with magnets towards the experimental stations. Adapted from [42].

The current knowledge is that cosmic rays comprise mostly protons and heavier stripped nuclei originating from sources such as stars and supernovae within our own and distant galaxies [43]. The primary radiation reaching Earth falls within the GeV-TeV energy range [44, 45]. In comparison, the binding energies of protons and neutrons in nuclei are on the order of 10 MeV.

These primary particles collide with nuclei of air molecules, giving rise to secondary particles including pions, electrons and photons. Through a series of collisions and decays, a cascade of particles is produced, with the most energetic ones potentially reaching the Earth's surface [Fig. 3.1(a)]. One of the dominating constituents of this particle shower is the muon, discovered by *Carl Anderson* and *Seth Neddermeyer* in 1937 [46]. Muons originate from the decay of charged pions and over their lifespan they travel a relatively long distance, while interacting with matter though weak and electromagnetic forces before undergoing radioactive decay.

The development of charged particle detectors has allowed the use of cosmic muons in various applications through muon flux and momentum measurements. Muons have been employed in a demonstration of the time dilation effect of special relativity, the detection of cavities underground or in massive objects like the pyramids, assessing the structure and density variations in volcanoes for eruption predictions, and mineral exploration [47, 48]. The list of applications extends across numerous research disciplines, as discussed in the subsequent sections.

3.2.2 In captivity

In parallel with cosmic muon studies, the development of particle accelerators gave us the opportunity to experiment with tailor-made particles in an controlled environment. Muons have since been extensively investigated and used as a probe in both particle and material physics. The famous muon g-2 experiment studies alterations in the gyromagnetic ratio of the muon, a fact that could lead to yet undiscovered particles or forces beyond the Standard Model [49, 50]. Ongoing discourse revolves around the potential utilization of muon-antimuon colliders, capitalizing on the low charge-to-mass ratio and fundamental nature of the muon [51]. The proposed experiments require energies of several TeV's. However, at much lower energies the muon proves to also be a unique probe in material research. Studies on the muon magnetic properties and decay characteristics [52–54] have laid the foundation for the development of the μSR technique.

Muons naturally reach the Earth's surface with an average flux of 1 muon$\cdot$m$^{-1} \cdot$ cm^{-2} and possess high energies of an average 4 GeV. These values are unsuitable for experimental purposes in material physics. To employ muons as a probe, higher fluxes in the range of $10^3 - 10^7$ muon $\cdot$ s$^{-1} \cdot$ cm^{-2} and lower energies between 1 keV-200 MeV are necessary [55]. Intense muon beams meeting these criteria can be generated in hadron particle accelerator facilities, serving as the power sources for a μSR experiment.

3.2.2.1 Muon creation

A typical procedure for the production of positive muons mimics the same physical process observed in cosmic rays. Protons are produced from a hydrogen source [Fig. 3.1(b)]. The protons are then fed into a cyclotron accelerator (alternatively a synchrotron or a linear accelerator) to gain the momentum required to produce positive pions. The protons are then guided in vacuum towards a graphite production target. The collision of the energetic proton with a proton of the target nuclei results in a proton, a neutron and a positive,

spinless pion (π^+):

$$p + p \rightarrow p + n + \pi^+ \tag{3.1}$$

with a lifetime of 26.033 ns and mass of 139.570 MeV/c^2. The pion eventually undergoes a two-body decay caused by the weak interaction:

$$\pi^+ \rightarrow \mu^+ + \nu_\mu \tag{3.2}$$

Let us analyse the decay within the reference frame where the pion is at rest. Conservation of the total linear momentum and charge dictates that a positive muon is produced together with a muon neutrino [Table 2.1], and the linear momenta of μ^+ and ν_μ are equal and antiparallel. A crucial factor is that parity violation in weak interactions results in neutrinos having a predominantly negative helicity (-1) from the spin aligned opposite to their linear momentum [54]. Conservation of angular momentum requires the spin of μ^+ to be antiparallel to the ν_μ spin. The μ^+ is therefore 100% spin polarized antiparallel to its linear momentum [Fig. 3.2]. In practice muons are emitted in a range of angles θ. Therefore, the spin polarization with respect to the beam direction depends on the accepted angular range, but still remains higher than 95%.

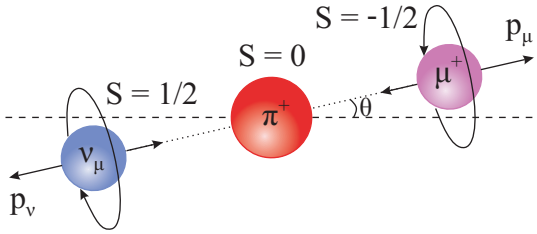

Figure 3.2: The π^+ decay in the rest frame of the pion. Conservation of momenta and the negative helicity of the neutrino determine the spins of ν_μ and μ^+ to be antiparallel to their linear momenta. Inspired from [56].

The mechanism described above takes place at a particular type of muon beamline where μ^+ are produced from π^+ decaying at rest, close to the target surface. This type is therefore called surface beamline and the muons produced, surface muons. From the conservation of energy and momentum in the two-body decay of a π^+ at rest we can calculate the kinetic energy of the created muon:

$$E_{k,\mu} = \frac{(m_\pi - m_\mu)^2 c^2}{2m_\pi} \tag{3.3}$$

depending only on the pion and muon mass. The kinetic energy and momentum of the muon are therefore determined to be 4.12 MeV and 29.79 MeV/c respectively. Depending on the production mechanism and the configuration of the beamline transporting the muons to the experimental chamber the muon beam can be customized in terms of momentum, spin polarization, muon charge, beam structure, beam-spot size etc. Examples of these variations will be presented in a subsequent section of this chapter.

3.2.2.2 Muon decay

The produced μ^+ beam is consequently focused and steered towards the experimental chamber, and targeted on the sample. As the spin-polarized muon travels through the sample, initially it ionizes or excites the electrons in proximity until its kinetic energy drops below these thresholds [57]. During this process the muon may capture and lose an electron but the Coulomb interaction does not depolarize the muon spin. There is a possibility that the positive muon captures and holds an electron, forming an electrically neutral bound state called muonium. This formation is most likely to appear in non-metallic materials, below a limit of free-electron density [58]. The path length of muons depends on their kinetic energy and the material density. The variations of path lengths drop down to a few percent for kinetic energies in the MeV range. In most cases the muon eventually thermalizes in a location with high electron density, well away from vacancies that may have been created in its path. There, it interacts magnetically with its local environment until it decays:

$$\mu^+ \rightarrow e^+ + \nu_e + \bar{\nu}_\mu \tag{3.4}$$

The muon decay is also a result of the weak interaction and produces a positron (e^+), an electron neutrino and a muon antineutrino. Considering the conservation laws and parity violation for a three-body decay in the rest frame of the muon, results in an anisotropic positron emission. The emission angle and energy of the positron form a distribution [59], where the most energetic positrons have a higher probability to be emitted in the direction of the muon spin at the moment of decay. In this we find the working principle of μSR. By detecting the direction of the emitted positron we are able to determine the direction of the muon spin at the moment of its decay, after it interacted with the magnetic fields present at the particular interatomic region in the sample material. The probability of positron emission at an angle θ to the muon spin direction just before decay is given by

$$d\Gamma(x,\theta) = E(x)[1 + \alpha(x)cos\theta]dxd(cos\theta) \tag{3.5}$$

, where $x = E/E_{max}$ a parameter of positron energy with a maximum value of $E_{max} =$ 52.83 Mev from the conservation of energy and momentum in the muon decay. The parameterized energy spectrum has the form:

$$E(x) = 2x^2(3 - 2x) \tag{3.6}$$

and the term

$$\alpha(x) = \frac{2x - 1}{3 - 2x} \tag{3.7}$$

is an asymmetry factor which describes the asymmetric positron emission as a consequence of the weak interaction. The angular distribution of emitted positrons for different normalized positron energies is presented in Figure 3.3(a). We notice that the asymmetry is highest for the most energetic positrons, the distribution becomes more isotropic as the energy drops, and at low energies the asymmetry becomes negative. The average asymmetry is given by

$$\langle\alpha\rangle = \int_0^1 \alpha(x)E(x)dx = \frac{1}{3} \tag{3.8}$$

and is represented in Figure 3.3(a) by the green curve. In practice the maximum observed asymmetry is in the range of 24-30% [56], due to the angular arrangement of the detectors around the sample, exclusion of low energy positron signals and signal corrections with respect to intermediate positron interactions.

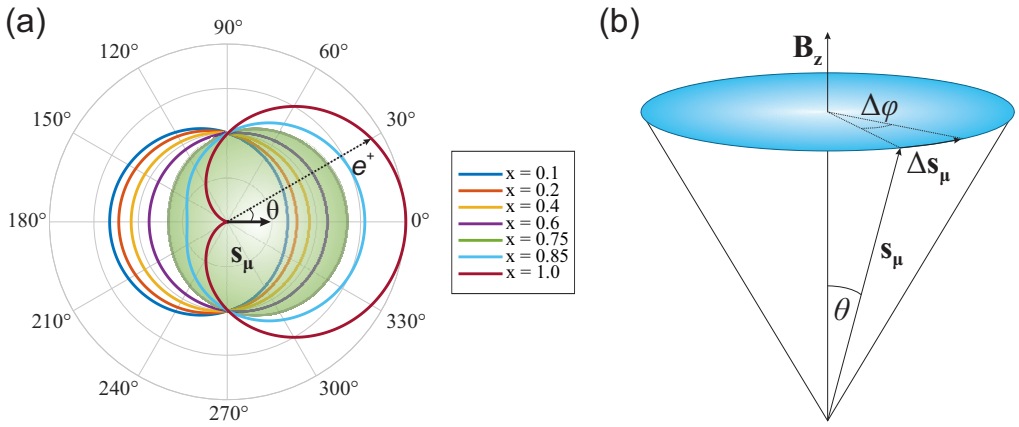

Figure 3.3: **(a)**: The angular distribution of emitted positrons with respect to the muon spin direction $\mathbf{S}_\mu$, for various normalized energy values. The dotted arrow length reflects the probability of the particular positron emission. **(b)**: An illustration for the Larmor precession of the muon spin around a local magnetic field $\mathbf{B_z}$.

3.3 The muon as a magnetic probe

Following a spin-polarized μ^+ penetration and eventual thermalization into a sample, its spin will depolarize through the interaction with a local magnetic field. The asymmetric emission of a positron allows us to determine the direction of the muon spin at the moment of decay. The lifetime of each muon will vary from the average lifetime (τ_μ) according to the radioactive decay law

$$n(t) = n(0)e^{-t/\tau_\mu} \tag{3.9}$$

, therefore each decay positron contributes to a snapshot of the muon spin at a particular decay time. From an ensemble of millions of muon decays, the paths of the captured positrons create a histogram of the average muon spin polarization as a function of time. The analysis of such histograms provides information regarding the magnetic environment in the studied material.

3.3.1 Larmor precession

As discussed previously, the interaction of a polarized muon spin with a local magnetic field leads to depolarization. This interaction is ideally treated within the quantum-mechanical framework, considering the purely quantum nature of spin. However, for the purposes of this chapter, we adopt the illustrative and effectively correct classical approach.

The magnetic moment of the muon can be described as

$$\boldsymbol{\mu} = \gamma \mathbf{S} \tag{3.10}$$

, where $\gamma = gq/2m$ the gyromagnetic ratio of the muon given its charge (q), mass (m) and g-factor ($g \simeq 2$. The spin is therefore seen as an intrinsic angular momentum. A local magnetic field creates a torque on the muon's magnetic moment

$$\boldsymbol{\tau} = \frac{d\mathbf{S}}{dt} = \boldsymbol{\mu} \times \mathbf{B} = \gamma \mathbf{S} \times \mathbf{B} \tag{3.11}$$

, meaning that the rate of change of the spin angular momentum is perpendicular to the spin and the magnetic field. This causes a precessing movement called *Larmor* precession, with angular velocity $\omega = \gamma B$ [Fig. 3.3(b)]. For a finite angle $\Delta\phi$ the torque can be given by

$$\tau = \frac{S sin\theta \Delta\phi}{\Delta t} = \gamma S B sin\theta \tag{3.12}$$

If we assume a magnetic field along the z direction, then the spin angular momentum in three dimensions is given by

$$\mathbf{S}(t) = |\mathbf{S}| \begin{pmatrix} sin\theta\, cos\omega\, t \\ -sin\theta\, sin\omega\, t \\ cos\theta \end{pmatrix} \tag{3.13}$$

We observe that only the components perpendicular to the magnetic moment oscillate in time, while the parallel component remains constant. Since an ensemble of millions of muons is studied, we can define the muon spin polarization as

$$\mathbf{P}(t) = \frac{\langle \mathbf{S}(t) \rangle}{|\mathbf{S}(0)|} \tag{3.14}$$

, with respect to the average spin polarization over all the initial muon spin vectors. In the next section we describe how the time evolution of this muon spin polarization occurs from the detection of asymmetrically emitted positrons.

3.3.2 The μ^+SR experiment

This section focuses on the basics of a μ^+SR experiment and the treatment of primary data. The main instrument at the experimental station of a μ^+SR beamline is a spectrometer. The sample is placed at its center, surrounded by positron detectors which cover the angular distribution of the emitted positrons. Additionally, the sample is surrounded by an arrangement of magnets. The experiment is typically carried out in true zero field (ZF), with a longitudinal field (LF) applied parallel to the initial spin polarization, or with a transverse field (TF) applied perpendicular to the initial spin polarization. We follow the convention were the z-axis is always parallel to the applied magnetic field. In the TF geometry, the initial muon spin is parallel to the x-axis. A simplified representation of the experimental chamber is shown in Figure 3.4. This schematic in particular represents a time differential measurement in a continuous source of surface muons. Alternative experimental setups will be described in the following chapter.

Here the muon comes with a spin antiparallel to its momentum. Therefore, when it stops in the material, if it decays right away (at t=0), or precesses around a field and

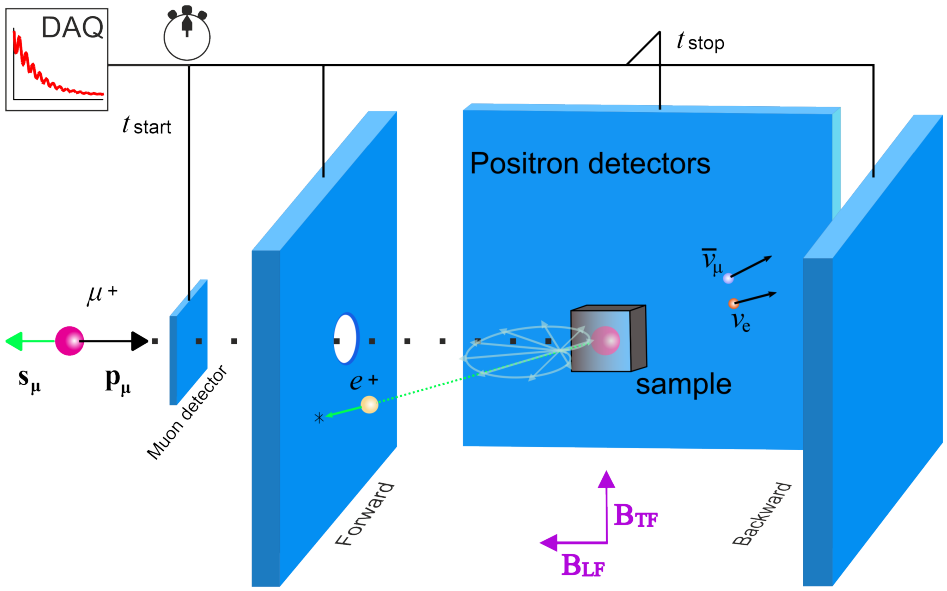

Figure 3.4: Representation of a time differential μ^+SR measurement. An incoming, spin polarized muon is first counted by a muon detector which sets the starting time of a measurement. The muon then flies through the windows of the positron detectors and the cryostat, and is implanted into the sample. When it thermalizes at its stopping site, the muon spin will interact with the surrounding magnetic fields. These fields may be intrinsic, applied perpendicular ($\mathbf{B}_{TF}$) or parallel ($\mathbf{B}_{LF}$) to the muon spin. The muon eventually decays to a positron, an electron neutrino and a muon antineutrino. The direction of the positron emission is most probable to be parallel to the muon spin at the moment of decay. One of the positron detectors will collect the emitted positron and set the stopping time of this count. A successive count follows in this manner. This schematic was inspired from [18].

decays when its spin is in the same direction, then the decay positron will most probably be collected by the Forward detector. If the spin precesses with an applied and/or intrinsic field, then it may decay with a spin towards the opposite direction, where the Backward detector counts. The number of positron events at a particular detector corresponds to the spin polarization direction of decaying muons at times t. Starting from Eqs. 3.5,3.9 and considering a positron detector covering a finite solid angle, the number of positrons counted by the Forward and Backward detector is given by:

$$N_{F|B}(t) = B + N^0_{F|B} e^{-t/\tau_\mu} \left[1 \pm A_0 \mathbf{P}(t) \cdot \hat{\mathbf{n}}\right] \tag{3.15}$$

in the direction of each positron detector. Here, B accounts for the time independent background events. The $N^0_{F|B}$ are scaling parameters for the count rates in the active solid angle. A_0 is the initial experimental asymmetry, which is lower than the average asymmetry [Eq. 3.8] due to the finite solid angle and the efficiency of the detector in counting high energy positrons. In Eq. 3.15 the polarization function is superimposed on the exponential describing the decay of muons. In order to extract the polarization function, we calculate the asymmetry of the opposite detector counts:

$$A(t) = A_0 P(t) = \frac{N_F(t) - \alpha N_B(t)}{N_F(t) + \alpha N_B(t)} \tag{3.16}$$

, where $\alpha = N_F^0/N_B^0$ is a correcting factor that accounts for any inequivalence in geometry and efficiencies between the two detectors. At the beginning of an experiment the values α, A_0 are determined as part of the calibration process. The initial asymmetry is determined by measuring a metallic reference sample (typically an Ag plate) in TF. Then α is determined in TF on our sample, above any magnetic ordering temperature. It is selected so that the observed oscillations are symmetric about the time axis. The time dependent muon polarization function $P(t)$ contains the information about the magnetic environment interacting with the muon spin. An example of the detector signals and exported polarization function is presented in Figure 3.5.

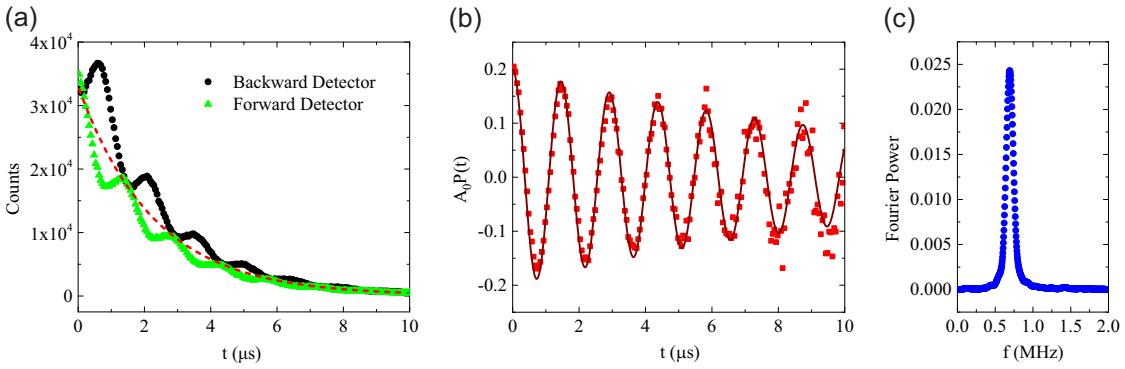

Figure 3.5: Example of experimental results in a system where muons interact with a field perperndicular to the initial muon spin direction. **(a)**: Positron counts versus time for the forward and backward detector. The dotted line shows the average signal representing the exponential decay of muons. **(b)**: The extracted asymmetry or depolarization function. **(c)**: A Fourier transformation of the μSR signal into the frequency domain shows the distribution of frequencies in which the muons *Larmor* precess.

3.4 Depolarization functions

The objective of the μSR data analysis is to determine a suitable and physically meaningful depolarization function that describes the signal. In this section, the muon spin polarization will be treated classically, within the framework of Refs. [18, 56]. Starting from the highest-order scenario, we will introduce a series of depolarization functions formulated to describe systems featuring static, homogeneous, inhomogeneous and dynamic magnetic fields.

3.4.1 Homogeneous static fields

We start by considering an ideal scenario, in which polarized muons within a single crystal interact with a static, homogeneous magnetic field $\mathbf{B_{loc}}$ directed at an angle θ from $\mathbf{S}_\mu$, The polarization is calculated from the projection of the *Larmor* equation [Eq.3.13] along the direction of observation κ, and has the form:

$$P_\kappa(t) = \cos^2\theta + \sin^2\theta\cos(\omega_\mu t) \tag{3.17}$$

, where ω_μ the muon's *Larmor* angular velocity. This function consists of a static term and an oscillatory term, which describes the precession in the field. By rotating the sample with respect to the muon beam we can determine the direction of the magnetic field from the change in amplitude of the oscillation observed in the spectrum. For $\theta = 90°$ and $\theta = 0$ the depolarization function becomes $P_\kappa(t) = \cos(\omega_\mu t)$ and $P_\kappa(t) = 1$ respectively when the field is transverse or parallel to the direction of the muon spin. Now let us consider a polycrystalline sample in a ZF meaurement. If the sample's internal field, $\mathbf{B_{loc}}$, is the same at all muon sites in the randomly aligned crystallites, then an isotropic field distribution appears. In this case the depolarization function is spherically averaged and takes the form

$$P_z(t) = \frac{1}{3} + \frac{2}{3}\cos(\omega_\mu t) \tag{3.18}$$

Here P_z is considered in the z-direction, which is the direction of interest in the ZF geometry. The constant 1/3 term reflects the fraction of internal fields aligned with the initial muon spin while the 2/3 term represents the perpendicular fields. These terms are also referred to as the parallel and perpendicular component. The first describes the non-oscillatory segment of the spectrum, whereas the second fits the oscillations reflecting the magnetic order. Nevertheless, in the presence of disorder in the magnet, denoting a range of $\mathbf{B_{loc}}$ values, the oscillation will be damped or may even cease entirely. If the spin precession frequency exceeds the frequency window of μ^+SR, then also no oscillations will be detectable. In this case a magnetic phase transition is inferred from the drop in asymmetry to $A_0/3$.

3.4.2 Inhomogeneous static fields

In most cases the muon spin is depolarized from interactions with either a static distribution of local fields or fluctuating fields [60, 61]. These fields have electronic and nuclear origin, dominated by dipolar interactions with the muon magnetic moment, or can simply originate from an externally applied magnetic field. Starting from Eq. 3.17 we can devise depolarization functions that describe complicated environments. Let $D(\mathbf{B_{loc}})$ be a field distribution at the muon site and $\hat{S}^{\hat{\mu}}_\kappa(t, \mathbf{B_{loc}})$ the projection of the muon spin unit vector along a direction κ. The polarization can thus be derived from

$$P_\kappa(t) = \int \hat{S}^{\hat{\mu}}_\kappa(t, \mathbf{B_{loc}}) D(\mathbf{B_{loc}}) d\mathbf{B_{loc}} \tag{3.19}$$

This is a general form that produces the depolarization function in a field distribution that describes our physical system, and in a chosen direction of observation. If a Dirac delta function is selected as $D(\mathbf{B_{loc}})$ then Eq. 3.19 falls back to Eq. 3.17. Alternatively, one can use a Gaussian distribution

$$D(\mathbf{B_{loc}}) = \frac{\gamma_\mu}{\sqrt{2\pi}\Delta} exp\left(-\frac{\gamma_\mu^2 B_{loc}^2}{2\Delta^2}\right) \tag{3.20}$$

or a Lorentzian distribution

$$D(\mathbf{B_{loc}}) = \frac{\gamma_\mu}{\pi} \frac{\Delta}{\Delta^2 + \gamma_\mu^2 B_{loc}^2} \tag{3.21}$$

to calculate the depolarization function from Eq. 3.19. In a single crystal, for a spontaneous field B_0 sufficiently larger than Δ, the depolarization function will have the form

$$P_z(t) = cos(\omega_\mu t)e^{-\frac{\sigma^2\tau^2}{2}} \tag{3.22}$$

, referred to as a Gaussian relaxation function with a depolarization rate $\sigma = \sqrt{\Delta_\mu^2/\gamma_\mu^2}$, and

$$P_z(t) = cos(\omega_\mu t)e^{-\lambda t} \tag{3.23}$$

, the Lorentzian relaxation function with a relaxation rate $\lambda = \gamma_\mu\Delta$. Additionally, Eq. 3.22, 3.23 can also be used for an externally applied field i.e., at a TF measurement on a system with a static field distribution. The form of these depolarization functions is presented in Figure 3.6, in comparison to the archetypical depolarization function (Eq. 3.17). In a TF measurement the applied field dominates the muon precession and a clear oscillating signal is observed. If spontaneous internal fields appear, the competition will dephase the muon spin precession creating a damping in the observed oscillating signal. Therefore, we perform temperature dependent measurements to observe a possible damping of TF oscillations that will indicate inhomogeneities of the local field or a dramatic damping if the system crosses to a magnetically ordered state.

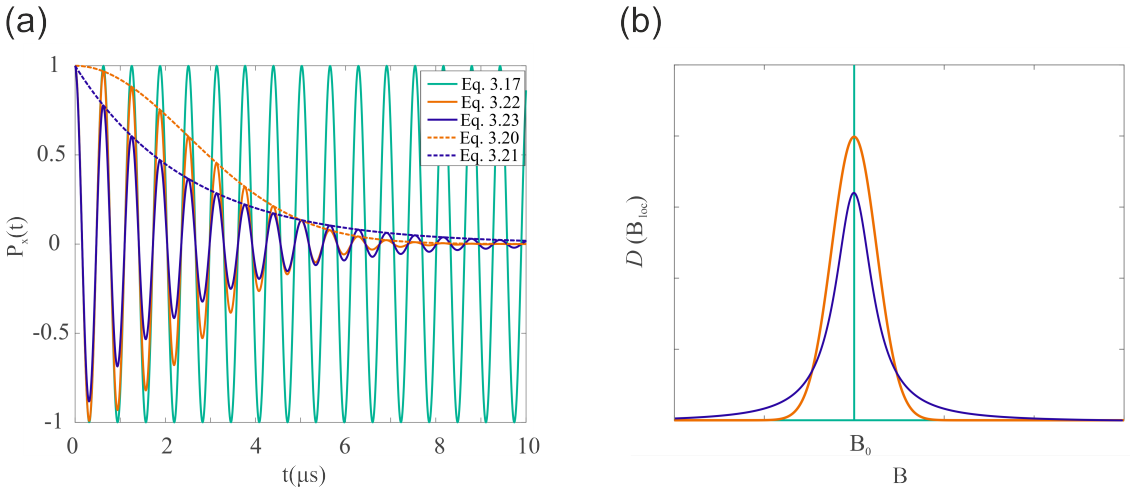

Figure 3.6: **(a)**: Depolarization function in a static homogeneous field B_0 (green), a static Gaussian (orange) and Lorentzian (blue) distribution around B_0. **(b)**: The respective delta function, Gaussian and Lorentzian distribution describing the envelope (dotted lines).

3.4.2.1 Disordered systems

The Gaussian and Lorentzian distributions provide also reasonable models for magnetically disordered materials where no spontaneous field arises. An isotropic Gaussian distribution describes a system of concentrated magnetic moments of similar size, randomly oriented in the lattice [Fig. 3.7(a)]. All implanted muons experience an equivalent magnetic environment, which may originate from electronic or nuclear moments. In this case Eq. 3.19 will give a depolarization function with the form

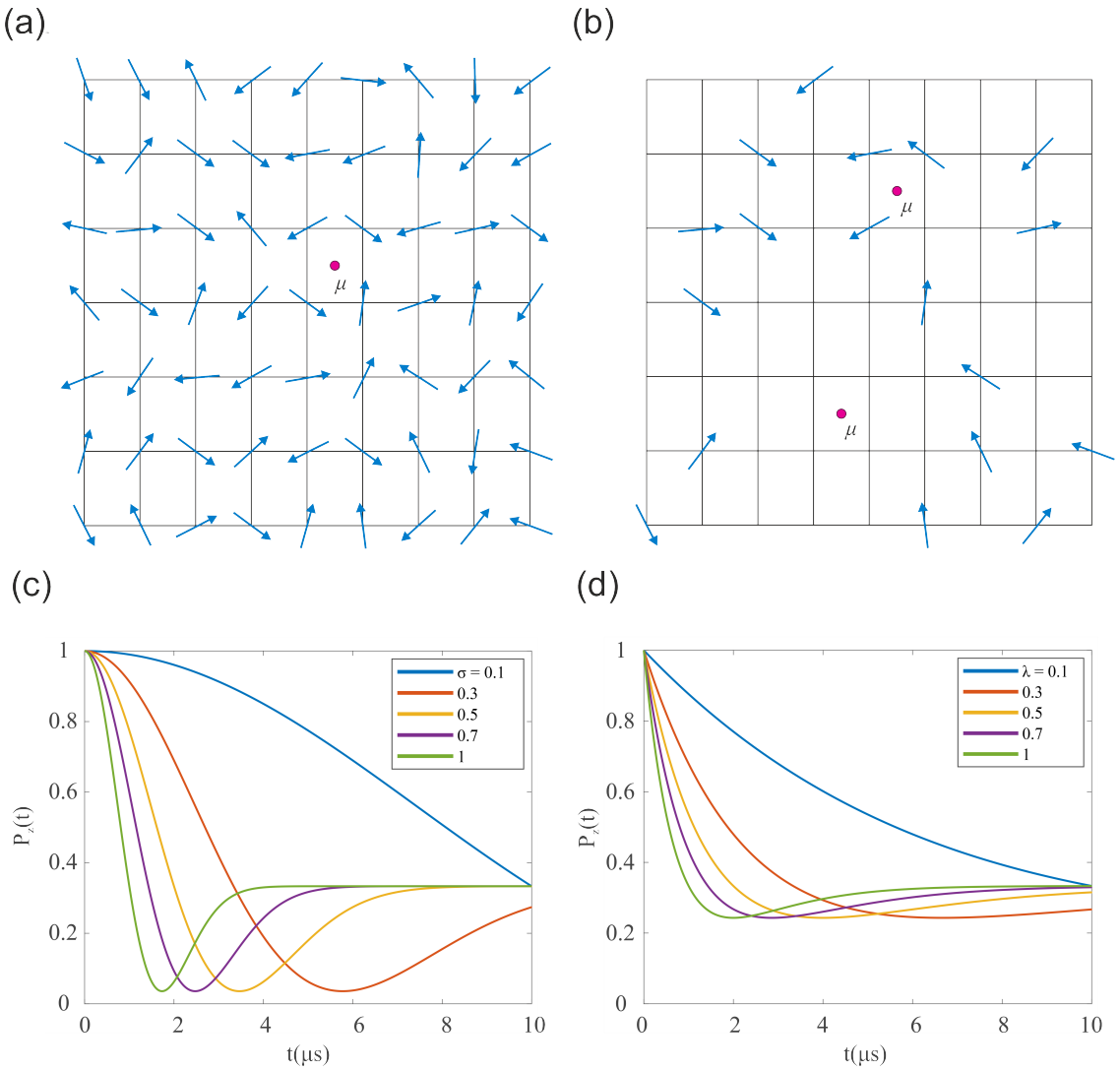

Figure 3.7: Illustrations of muons (magenta spheres) probing disordered systems with a dense **(a)** and a dilute **(b)** arrangement of magnetic moments at the lattice sites. The corresponding depolarization functions Gaussian KT **(c)** and Lorentzian KT **(d)** for various values of σ and λ.

$$P_z(t) = \frac{1}{3} + \frac{2}{3}(1 - \sigma^2 t^2)e^{-\frac{\sigma^2 t^2}{2}} \tag{3.24}$$

, where $\sigma = \sqrt{\Delta_\mu^2/\gamma_\mu^2}$. This is known as the Gaussian *Kubo-Toyabe* (KT) function. The 1/3 and 2/3 terms are attributed to the parallel and perpendicular field components with respect to the muon spin, as in Eq. 3.18. The form of Gaussian KT can be described as a damped oscillation around the asymmetry value 1/3. A fast depolarization, caused by the perpendicular field components, takes place at short times until it reaches a minimum at $t = \sqrt{3}/\gamma_\mu\sigma$. The minimum is the result of the dephasing of oscillations caused by the field distribution [Fig. 3.8]. At longer times a constant 1/3 term is recovered, since the parallel component will not affect the muon spin. The position of the minimum shifts in time depending on σ. For higher/lower σ values the minimum moves to shorter/longer

times, indicating a faster/slower depolarization from larger/smaller moments [Fig. 3.7(c)].

The Lorentzian distribution characterizes a sparse arrangement of magnetic moments in a lattice. In this picture, the muons will sense an environment of lower or higher fields depending on their location in the lattice [Fig. 3.7(b)]. From Eq. 3.19 with a square-Lorentzian distribution [62] we arrive to the Lorentzian KT function

$$P_z(t) = \frac{1}{3} + \frac{2}{3}(1 - \lambda t)e^{-\lambda t} \tag{3.25}$$

, where $\lambda = \gamma_\mu \Delta$. We observe once more the 1/3 an 2/3 terms for the parallel and perpendicular local field components with respect to the initial muon spin, which indicates an isotropically distributed local field. In the short time scale the depolarization follows an exponential decay, reaching a minimum at $t = 2/\lambda$, and eventually recovers the 1/3 value at longer times [Fig. 3.7(d)].

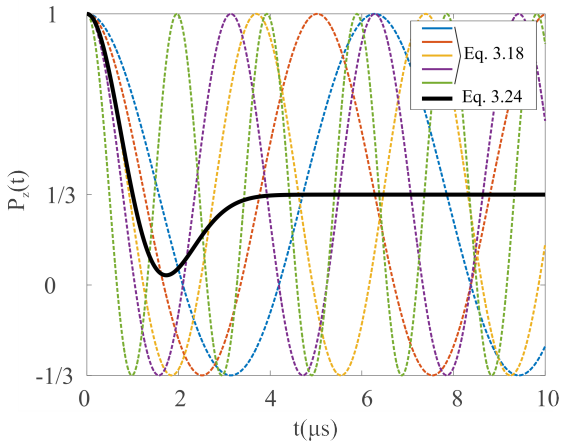

Figure 3.8: Time evolution of the depolarization function Eq. 3.18 with various local fields (colored dotted lines). A Gaussian KT function (black) is the weighted average over these fields.

3.4.3 Dynamic systems

Often, the depolarization function is called to describe local fields that vary with time, within the lifetime of the probing muons. A useful approach on dynamic changes is to consider the evolution of the field as a series of independent and random events following a Gaussian-Markovian process [63]. In effect, the local field abruptly fluctuates at a rate, ν, and changes its value randomly to another, from the available configurations of its constituent moments. The new field at each step follows a Gaussian distribution. This approximation is called **strong-collision model** (SCM). If the fluctuation time, τ, is long compared to the precession time of the muons, the precession will refresh in a new field environment. According to SCM, if the system is in the slow-fluctuation limit ($\gamma B\tau \gg 1$), the muon polarization is not affected by the fluctuations at short times and only the long-time tail relaxes exponentially. In the fast-fluctuation limit ($\gamma B\tau \ll 1$) the polarization relaxes exponentially in the whole time window. A recursive relation of muons experiencing alterations is formed, based on the probability that the field distribution remains constant in a given time. The dynamic depolarization function is calculated in relation to a static depolarization function, given by

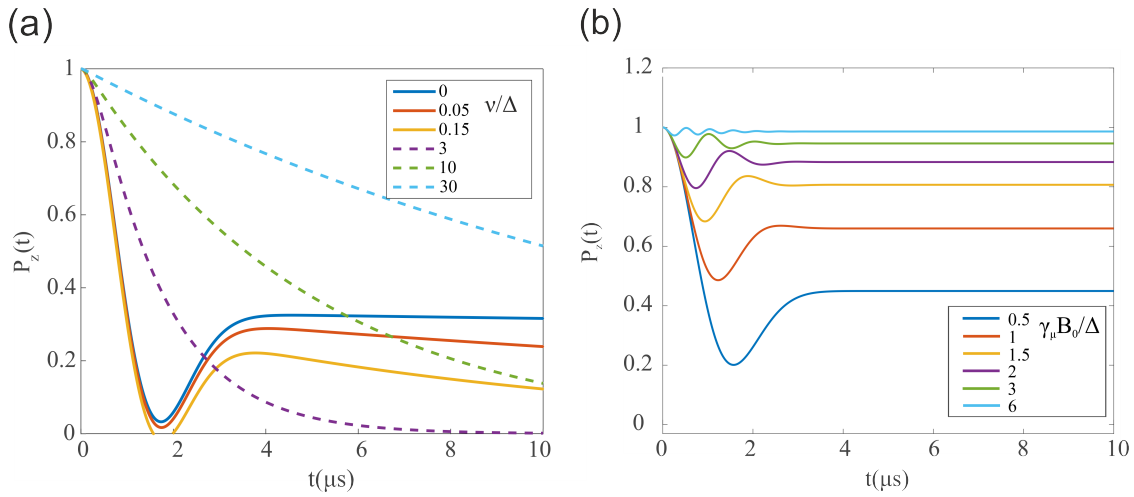

Figure 3.9: **(a):** The dynamical zero/longitudinal depolarization functions from Eq. 3.28, Eq. 3.29 calculated for a Gaussian KT in the strong-collision model are presented for various values of the fluctuation rate ν/Δ. **(b):** The LF Gaussian KT function for various magnetic fields. The coupling of the muon spin and the enhancement of the parallel component is observed with increasing field.

$$P_{z,dyn}(t) = P_{z,stat}(t)e^{-\nu t} + \nu \int_0^t P_{z,dyn}(t-t')P_{z,stat}(t')e^{-\nu t'}dt' \tag{3.26}$$

,where $e^{-\nu t}$ is the probability that the field has remained constant from 0 to t and $P_{z,stat}$ is our choice of an initial static depolarization function. Under a Laplace transform Eq. 3.26 becomes

$$\tilde{P}_{z,dyn}(s) = \frac{\tilde{P}_{z,stat}(s+\nu)}{1-\nu\tilde{P}_{z,stat}(s+\nu)} \tag{3.27}$$

If we consider an isotropic Gaussian distribution for **B**, the corresponding static depolarization function will be a Gaussian KT function (Eq. 3.24). From Eq. 3.27 and the Laplace transform of Eq. 3.24 we obtain

$$P_{z,dyn}(t) \approx \frac{1}{3}exp\left(-\frac{2}{3}\nu t\right) + \frac{2}{3}(1-\Delta^2 t^2)exp\left(-\frac{\Delta^2 t^2}{2}\right) \tag{3.28}$$

, for $\nu/\Delta \ll 1$. This is the quasi-static limit where the 1/3 tail is damped at a rate of $2\nu/3$ due to slow dynamics. This can be understood as a dephasing of muon spin precession from the two (out of three) perpendicular field components. Then in the fast fluctuation limit, $\nu/\Delta \gg 1$, we obtain

$$P_{z,dyn}(t) = exp\left\{-\frac{2\Delta^2}{\nu^2}[exp(-\nu t) - 1 + \nu t]\right\} \tag{3.29}$$

, which is similar to the results obtained from the weak collision model [64, 65] and provides an accurate approximation of P_z for $\nu/\Delta \geq 3$ [Fig. 3.9(a)]. In the fast fluctuation limit, for $\nu t \gg 1$ Eq. 3.29 reduces to an exponential relaxation

$$P_{z,dyn}(t) = e^{-\lambda t} \quad , \quad \lambda = \frac{2\Delta^2}{\nu} \tag{3.30}$$

The dynamic Gaussian KT function is commonly employed to study ion dynamics and appears also in Paper III. When a positive muon arrives at a stopping site inside a material in the paramagnetic state, it will interact with the dipole field distribution from random nuclear moments, a field distribution which can be described by a static Gaussian KT function. However, ion diffusion itself creates problems in the strong-collision model. As a result of diffusing ions or fluctuations in the lattice, the muons themselves can become a dynamic component, and possible changes in their stopping sites may lead to new environments that require new initial static depolarization functions to be described.

While a dynamic depolarization function can be derived from Eq. 3.26, the dynamic depolarization can also be observed from LF measurements. This phenomenon occurs in regions where the fluctuations are within the frequency range of the muon, such as in the slowing down of magnetic fluctuations when approaching a phase transition temperature from above. In this region, an exponential depolarization (Eq. 3.30) is likely to be observed. Additionally, another justification for exponential relaxation is the Lorentzian KT depolarization function (Eq. 3.25). This issue can be effectively addressed within μ^+SR, particularly through LF measurements. When the LF field surpasses the internal fields, more muons will align with the parallel component, resulting in an increase in the tail of the depolarization function and a reduction of depolarization [Fig. 3.9(b)]. The muons will be decoupled from the static internal field, which is now distributed around the external field. With increasing LF fields the muon polarization will eventually become nearly time independent. Conversely, in the presence of large fluctuating internal fields, the applied LF fails to decouple the muon spin, and depolarization is not readily reduced.

Chapter 4

Sources and Instrumentation

The current available μSR instruments exist in facilities around the world: ISIS, based at Rutherford Appleton Laboratory (RAL) in Oxfordshire UK. MLF, based at the Japan Proton Accelerator Research Complex (J-PARC) in Tokai JPN. SμS, based at Paul Scherrer Institute (PSI) in Villigen CH. MuSIC, based at the Research Centre for Nuclear Physics (RCNP) in Osaka JPN. CMMS, based at the TRI University Meson Facility (TRIUMF) in Vancouver CA. These research facilities offer a variety of muon sources and experimental instruments. The experiments presented in Chapter 5 were conducted at ISIS, SμS and CMMS with either surface or low energy positive muons, from a pulsed or continuous source. In the following section we present the basic characteristics of these muon sources, and the typical instrumentation for a μSR experiment.

4.1 Muon sources

Pulsed and continuous sources

The two main types of proton beams are pulsed, produced at synchrotrons, and (quasi-)continuous, produced at cyclotrons. These proton beams produce, as described in the previous chapter, pulsed or continuous pions and eventually muons, which exhibit certain advantages and disadvantages. The experiments presented in Paper III were conducted in the pulsed muon source at ISIS [66, 67]. The pulsed muon beam's high intensity results in high data acquisition rates since a large number of muons is implanted into the sample at each pulse. This allows us to create high quality spectra at longer times at $\approx$20 μs, where the signature of slower dynamic effects usually lies. However, the pulse width (about 100 ns) raises a limit to the time resolution at $\approx$0.1 μs, which discourages the use of a pulsed source to study fast depolarizing components in the muon spectra. Distortions can be induced in the spectra by a large number of decaying muons in successive pulses, leading to count losses from the detectors. This problem is handled by increasing the time interval between pulses and introducing a large array of detectors to distribute the workload of positron counts. Additionally, the pulsed beam does not allow us to regulate the beam spot size and reject individual events. To overcome this issue experiments are done using a fly-past setup, which allows the part of the beam not hitting the target to fly past and decay away from the detectors.

The continuous source characteristics complement many of the limitations of pulsed sources, and vice versa. In this case, the muons are implanted and positrons detected individually at each counting round. This drastically lowers the count rate and reduces the time window to $\approx$10 μs. Moreover, the rate is lowered so that no more than one positron is counted at a measuring cycle, otherwise the origin of the positrons may be

mixed. The time resolution is determined by the muon counter [Fig. 3.4] and electronics setup, extending down to ≈50 ps. This allows us to study fast relaxing components from strong magnetic moment systems. Individual unwanted counts from muons stopping outside the sample can be rejected in this case by the use of a veto detector behind the sample, allowing the study of samples of ≈1 mm^2.

It should be noted that continuous sources find application in time-differential measurements, whereas pulsed sources can be used in both time-differential and time-integral measurements, where there is no restriction on the number of the implanted muons. This flexibility, together with their pulsed form, allows the integrated polarisation to be measured against external stimuli like laser, RF field, pulsed magnetic field excitations etc.

Surface, decay and low energy muons

There are two main types of muon beamlines depending on the momentum of the decaying pions. The decay of pions at rest close to the surface of the target results in the production of surface muons. A surface muon beamline is characterized by a high spin polarization, since muons are perfectly polarized in a specific emission direction. The muon kinetic energy is set to $E_\mu = 4.12$ MeV, as discussed in Chapter 3. The calculated penetration depth from the stopping power of such muons is in the range of several hundred micrometers, setting limitations on the components of the sample environment that obstruct the beam. If a measurement requires such components, as in the case of measurements under high pressure with the use of pressure cells, then decay muons are preferred. Decay muons are emitted off pions that decay in flight. The emission directions with the highest spin polarization are forward and backward with respect to the pion momentum, however polarization is lower than with surface muons. The more energetic forward muons can penetrate several centimeters in a material, appropriate for thick bulk samples or thick sample holders. On the opposite case, for the study of nanometer-thick layers, surfaces or interfaces, we require low-energy muons in the range of eV-keV. There exist two such low-energy muon beamlines, the USM in J-PARC and LEM in PSI. The scheme pursued at J-PARC is the formation of thermal muonium from a pulsed muon beam crossing a heated tungsten foil, followed by the ionization of muonium with pulsed lasers. This process will leave the muon beam with an energy range of 0.1-30 keV and the polarization reduced by ≈ 50%. In PSI, the continuous muon beam is moderated through inelastic processes in a dense noble gas. The achieved energy reduction is in the range of 1-30 keV with small losses in polarization.

4.2 Sample environment

In Chapter 4 we presented a simplified model of a μSR spectrometer [Fig. 3.4]. In practice it is composed of a number of detectors in a specific geometry depending on the muon source and the adjoining instrumentation. The distance from the sample is also important, since charge particles like muons and positrons may feel a *Lorentz* force from a surrounding field and deviate from their path. For a pulsed source a large array of detectors is needed to facilitate the counting of many events. At a continuous beam there is no need for many detectors. During data analysis, the histograms from certain detectors can be grouped and treated as a forward and backward detector. Each detector is composed of a scintillator, a light guide and photomultiplier tube [Fig. 4.1(b)]. The detector system and associated electronics operate successively to complete a measurement. A Time-to-Digital (TDC)

converter, triggered by either a muon detector before the sample in continuous beam or an incoming pulse, sets the starting time for the measurement. The scintillator emits a light pulse when hit by the emitted positron. The photomultiplier converts the light pulse into a voltage pulse and then a discriminator is used to convert it into a logic pulse. The TDC can then count it as an event, add it to the respective histogram and time the end of the measurement. The end-station consists also of a cryostat or an oven and conventional or superconducting magnets, surrounding the sample in specific geometries.

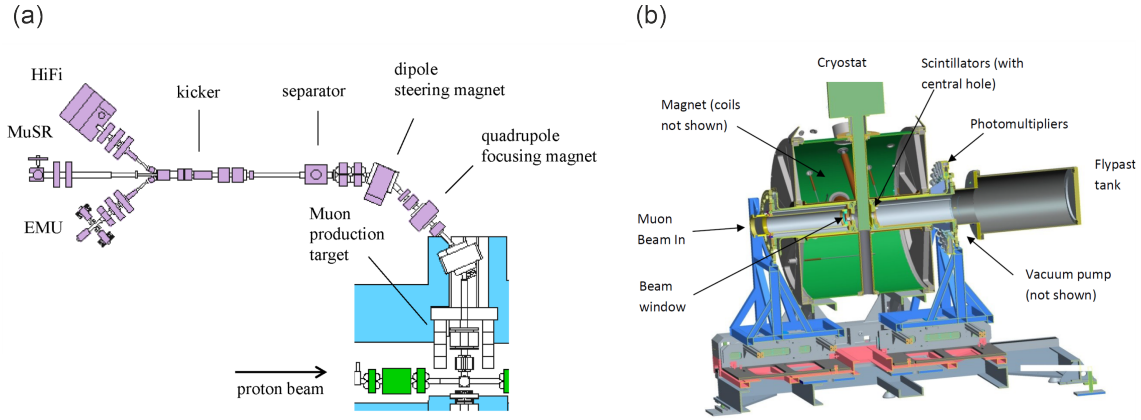

Figure 4.1: (a): Example of a muon beamline (ISIS) and typical installed components for muon beam transport, focus, decontamination and configuration.**(b):** The configuration of a μSR spectrometer. The sample is placed in the center of the beam path in the cryostat. Adapted from [68, 69].

Finally, an essential element integrated into a surface and low energy muon beamline, preceding the spectrometer, is a separator [Fig. 4.1(a)]. This apparatus filters charged particles not matching the velocity selected for the muons. This is achieved by employing perpendicular **E** and **B** fields, generating a *Lorentz* force that deviates the contaminant particles (mostly muons). Morover, this device can serve as a spin rotator. For TF measurements in a field perpendicular to the muon momentum the beam would be deflected from its path. Consequently, this device is used to rotate the muon spin perpendicular to its momentum, enabling the application of the TF field parallel to the beam without affecting its trajectory.

Chapter 5

Results

This chapter serves to summarize the primary experimental conclusions of the appended Papers I-V , as well as to provide a framework for the presented research. The examined samples include materials in powder form, single crystals and multilayered films with nanometer-scale thickness. In Papers I and II we investigate the emergent magnetic phases of transition metal double perovskite oxides $LaSr_{1-x}Ca_xNiReO_6$ resulting from cation substitution. In Paper V the magnetic ordering and spin dynamics of the transition metal tri-halide $CrCl_3$ are explored. In Paper III, we examine the ion kinetics within the hybrid organic-inorganic perovskite halides through successive structural transfromations, as influenced by anion substitution, temperature and illumination. Paper IV delves into the magnetic phases and spin dynamics in the multilayered heterostructure $[Co_{40}Fe_{40}B_{20}$ (0.8 nm)/Ru (1.4 nm)/Pt (2 nm)]x40. The foremost approach utilized in these investigations was the application of the μ^+SR technique, wherein measurements were conducted as a function of temperature and applied magnetic fields. These measurements were executed in both continuous and pulsed sources of high or low energy muons.

5.1 Magnetic phases and spin dynamics in polycrystalline metallic compounds

5.1.1 Introduction

Since the beginning of the 20th century, the progress in understanding the electronic structure as well as intra- and inter-atomic interactions in crystalline solids has allowed us to study in depth the origins and properties of magnetic, metal-based materials. The concept of alloying, practically known since ancient times - now understood at an atomic level, together with the combination of metals with nonmetals has led to an ocean of possible compound materials. On these compounds, researchers are experimenting with element substitutions, applied mechanical stress, the system's dimensionality, and their response to externally regulated parameters such as temperature and magnetic field. The goal is to discover their magnetic properties and adjust the contribution of different magnetic interactions that define them in order produce new, well-tuned functional materials for applications in electronic and spintronic devices.

One such class of materials are called perovskites, after the mineralogist *Lev Perovski*, and share a similar crystal structure with the archetypal calcium titanate $CaTiO_3$, discovered in the Ural mountains in 1893. Perovskite oxides have been extensively investigated the past 70 years, owing to their wide range of electrical and magnetic properties such as

metallic [70], semiconducting [71] or insulating behaviour [72], but also superconductivity [73], magnetoresistance [74] and ferroelectricity [75], as well as diverse and complex magnetic phases. This diversity is attributed to their structural malleability that allows them to accommodate almost all elements in the periodic table [76]. The perovskite structure is ideally cubic with a unit formula of stoichiometry ABX_3. The larger, 12-fold coordinated, A-site cations occupy the center of the unit cell, while the smaller, 6-fold coordinated, B-site cations occupy the corner positions, bonded to the X anions (typically oxygen or a halogen), forming a network of adjoining BX_6 octahedra. Often, the octahedra are tilted or twisted as a result of cation substitution, displacements or Jahn-Teller distortion. *Glazer* studied and classified the octahedral distortions into 15 distinct space groups [77, 78]. This structural tolerance permits the adoption of cations of different sizes and oxidation states that affect the electrical and magnetic properties of the system. Moreover, the formation of superstructures, termed double perovskites and so on, is possible.

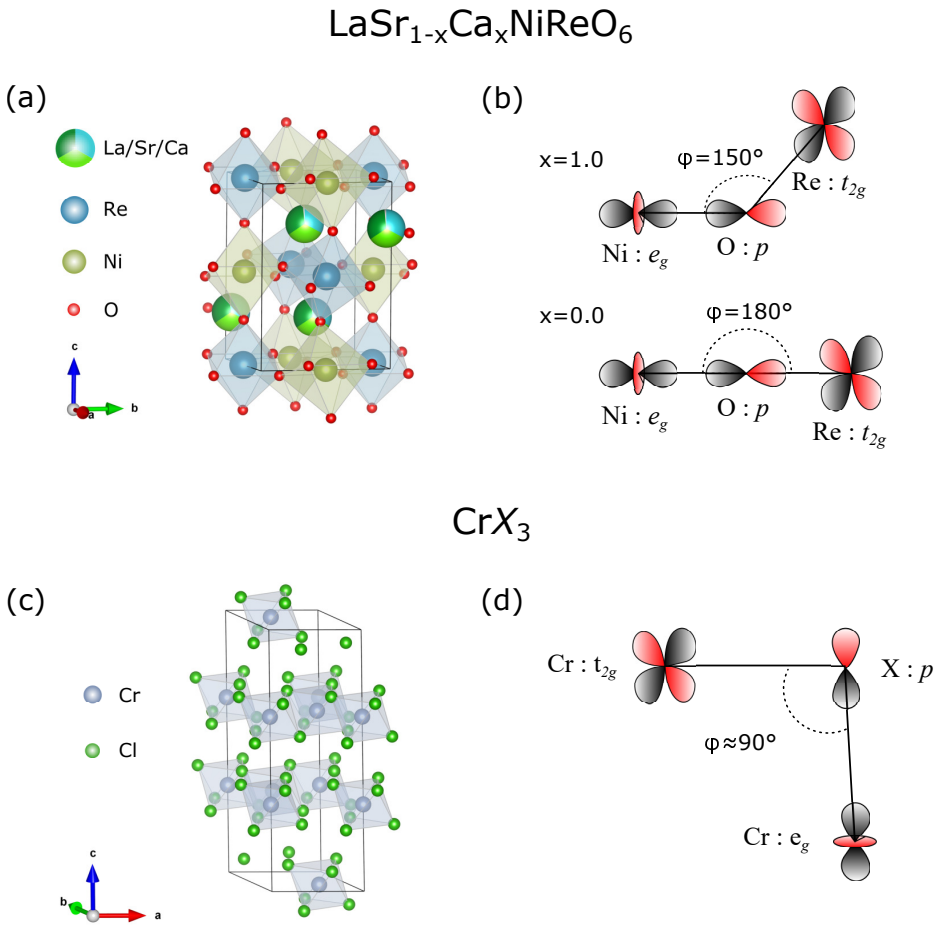

Figure 5.1: **(a)**: The double perovskite crystal structure of $LaSr_{1-x}Ca_xNiReO_6$ composed of La, Sr or Ca atoms in the cavities created by corner-sharing NiO_6 and ReO_6 octahedra. **(b)**: The Ni-O-Re atomic orbitals and bond angles depending on the substitution of Ca with Sr. **(c)**: The crystal structure of $CrCl_3$ composed of $CrCl_6$ octahedra arranged in layers, in a honeycomb lattice. **(d)**: The Cr-X-Cr atomic orbitals and bond angle.

The double perovskite (DP) structure has a general formula $AA'BB'O_6$ and staggered

rocksalt, columnar or layered ordering of the BO_6 and $B'O_6$ octahedra [Fig. 5.1 (a)]. Typically, the A/A' sites are occupied by either alkaline, lanthanide, or rare earths, while the B/B' sites host 3d, 4d, or 5d transition metals [76]. The type of sublattice arrangement of the B/B' cations, together with the selection of elements that offers a tunable B-O-B' superexchange interaction, result in a variety of physical properties [Fig. 5.1 (b)]. Additionally to the nearest neighbor (NN) superexchange interaction, which is expected to be dominant, the hamiltonian of these systems would also account for next-nearest neighbors (NNN) double-exchange interactions (B-O-B and B'-O-B'), as well as anisotropy terms arising from spin-orbit coupling (SOC) and dipolar interactions [76, 79, 80]. In Papers I and II we focus on the magnetic ordering of nickel/rhenium-based DP oxide samples. This group of perovskite materials exhibit rich magnetic phases due to the interactions between the strongly localized $3d$ electrons and more delocalized $5d$ electrons with strong spin-orbit coupling. Studies on other Re-based DP compounds have demonstrated high Curie temperatures, large magnetic anisotropy and large carrier spin polarization [81–85], all of which make the case of coupling among charge, spin and orbitals open for further research.

Transition metal trihalides (TMTH) is also a family of compound materials with a long history and interesting electrical and magnetic attributes. The first samples were fabricated during 1845 by *Claus* [86] and in the course of the 20th century several samples and studies where added [87–89]. TMTHs were initially deployed as metal-based catalysts in organic synthesis procedures. Nevertheless, since the discovery of the transport properties of graphene in 2004 by *Geim* and *Novoselov* [14], there has been rapid developments towards 2D magnetism, as the low dimensionality of a system may radically influence its physical properties. In this context, the study of TMTHs has lately resurfaced and samples are currently reexamined with respect to the emergent magnetic arrangements in their layered structure [90–92]. The general formula of TMTHs is MX_3, where M is occupied by a transition metal and X a halide ion. Here, we focus on the chromium-based group: (M=Cr, X=Cl, Br, I) and specifically $CrCl_3$ in Paper V. This group of chromium trihalides are insulating magnets and their magnetic properties strongly depend on the type of halide ion, therefore they are often studied in parallel [93–96]. Numerous investigations have also centered on the utilization of these materials in magnetic tunnel junctions and consequently their implementation in spintronic devices [97–99].

The CrX_3 crystals consist of stacked layers of Cr^{3+} ions arranged in a honeycomb lattice and surrounded by edge-sharing octahedra of X^- ions [Fig. 5.1 (c)]. In this 2D arrangement, the atoms of each layer are held together by ionic bonds while the successive layers are connected by the weaker *van der Waals* force, hence these materials are also termed "2D *van der Waals* magnets". A first order, structural phase transition from a monoclinic to a rhombohedral structure occurs at relatively high temperatures (at 210 K for CrI_3 [100], 240 K for $CrCl_3$ [87] and 420 K for $CrBr_3$ [89]), while a magnetic ordering emerges with further cooling ($T_C \approx 68$ K for CrI_3 [101], $T_C \approx 17$ K for $CrCl_3$ [102] and $T_C \approx 37$ K for $CrBr_3$ [103]). However, the characteristics of the magnetic ordering phases that develop below these critical temperatures is still under debate. In each layer, superexchange is again considered to be the decisive magnetic interaction between NN Cr^{3+} ions with crystal-field split atomic orbitals, mediated by X^- ions [Fig. 5.1 (d)] [104]. The hamiltonian of these systems is often composed of isotropic and anisotropic Heisenberg exchange terms, and a dipole-dipole interaction term [105]. However, alternative frameworks and exchange interaction terms have also been proposed [106–108]. The forementioned interactions define the ordering of spins and the anisotropy axis. These CrX_3 crystals exhibit a predominantly ferromagnetic intralayer spin ordering, with the easy axis of magnetization

being out of plane for CrI_3 and $CrBr_3$, and in plane for $CrCl_3$. Concerning the interlayer coupling, the link between the Cr^{3+} is a more complicated, super-superexchange, interaction mediated by two X^- ions. The stacking order is reported to play a crucial role in determining the strength and the sign of these interactions, resulting in either ferro- or antiferromagnetic ordering, an effect which makes CrX_3 an attractive material for use in layered heterostructures, in future applications [109, 110]. In conclusion, the intra- and interlayer magnetic ordering of CrX_3 is an active subject of research, exemplifying the role of dimensionality in intrinsic 2D magnets.

5.1.2 Summary of results

Magnetic phases of $LaSr_{1-x}Ca_xNiReO_6$

The research presented in Papers I and II aims to reveal the ordering and dynamics of multiple magnetic phases in $LaSr_{1-x}Ca_xNiReO_6$ DP oxide across a wide temperature range. The influence of cation substitution and resulting structural distortions on magnetic ordering, as well as the evolution of spin correlations with temperature, are observed. Previous studies by Jana *et al.* on samples from the same polycrystalline powder batch found the materials to be insulating magnets [111]. Both x-ray and neutron diffraction data were fitted under the $P2_1/n$ space group at all measured temperatures. However, bulk magnetometry and neutron diffraction results created uncertainty regarding the magnetic structure of the compounds [112]. Therefore, the current study aimed to investigate the magnetic ordering in these materials. In order to cover a wide frequency range in magnetic dynamics and verify the results, both bulk magnetometry and μ^+SR measurements were conducted in the temperature range of 2-300 K. These measurements revealed a series of magnetic phases that strongly depend on the substitution of cations on the A' site of the double perovskite. Papers I and II focus on the $x = 0$ and $x = 1$ compounds, respectively, and will be referred to as "LSNRO" and "LCNRO" for clarity.

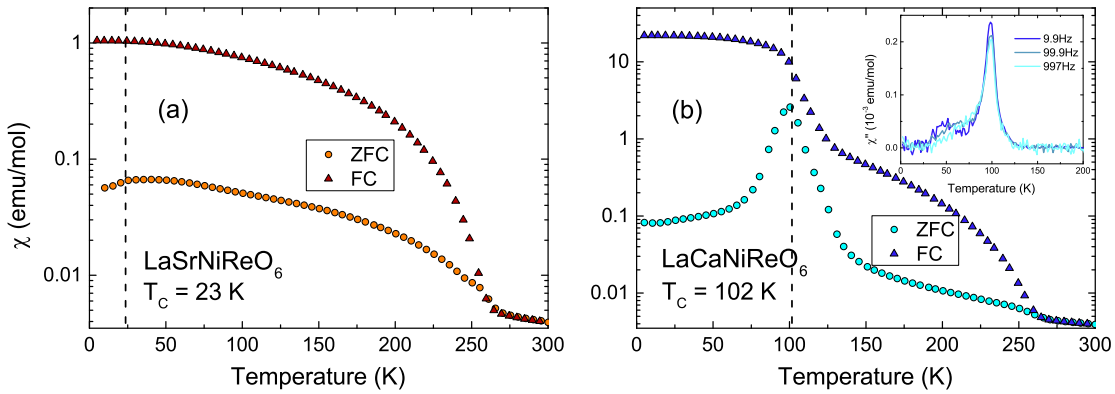

Figure 5.2: Temperature variation of d.c susceptibility in a zero-field-cooled (ZFC) and field-cooled (FC) process for **(a)**: $LaSrNiReO_6$ and **(b)**: $LaCaNiReO_6$. The inset displays the imaginary part of the a.c susceptibility in various frequencies. Adapted from [113, 114].

Both compounds exhibit magnetic ordering as a result of the interaction between the Ni^{2+} and Re^{5+} magnetic sublattices. In Chapter 2, we highlighted the exchange interac-

tions that predict ferro- or antiferromagnetism. The primary exchange interaction in this system is the superexchange interaction between the Ni and Re cations, which depends on orbital overlap and, consequently, on the Ni-O-Re bond angle. Previous studies have emphasized the effects of cation substitution on the magnetic properties of double perovskites through exchange interactions and spin-lattice coupling [115–118]. A substitution of Sr^{2+} with the smaller Ca^{2+} in the A' site, is likely to distort the octahedra and affect the B-O-B' bond angle. In the LSNRO crystal, a $\sim$180° angle is expected [Fig. 5.1 (b)], promoting a weak ferromagnetic interaction between Ni^{2+} half-filled e_g orbitals and Re^{5+} partially filled t_{2g} orbitals. In the case of LCNRO, the angle is narrowed, making antiferromagnetic interaction more favorable according to the Goodenough-Kanamori-Anderson (GKA) rules [119–122]. Furthermore, the interplay between first and higher-order neighbor interactions can effectively alter the type of magnetic ordering. Previous studies have reported geometrical frustration depending on the sign of the B-O-B' and B'-O-B' interactions [123, 124]. The strong SOC of the 5d transition metal (Re) creates a coupling between the spin structure and the crystal symmetry through the orbital momentum. This coupling may promote Jahn-Teller distortions of the octahedra and magnetocrystalline anisotropy, as indicated by the high remanence and coercivity values observed in both compounds.

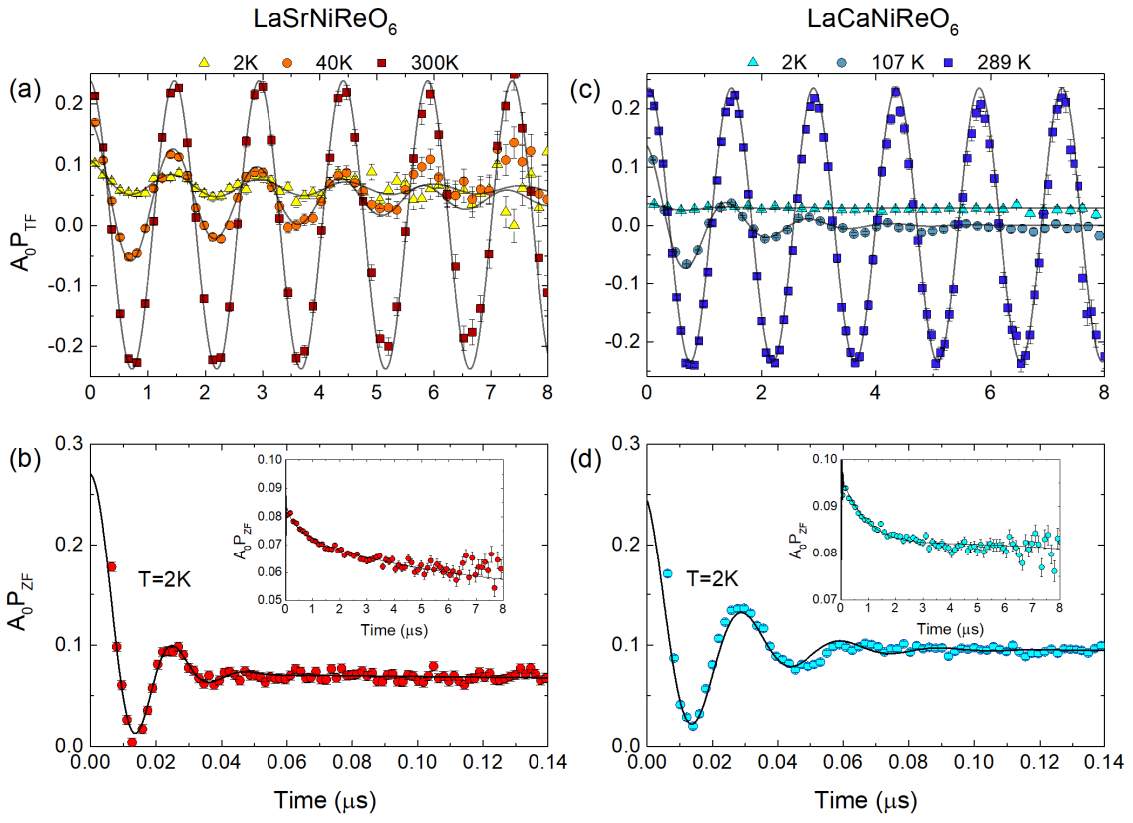

Figure 5.3: (a,b): Transverse field (TF=50 Oe) time spectra of $LaSrNiReO_6$ and $LaCaNiReO_6$ at selected temperatures exhibit damped oscillations with cooling. An offset is observed at lower temperatures. **(c,d)**: Zero field (ZF) time spectra of $LaSrNiReO_6$ and $LaCaNiReO_6$ in a short time frame reveal heavily damped oscillations at a temperature of 2 K for both compounds. The insets in panels (c) and (d) display the same data in the full time window. Adapted from [113, 114].

The results of bulk magnetic susceptibility measurements indicate the presence of two distinct magnetic transitions for both LSNRO and LCNRO compounds [Fig. 5.2 (a,b)]. In LSNRO, as the temperature decreases from 300 K, a first magnetic transition occurs at the bifurcation of the zero-field-cooled (ZFC) and field-cooled (FC) measurements at $T \approx 250$ K, and a second one at $T \approx 23$ K. On the other hand, in LCNRO, a first magnetic transition is observed also at $T \approx 250$ K, and a second one at $T \approx 102$ K. However, neutron diffraction measurements in LSNRO did not produce any magnetic Bragg peaks, while in LCNRO, these measurements reveal evidence of a magnetic ground state involving two antiferromagnetically coupled Ni and Re ferromagnetic sublattices [111–113]. In addition, a frequency-dependent shift of the peak maxima in a.c magnetic susceptibility was observed, from which a spin-glass ground state was suggested [112]. Therefore in our studies we employed μ^+SR at the continuous wave, surface muon instruments M20 (TRIUMF) and DOLLY (PSI), in an effort to identify and microscopically clarify the magnetic phases in this wide temperature range.

From the transverse field (TF= 50 Oe) measurements performed on each sample, we observe an oscillation that becomes increasingly damped with cooling and develops an offset at lower temperatures [Fig. 5.3 (a,c)]. To account for the fast and slow relaxation of the signal, we fitted the spectra with an exponentially relaxing cosine component and a simple exponential component respectively. The oscillatory component reflects the influence of the applied field on the sample, while the relaxing components arise from internal magnetic fields. The asymmetry parameter (A_{TF}) of the oscillatory component, which roughly corresponds to the paramagnetic fraction of the sample, exhibits a transition-like behavior indicating magnetic ordering, as shown in Figures 5.4 (a,d). Notably, we find that the full asymmetry is not recovered until above 250 K, indicating that the magnetic contributions in both samples persist up to this temperature, before entering a paramagnetic state. Furthermore, at low temperatures A_{TF} is nonzero, indicating small background contributions.

In the case of LSNRO, zero field (ZF) measurements were conducted at temperatures in the range of $2 \leq T \leq 250$ K. With regard to the ZF time spectrum at T_{base} =2 K, an oscillatory signal was observed, which is typically indicative of long range order in a material [Fig. 5.3 (b)]. This short time depolarization represents primarily the field components perpendicular to the initial muon polarization, while the spectrum at longer times reflects the field components parallel to the muon spin. The spectra were analyzed using an oscillating Bessel function with Gaussian relaxation and a general exponential, to account for depolarization at both shorter and longer times respectively. The precession frequency parameter (f) of the Bessel function exhibits a transition at $T_{\mathrm{C}}^{\mathrm{ZF}} = 23$ K , as determined by a power law fit according to mean field theory. This corresponds to the true critical temperature of the intrinsic magnetic ordering of the material [Fig. 5.4 (b)]. Two possible muon sites were identified at the electrostatic potential minima from density functional theory (DFT) calculations based on the crystal structure [125, 126]. However, since only one oscillating signal is observed, the two muon sites are considered to be magnetically similar. The relaxation rates λ_{IC} and λ_{S} reflect the internal field distribution and the spin-lattice dynamics respectively [Fig. 5.4 (c)]. With increasing temperature up to $T_{\mathrm{C}}^{\mathrm{ZF}}$, both λ_{IC} and λ_{S} increase, revealing a rise of internal field dynamics. At lower temperatures, although λ_{IC} decreases, it still remains significant at T =2 K, suggesting that the sample possesses a wide field distribution and is magnetically inhomogeneous even below the transition. This is also indicated by the fact that a Bessel function appears to be more suitable to represent the data, since this function is typically employed to describe a magnetic ordering with periodicity that is not commensurate with that of the crystal

lattice [127, 128]. At the same temperature range the slow relaxation component (λ_S) decreases with cooling towards a static state. From the microscopic (f) and bulk (χ) experimental results, the reduction of spontaneous magnetization at low temperatures suggests a ferrimagnetic type of ordering. Consequently, we propose that below $T_C^{ZF} = 23$ K, an incommensurate ferrimagnetic state takes effect.

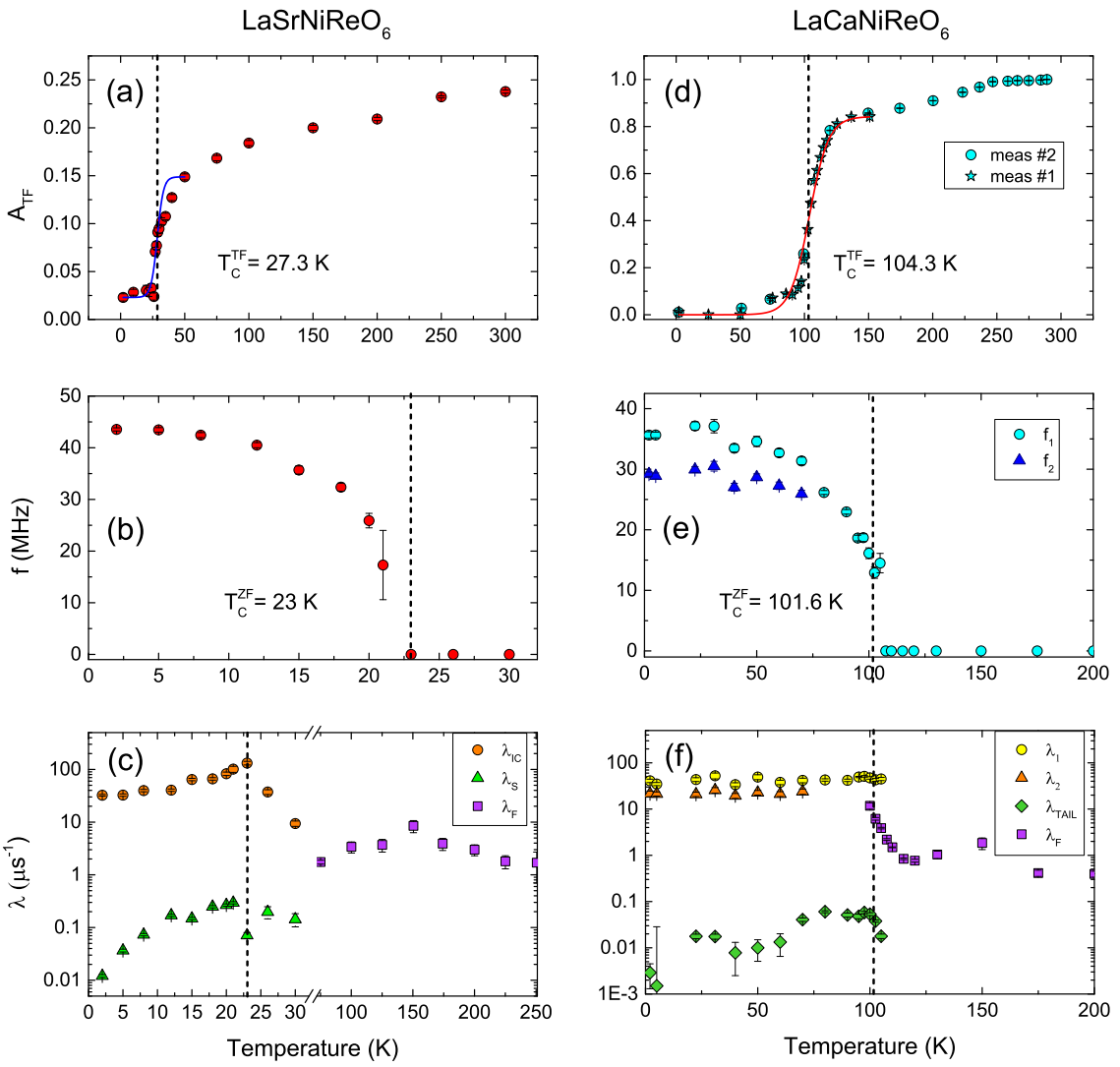

Figure 5.4: **(a)**: The TF asymmetry (A_{TF}), **(b)**: ZF precession frequency (f) and **(c)**: depolarization rate (λ) parameters of the depolarization function used to describe the $LaSrNiReO_6$ μ^+SR spectra. **(d-f)**: The respective components for $LaCaNiReO_6$. Adapted from [113, 114].

With respect to LCNRO, ZF spectra were recorded in the temperature range of $2 \leq T \leq 200$ K. In the short time scale of the spectrum, recorded at base temperature $T_{base} = 2$ K, a damped oscillation is evident as an effect of a static internal field distribution, perpendicular to the initial muon spin. At longer times, we observe a slower relaxation from the parallel field components [Fig. 5.3 (d)]. We initially attempted to fit the spectra with a single, exponentially relaxing, cosine function and a simple exponential tail, to describe the short and long time domain respectively. However, from DFT calculations

based on the crystal structure we predicted two possible muon sites. Based on the magnetic structure and assuming only dipolar contributions [111, 129] the calculated internal field frequencies for these muon sites are $f_1^{\rm calc} = 38.4$ MHz and $f_2^{\rm calc} = 28.9$ MHz. From further inspection of the Fourier transform with respect to temperature, we observed that the field distribution is asymmetric at base temperature in comparison to narrower and more symmetric distributions at higher temperatures, closer to transition. These indications lead us to use two oscillatory components instead, which also lead to an improved fit [Fig. 5.4 (e)]. The frequencies obtained at base temperature, $f_1 = 35.6(6)$ MHz $f_2 = 29.2(4)$ MHz, match the calculated $f_1^{\rm calc}$ and $f_2^{\rm calc}$ values. As temperature is increased though, these two frequencies become equivalent above ∼70 K and up to the transition temperature $T_{\rm C}^{\rm ZF} = 101.6$ K. A correlation is observed between the merging of the two frequencies and the appearance of a peak at lower frequencies, in the imaginary component of the a.c susceptibility [Fig. 5.2 (b-inset)]. It is known that the imaginary component is related to dissipative processes in the sample. A similar frequency-dependent peak arising below the magnetic ordering temperature and a decrease of the d.c magnetization has been observed in other systems and has been ascribed to a freeze-out of domain wall motion [130, 131]. This spin glass-like behavior, with associated slow magnetic relaxations, can occur from reorientation of a part of the magnetic moments. Therefore, we interpret these observations as the existence of partly disordered Ni or Re magnetic moments in the temperature range $70 < T < T_{\rm C}^{\rm ZF}$. A suggested scenario is that either the Ni or Re magnetic moments undergo ordering at $T_{\rm C}^{\rm ZF}$ and subsequently, the remaining experience a second ordering process at ∼70 K. The relaxation rates λ_1, λ_2, $\lambda_{\rm TAIL}$ of the fast and slow relaxing components all increase towards $T_{\rm C}^{\rm ZF}$ revealing an increase in the internal field dynamics [Fig. 5.4 (f)]. At low temperatures, the fast relaxation rates (λ_1, λ_2), which are related to the internal field distribution width, remain significant down to base temperature. The $\lambda_{\rm TAIL}$, which reflects the spin-lattice relaxation rate, exhibits a first drop between $50 < T < T_{\rm C}^{\rm ZF}$, which also hints towards an ordered and a disordered type of magnetic moments. Below 50 K the rate $\lambda_{\rm TAIL}$ decreases further towards a static state.

Above the transition temperature ($T_{\rm C}^{\rm ZF}$) the muon spectra from both materials present no oscillations but still consist of a fast and slow muon spin relaxing component. These temperature regions were described by the same relaxation function for both LSNRO and LCNRO, consisting of a fast relaxing exponential and Lorentzian Kubo-Toyabe (LKT) function. The LKT describes a dilute, random distribution of magnetic moments and the fast relaxing component possibly reflects the depolarization of muon in the vicinity of correlated moments. The relaxation rate $\lambda_{\rm F}$ increases sharply close to the motional narrowing limit of magnetic fluctuations at $T_{\rm C}^{\rm ZF}$ [Fig. 5.4 (f)]. This region could not be fitted with a KT function for LSNRO. In the temperature range $23 < T < 75$ K a stretched exponential function was used instead, which describes a distribution from magnetic entities with different relaxation times. These approaches effectively describe a similar picture for both samples. There exist regions of relatively strongly and weakly correlated moments that create a dense and dilute spin environment on a paramagnetic background. These correlations cease to exist with increasing temperature, and eventually both samples become paramagnetic above T=≃250 K.

Key Results:
The double perovskites $LaSr_{1-x}Ca_xNiReO_6$ (x=0,1) present similar dense and dilute magnetic phases above their ordering temperature and as high as T≃250 K. Below $T_{\rm C}^{\rm ZF} \simeq 23$ K for x=0 and $T_{\rm C}^{\rm ZF} \simeq 102$ K for x=1, the samples are ferrimagnetically ordered with a periodicity incommensurate and commensurate to the crystal lattice respectively.

Magnetic phases of $CrCl_3$

The 2D *van der Waals* magnet $CrCl_3$ was studied with μ^+SR at the continuous wave, surface muon instrument GPS at PSI [132]. The measured sample was in powder form, originating from small single crystals, fabricated by chemical vapor transport [133]. Being an intrinsic 2D material, the $CrCl_3$ crystal structure is composed of layers of Cr^{3+} ions in a honeycomb lattice, surrounded by six Cl^- ions in an octahedral coordination [Fig. 5.1 (c)]. Previous studies reported a structural transition of the honeycomb lattice from monoclinic to rhombohedral structure at 240 K [87]. Concerning the magnetic structure, neutron diffraction results exhibited a transition taking place at 16.8 K, where an intralayer Cr ferromagnetic coupling is taking place, while the interlayer coupling is antiferromagnetic [134]. The ferromagnetic coupling is also predicted by the GKA for a Cr-Cl-Cr superexchange interaction with a bond angle $\theta \approx 90°$. *Faraday* rotation, magnetization and heat capacity measurements during cooling have reported a first transition from a paramagnetic state to a quasi-2D ferromagnetic order of the Cr magnetic moments at 16.8 K, followed by an antiferromagnetic ordering due to the interlayer coupling at 15.5 K [102, 133, 135]. Additionally, the reported weak magnetic anisotropy and antiferromagnetic coupling allows a field of ∼1 kOe to polarize the magnetization in or out of the plane, which creates doubts about the stability of the proposed magnetic orders. Therefore, in Paper V we propose a μ^+SR microscopic study of the magnetic ordering in $CrCl_3$, in true zero field (ZF) and transverse applied field (TF) conditions.

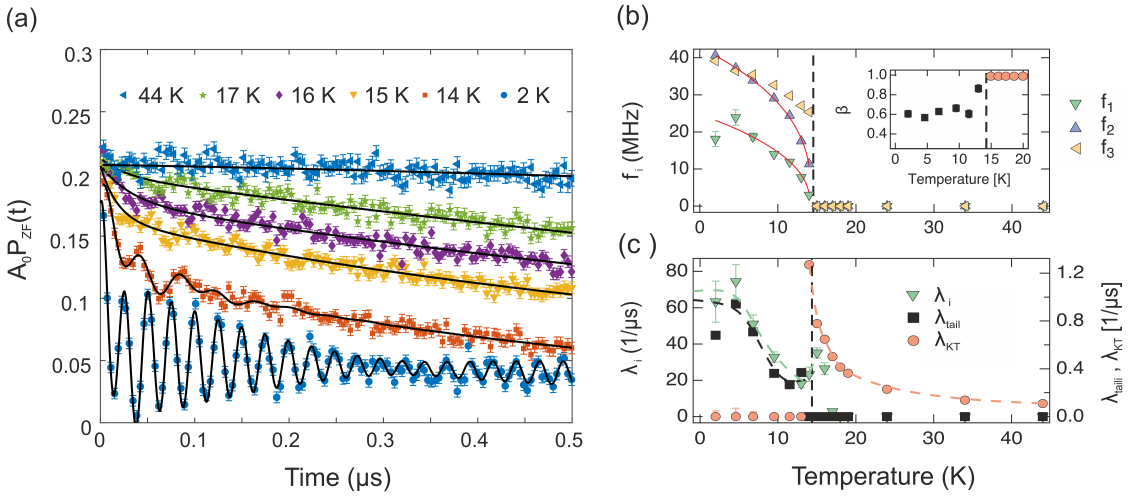

Figure 5.5: **(a)**: Zero field (ZF) time spectra of $CrCl_3$ at various temperatures. Damped oscillations appear below 15 K. The respective fit parameters of the depolarization function are presented as a function of temperature, **(b)**: the precession frequencies (f) and **(c)**: the relaxation rates (λ). The inset of panel (b) displays the stretched exponent (β). Adapted from [136].

The collected ZF spectra [Fig. 5.5 (a)] were fitted with, (1) two exponentially relaxing oscillatory functions reflecting the internal field components perpendicular to the initial muon spin, (2) a stretched exponential function in connection with the parallel internal field components, and (3) a Gaussian Kubo-Toyabe (KT) function that arises from the nuclear magnetic moments, which are considered to be static in the experiment's time frame. In addition, the probable muon sites were identified from the electrostatic potential minima through DFT calculations in the solved structure, and the expected internal

field frequencies ($f_{\mathrm{n}}^{\mathrm{calc}}$) were calculated based on dipole-dipole interaction and the magnetic structure at base temperature from previous neutron diffraction data [134]. Two muon sites were identified: μ_1 with $f_1^{\mathrm{calc}} = 12.73$ MHz, positioned in the interlayer space, and μ_2 with $f_2^{\mathrm{calc}} = 39.37$ MHz, positioned in the Cr planes. The resulting ZF fit parameters are presented in Figures 5.5 (b,c). The oscillating frequencies f_1,f_2 can be tracked down to base temperature and appear to originate from the calculated muon sites μ_1 and μ_2. A power-law function in accordance with mean field theory was selected to fit the observed transition. The fit exported a critical temperature $T_{\mathrm{C}}^{\mathrm{ZF}} \approx 14.33$ K and a critical exponent $\alpha = 0.36$ which suggests the presence of 3D fluctuations. Notably, a large depolarization rate λ_1 overlays f_1 in comparison to a smaller λ_2 at low temperatures (omitted in Fig. 5.5 (b) for clarity). In the event of out-of-plane fluctuations of local moments, the μ_1 sites would indeed be subjected to more pronounced fluctuations in the local field compared to μ_2, thereby accounting for the variation in relaxation rates between the two sites. Turning our attention to increasing temperatures towards $T_{\mathrm{C}}^{\mathrm{ZF}}$, we observe a peculiar behavior, where the dynamics seem to decrease. This decrease is accompanied by the emergence of a third frequency (f_3) above 9.5 K, which is uncertain whether it was present at lower temperatures or it is the result of a change in the magnetic or crystal structure that creates a new, magnetically distinct muon site. In CrI_3, there has been observed a coexistence of the two structural phases of the honeycomb lattice even at low temperatures [101]. However, a related magnetic or structural phase change has not been reported for $CrCl_3$.

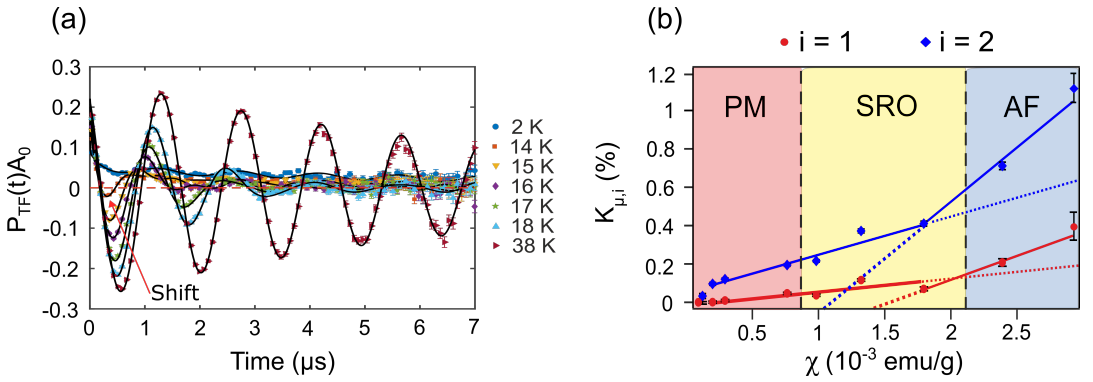

Figure 5.6: **(a)**: Transverse field (TF=50 Oe) time spectra of CrCl3 at selected temperatures. An oscillation frequency shift is apparent with decreasing temperature. **(b)**: Muon *Knight* shift (K_μ) versus the bulk magnetic susceptibility (χ). The colored areas represent the boundaries of each magnetic phase according to the ZF fitted spectra. An antiferromagnetic (AF) state for $T < T_{\mathrm{C}}^{\mathrm{ZF}}$. A short-range ferromagnetically ordered (FM-SRO) state $T_{\mathrm{C}}^{\mathrm{ZF}} < T \lesssim 18$ K. Finally a oaramagnetic (PM) state for $T \gtrsim 18$ K. Adapted from [136].

Let us now direct our focus towards the TF collected spectra illustrated in Figure 5.6 (a). The spectra were analyzed using three exponentially relaxing, oscillating functions, two of which correspond to the proposed muon sites (μ_1 and μ_2), and the remaining one representing an impurity contribution of approximately 3%. Throughout the cooling process, we observe a shift towards higher frequency values, accompanied by a reduction in the amplitude of the oscillation, which is attributed to the increasing internal field. The *Knight* shift (K_μ) was calculated as a function of temperature for both muon sites and juxtaposed with the bulk magnetic susceptibility (χ) at the same temperature values [Fig. 5.6 (b)]. As the

sample was cooled down from above the previously proposed first ordering temperature of 16.8 K, the applied field induced a positive *Knight* shift, indicating that the magnetization of the material is susceptible to align with an external field, as in a paramagnetic state. The microscopic origin of the temperature-dependent internal field consists of dipolar and hyperfine contact fields, both of which are related to the local magnetic susceptibility. The relationship between K_μ and χ is linear through the paramagnetic phase, but surprisingly, its gradient does not change around the proposed paramagnetic-ferromagnetic transition. Instead, it increases around T_C^{ZF}. However, a fully ordered quasi-2D ferromagnetic phase would result in a notable change in both the dipolar and hyperfine coupling, resulting in an increase in local spin density. The evolution of K_μ therefore indicates that the initial magnetic phase between $T_C^{ZF} < T \lesssim 18$ K is rather short-range ferromagnetically ordered. This is followed by an antiferromagnetic state for $T \leq T_C^{ZF}$, while a paramagnetic state is established at $T \gtrsim 18$ K.

Key Results:
The 2D *van der Waals* magnet $CrCl_3$ is found to be in a paramagnetic phase for $T \gtrsim 18$ K, followed by a short-range ordered ferromagnetic phase at $14 \lesssim T \lesssim 18$ K and an antiferromagnetic phase at $T \lesssim 14$ K. The lower-temperature antiferromagnetic phase demonstrates high dynamics, which decrease with increasing temperature.

5.2 Ion kinetics in hybrid organic-inorganic perovskite single crystals

5.2.1 Introduction

Another group of materials with the perovskite crystallographic structure ABX_3 are hybrid organic-inorganic perovskites (HOIP). An organic monovalent ion occupies the A site, confined by a cage of edge-sharing octahedra of inorganic divalent and monovalent ions that occupy the B and X sites respectively. HOIPs are arguably the most prominent materials in the perovskite family due to their promising photovoltaic properties and prospect of application in solar cells. In photovoltaic research, hybrid perovskite solar cells have displayed a dramatic increase in power conversion efficiency over the last decades, from a 3.8% first reported by Miyasaka et al. in 2009 [137], to current values being 26.1% for single-cell configuration and 33.9% for tandem perovskite/Si configuration [Fig. 5.7 (a)].

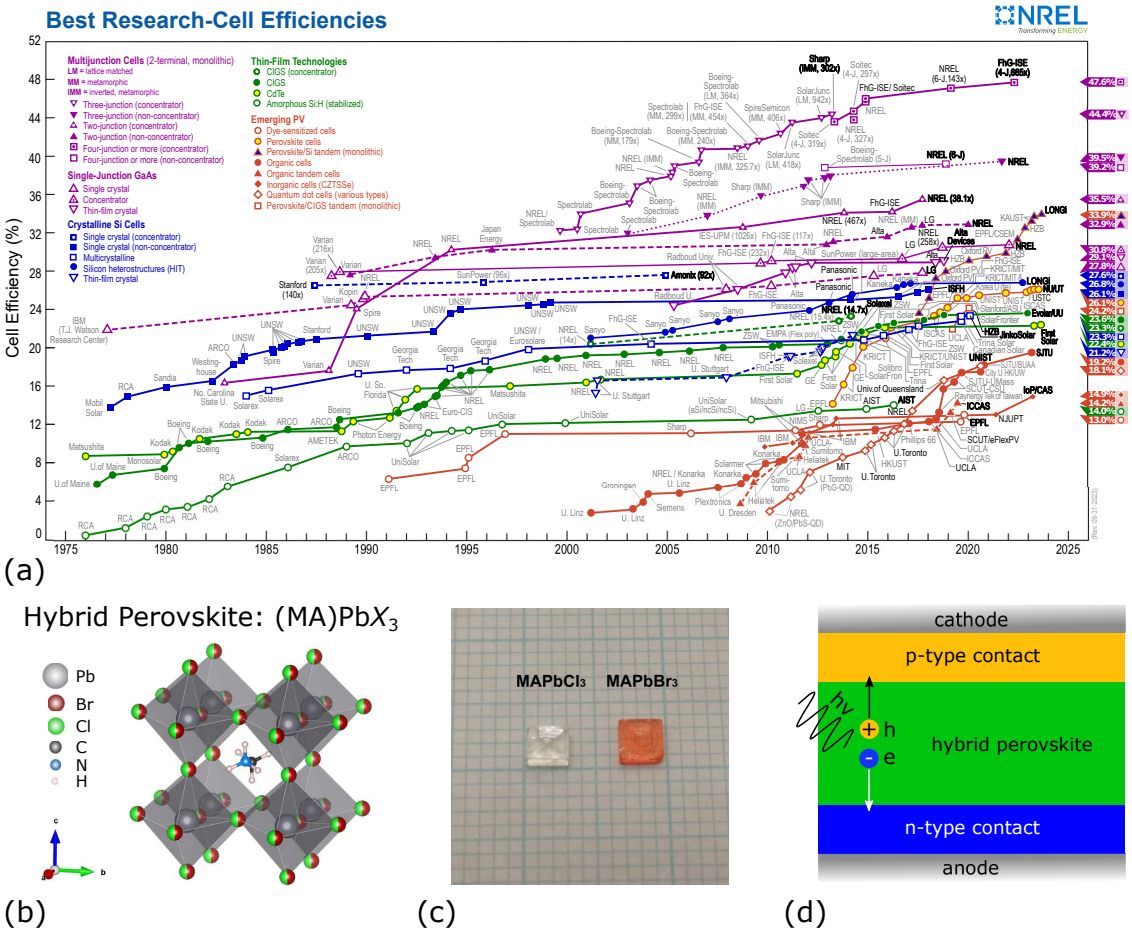

Figure 5.7: **(a)**: Timeline chart of record solar-cell efficiencies, reproduced from NREL [138] **(b)**: Crystal structure of the $(MA)PbX_3$ (X = Br, Cl) hybrid perovskite. **(c)**: A selection of $(MA)PbCl_3$ and $(MA)PbBr_3$ single crystals. **(d)**: Conceptual thin-film perovskite solar cell where charges are generated and extracted from the perovskite layer.

The rising trend in efficiency combined with their adjustable intrinsic properties, an effective, facile and low cost fabrication and assembly [139–141] drive their research as a sustainable alternative of silicon cells [Fig. 5.7 (d)].

The first HOIP solar cell in 2009 was based on the methylammonium ($CH_3NH_3^+$) lead (Pb^{2+}) iodide (I^-) material [137] and together with its halide species alternatives, either bromide (Br^-) or chloride (Cl^-), $(CH_3NH_3)PbX_nY_{3-n}$ are continuously studied ever since [Fig. 5.7 (b,c)]. The semiconducting properties of HOIPs occur in the inorganic framework. With halide doping or substitution their energy band-gap can be tuned between 1.68 eV for I, 2.20 eV for Br and 2.88 eV for Cl, leading to an adjustable light absorption range that covers the whole visible spectrum with high absorption coefficients [142–144]. The methylammonium (MA) lead halide group displays photo-generated charge carrier with high carrier mobilities [145] and long diffusion lengths $> 100\mu$m in single crystals, extracted from photoluminescence measurements [146–149]. However, the underlying mechanisms that enable these superior physical properties are still under debate.

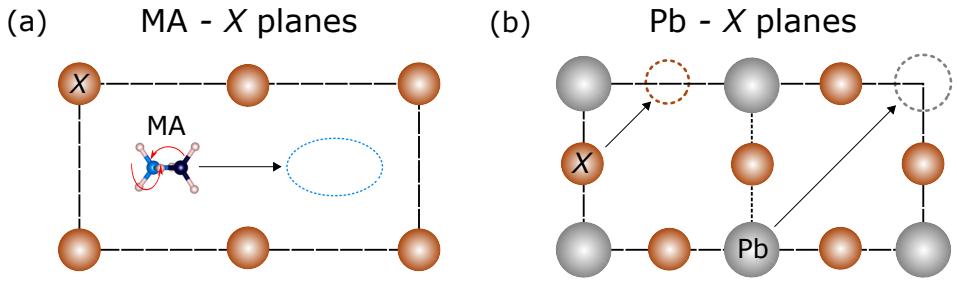

Figure 5.8: (a): Schematic representation of the MA molecule rotations and migration in the crystal lattice. **(b)**: Diffusion of the halides (X) or lead (Pb) in the crystal. The driving forces of ionic diffusion can be the electric field, the thermal gradient, the concentration of moving ions, lattice defects or stress, etc. Reproduced from [150].

The appearance of long diffusion lengths can be partially attributed to the low contribution of defects, with shallow energy levels, to carrier recombination [151]. Nevertheless, transport measurements indicate the presence of an internal mechanism suppressing electron-hole interactions, which is probably related to the MA molecular fluctuations and will be discussed further below [152, 153]. The organic cations can reorient rapidly with reported relaxation times between 0.1-28 ps [154]. Quasielastic neutron scattering, nuclear magnetic resonance and complex permittivity measurements have focused on these MA motions in relation to the structural phase transitions observed in X-ray diffraction and calorimetry measurements, in a temperature range of 1-400 K [155–159]. Three phases are identified with increasing temperature, an orthorhombic, followed by a tetragonal, followed by a cubic phase, where the MA molecule motions are believed to control the structural stability of the crystals [160, 161]. Halide diffusion is another source of instability leading to degradation of the crystal. Halide ions are found to be the most mobile species in the crystal [162, 163]. The migration activation energy grows gradually larger from Cl^- to Br^- to I^-, while the diffusion coefficient decreases due to smaller entropic contributions [164–166]. In parallel, the halide selection affects the migration density and fluctuations of MA^+, thus affecting the intrinsic stability of the system. The ionic migration and fluctuations also partly affect the charge transport performance of HOIPs, as reflected in a frequency dependence in permittivity and hysteretic behaviour of the

$I - V$ characteristic curves [162, 167]. Therefore, this matter of stability that arises from the intrinsic ion dynamics, together with extrinsic instabilities due to humidity, heat and constant illumination [168] pose the main challenges for perovskite solar cells.

5.2.2 Summary of results

The research presented in Paper III focuses on the kinetics of ionic species in hybrid organic-inorganic perovskite single crystals $(CH_3NH_3)PbX_3$ for X=Br, Cl, and how these evolve with temperature and are influenced by illumination. For the presented μ^+SR measurements we took advantage of the high counting rates acquired with the use of a pulsed muon source, at the EMU instrument (ISIS). As these materials are not expected to exhibit magnetic ordering, a high time resolution for fast relaxing components is not required. Instead, the goal is to investigate the dynamics of local nuclear magnetic fields resulting from structural transitions, fluctuations of the MA molecule, and ion diffusion. To accomplish this, TF, ZF, and LF measurements were conducted as a function of temperature in the T=30-340 K range, both in the dark and in an illuminated environment.

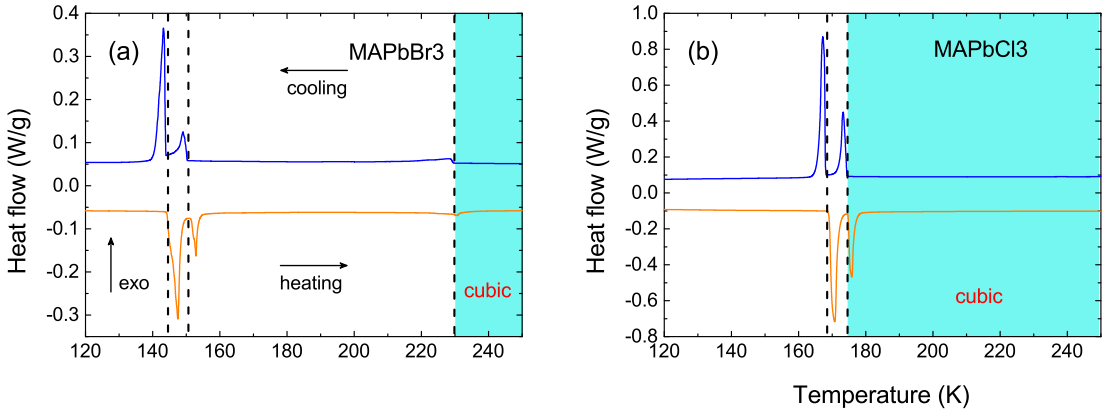

Figure 5.9: Differential Scanning calorimetry (DSC) thermograms of $MAPbBr_3$ and $MAPbCl_3$. **(a):** The exothermic and endothermic peaks correspond to a structural transition from cubic to tetragonal phase, followed by a transition to an incommensurate crystal phase, and finally an orthorhombic phase at low temperatures. **(b):** The peaks denote a cubic-tetragonal followed by a tetragonal-orthorhombic structural transition. Adapted from [169].

Previous studies have reported that these materials undergo a series of structural transitions below 300 K [158, 159]. To verify these structural phases, we performed Differential Scanning Calorimetry (DSC) [Fig. 5.9 (a,b)] and X-Ray Diffraction measurements on our samples. Our results showed that the $MAPbBr_3$ crystals have a cubic symmetry at room temperature. Below $T_{C2} \approx 230\ K$, the crystals adopt a tetragonal structure until an incommensurate phase transition ($T_{Ci} \approx 150\ K$) eventually leads them to an orthorhombic phase below $T_{C1} \approx 145\ K$. The $MAPbCl_3$ crystal assumes similar structures at different temperatures. A cubic-tetragonal transition appears at $T_{C2} \approx 180\ K$, followed by a tetragonal-orthorhombic transition at $T_{C1} \approx 175\ K$.

In light of the current research and the questions raised regarding the ionic motion and its effect on the HOIP's properties, we aimed to study the effect of illumination on the crystals' dynamic processes with μ^+SR. We initially measured the samples in a dark

environment, under TF, ZF, and LF configurations, in a temperature range of 30-340 K. A second round of measurements followed, where the samples were illuminated by a XENON flash lamp with a spectral distribution of 250-1020 nm that covers the absorption spectra of these samples [149, 170]. We collected spectra during two periods of 10s, light-on and light-off, where 500 muon pulses were recorded in each period. It appears that during these successive light on/off measurements, ions could not return to a steady state since the recorded ZF and LF spectra were almost identical for these two periods. However, the light-on spectra and especially their fitting parameters present suggestive differences in comparison to the initial recorded spectra in a dark environment.

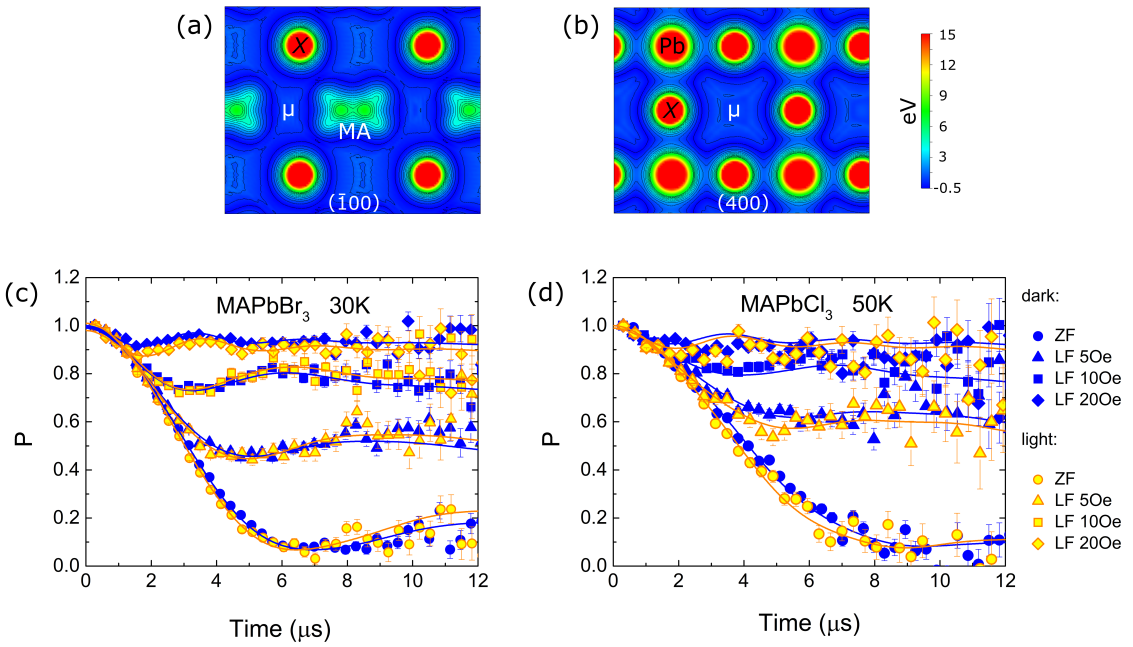

Figure 5.10: (a,b): Examples of probable muon sites in lattice planes where the electrostatic potential minima are observed. Zero field (ZF) and longitudinal field (LF= $5, 10, 20$ Oe) time spectra recorded at **(c):** T =30 K for $MAPbBr_3$ and **(d):** T =50 K for $MAPbCl_3$, in the dark and under illumination. Adapted from [169].

Figures 5.10 (c,d) display examples of the ZF and LF spectra at the lowest recorded temperatures. These spectra were fitted with a dynamic Gaussian Kubo-Toyabe function and a constant background component, permitting the identification and tracking of both static and dynamic field sources of the muon depolarization signal. The exported parameters, field distribution width (Δ) and field fluctuation rate (ν), are illustrated in Figures 5.11 (a-d). The drops in Δ correspond to the structural transition temperatures, an expected behavior since a structural change modifies the local nuclear fields experienced at each muon site. The expected muon sites were identified from the electrostatic potential minima calculated with DFT for all crystal symmetries [Fig. 5.10 (a,b)]. However, the calculated values of a static Δ originating from the present nuclear moments do not reproduce the experimental results beyond the orthorhombic phase. Previous research has been focused on the evolution of MA rotations with increased degrees of freedom through each structural transition [171]. If one considers fluctuations of the MA molecule and excludes the H, C and N nuclear moments from the calculation, then the motionally narrowed Δ values for $MAPbBr_3$ approach the experimental values as MA rotations are enhanced

with increasing temperature [Fig. 5.11 (b)]. In contrast, the calculated static Δ values for $MAPbCl_3$ show a better agreement with the experimental results, as the lighter and more electronegative Cl form stronger hydrogen bonds with MA, stabilizing the structure. Nonetheless, we expect the peaks in ν around the structural transitions, especially T_{C1}, to stem from the activation of MA fluctuations. An enhancement and shift of the peak to lower temperatures are observed in ν values with illumination, accompanied by shifted and decreased Δ values. The calculated activation energies below T_{C1} are reduced with illumination in both samples.

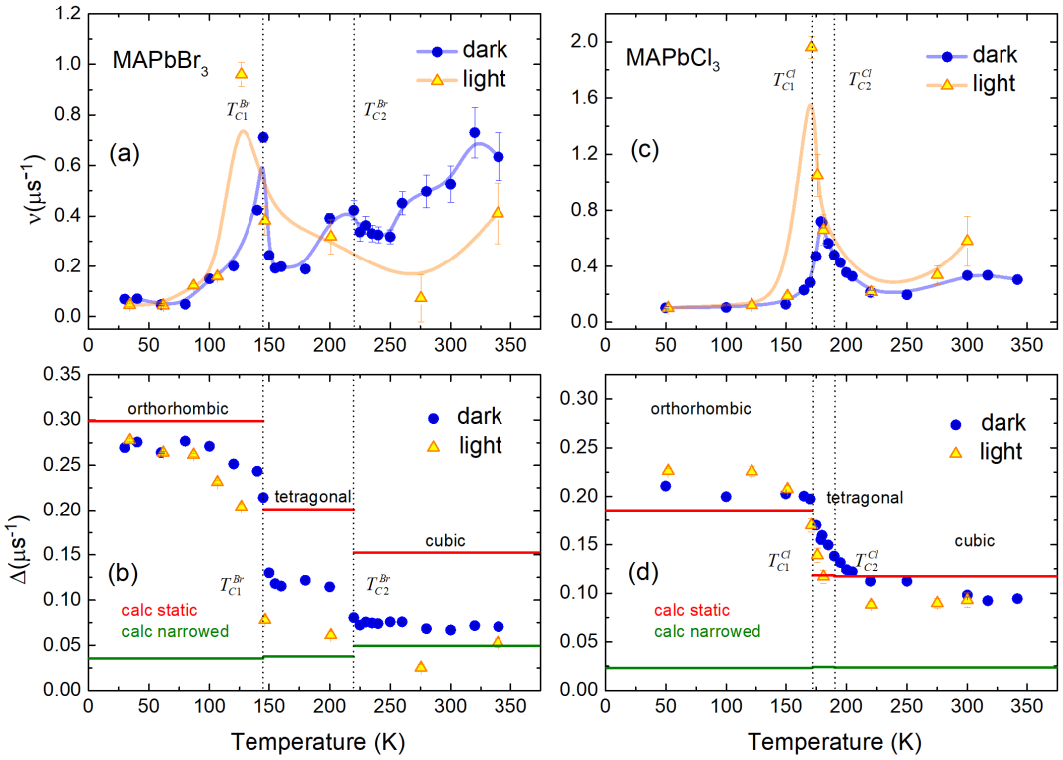

Figure 5.11: Temperature dependent **(a,c):** field fluctuation rate and **(b,d):** field distribution width of $MAPbBr_3$ and $MAPbCl_3$, in dark and illuminated environment. Adapted from [169].

Our analysis suggests that the observed MA fluctuations begin at lower temperatures and drive the structural transition. Quasi-elastic neutron scattering measurements in the sister compound $MAPbI_3$ exhibit a steep reduction in the relaxation time of MA rotation around the C_3 axis and the onset of C_4 rotations at T_{C1}, which supports this conclusion [172, 173]. For $MAPbBr_3$ in the dark environment, a second local ν maximum appears at T_{C2}, where a decrease in the relaxation times of MA C_3 and C_4 rotations is also expected. However, the limited number of collected temperature points and the proximity of the two structural transitions in $MAPbCl_3$ did not allow for the observation of a second peak in the Cl sample and the illuminated measurements. At higher temperatures, in the cubic phase, we attribute the further increase of ν primarily to migration of the halides, which are the most mobile ionic species [150, 164, 174, 175].

Additionally to the correlations between ν, Δ and the relaxation time of MA rotational motions, a correlation has also been observed with dielectric permittivity measurements. The MA cation possesses a permanent electric dipole moment, the fluctuations of which

can influence changes in the dielectric properties of these materials. A sudden increase in the dielectric permittivity is observed at the structural transition temperatures of both samples [157, 176], which can be microscopically understood as an alignment of the MA dipoles facilitated by molecular rotations. Based on this premise, the Coulomb interaction between photo-induced carriers and MA^+ could lead to dipole reorientation and a dynamic screening, thereby explaining the observed long carrier lifetimes. Within this picture, the effect of illumination appears to enhance this mechanism by both inducing carriers and enabling MA fluctuations for the formation of polarons.

Key Results:
In hybrid organic-inorganic perovskite single crystals $(CH_3NH_3)PbX_3$ (X=Br, Cl), molecular fluctuations, which are moderated by the choice of halogen ion, determine the observed structural transitions. Under illumination the molecular fluctuations appear enhanced, indicating an interaction between photogenerated carriers and methylammonium ions.

5.3 Magnetic phases of skyrmion-hosting multilayer superstructures

5.3.1 Introduction

Chirality is a universal phenomenon in nature, manifested as a breaking in mirror symmetry similar to the inverted mirror image of our palms [177, 178]. In magnetic materials, chiral arrangements of atomic magnetic moments emerge as a consequence of the DM antisymmetric exchange interaction which promotes a non-collinear alignment of neighbouring moments [35, 179, 180]. Versions of this interaction appear in systems lacking inversion symmetry [Fig. 5.12 a,b], such as certain 3D crystalline solids, or at the interfaces of 2D, nanometer thick, magnetic multilayered films [181]. Many types of chiral spin textures can be formed depending on the orientation of the short and long range exchange interactions and their synergy with dipole interactions ,magnetic anisotropy and the Zeeman effect [182, 183]. Among the various non-linear spin configurations, including cycloidal or helicoidal domain textures, magnetic vortices and bubbles, the formation of self-preserving and self-localized spin textures known as skyrmions are of particular interest [184]. Two general types of skyrmions exist: the Bloch-type, where spins rotate perpendicularly to the domain-wall and Néel-type, where the spins rotate parallel to the boundary [Fig. 5.12 c,d]. Bloch-type skyrmions are favored in 3D chiral magnets, while the Néel-type most commonly appears in multilayer interfaces [185–187].

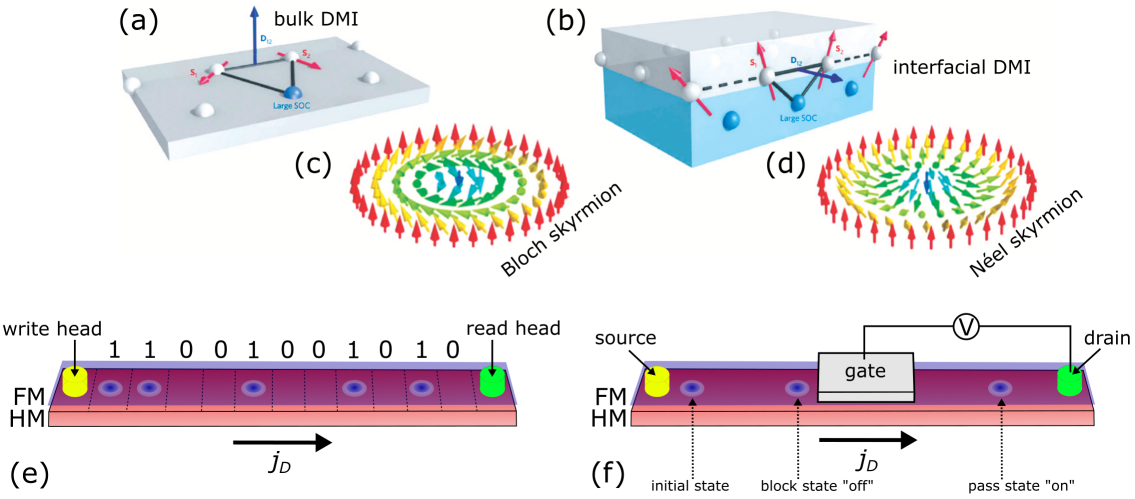

Figure 5.12: **(a)**: Orientation of the DM-Interaction vector in a bulk system with breaking of inversion symmetry in the lattice and **(b)**: in an layered system with breaking of inversion symmetry across the interface. **(c)**: A CW Bloch-type skyrmion, typical in bulk systems. **(d)**: A CCW Néel-type skyrmion, typical in interfacial systems. Panels a-d are adapted with permission from [188]. **(e)**: Conceptual storage device utilizing skyrmions, known as "racetrack memory". **(f)**: Conceptual voltage-gated skyrmion transistor. The skyrmions are created by a spin polarized current injector, driven by a vertical spin current and read through a magnetic tunnel junction.

Skyrmions are characterized by their nm-scale size, a signature chiral structure and topologically protected stability. The possibility to stabilize skyrmions at zero applied field

and at room temperature, while nucleate or drive them with femto/attosecond laser pulses or low current-densities , are promising properties for application in future non-volatile and ultra-fast storage and logic devices [Fig. 5.12 e,f] [189–191]. However, manipulation of the magnetic phases and stabilization of skyrmions in the hosting materials have proven to be a real challenge for the skyrmionic community.

Here we focus on the thin-film, multilayered skyrmion host [$Co_{40}Fe_{40}B_{20}$ (0.8 nm)/Ru (1.4 nm)/Pt (2 nm)]x40. A perpendicular magnetic anisotropy is expected from the large spin orbit coupling of Pt. Apart from Heisenberg and DM interactions around the CoFeB/Pt interface [192] , an interlayer, indirect exchange RKKY interaction is provided through the Ru/Pt layers by conduction electrons. The RKKY coupling between the CoFeB layers can be ferromagnetic/antiferromagnetic depending on the thickness of the Ru and Pt layers [193, 194]. Through the type of layer materials, the thickness, and number of repetitions one can control the interactions present in the system, which in turn determine the form of the chiral structures. Interlayer effects result in the formation of 3D, columnar skyrmion structures which depend on the number of repetitions [195, 196]. The multilayer repetitions are expected to enhance the stability of the skyrmion structures through increasing their annihilation energy, however they also enhance the interlayer dipolar interactions [187]. When the dipolar effects dominate, the chirality of the skyrmion structure may transition from a CCW to a reverse, CW (or vice-versa) along the perpendicular direction of the multilayer [197]. The magnetization curve of the magnetic layers and stabilization of a skyrmion lattice phase with or without field can be tuned to the extent that the strength of the aforementioned interactions is controlled [198–202]. To this end, extended studies and sampling of the magnetic phases appearing in the family of multilayered skyrmion hosts are required.

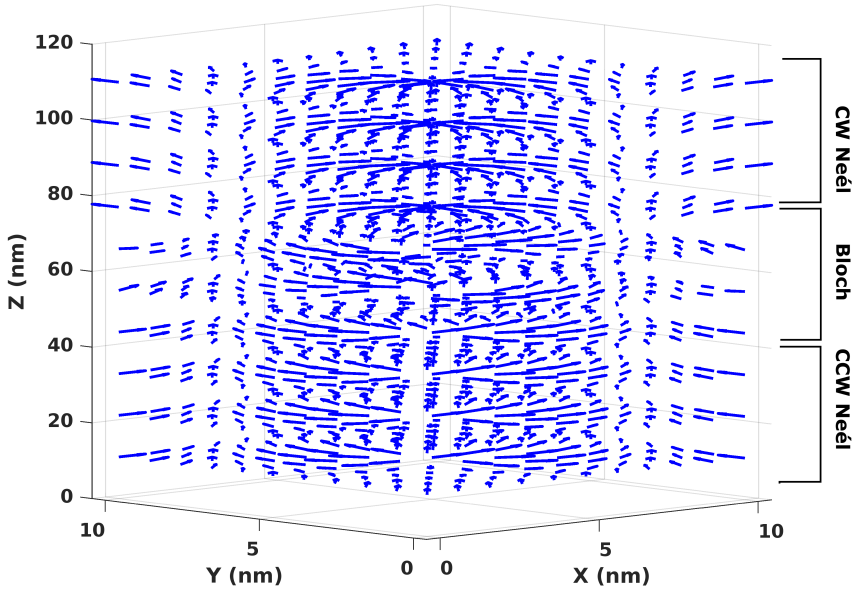

Figure 5.13: Simulated illustration of a columnar skyrmion structure as function of depth (z direction) in a multilayered system with multiple repetitions of the magnetic layer. The chirality of skyrmions transforms from CCW to CW through a Bloch-type transition along z.

5.3.2 Summary of results

The studies presented in Paper IV concern the magnetic phases of the $Pt/Co_{40}Fe_{40}B_{20}/Ru$ multilayer in a superlattice of 40 repetitions. The sample's bulk magnetization was initially measured by SQUID and alternating force magnetometry [Fig. 5.14(a)]. A perpendicular anisotropy is observed from the out-of-plane (OOP) and in-plane (IP) hysteresis curves, which is considered to stem from the large SOC of Pt. In magnetic force microscopy (MFM) scans [Fig. 5.14(b-e)], taken at room temperature for selected OOP fields directly below saturation, we observe transitions from a field polarized state to a disordered skyrmion lattice (SkL) and a labyrinth domain state.

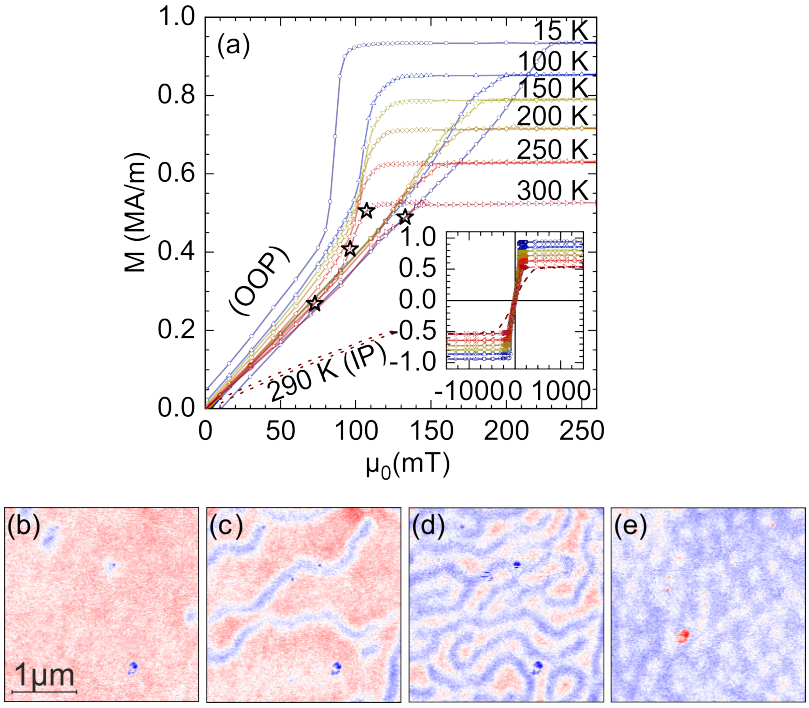

Figure 5.14: **(a)** Hysteresis curves for out-of-plane (OOP) and in-plane (IP) applied field, in the 15-300 K temperature range. The star points correspond to the **(b-e)** MFM phase maps at 300 K, for applied OOP fields of (b) 107 mT, (c) 96 mT, (d) 72 mT and (e) -133 mT. The color-scale corresponds to 1° phase range.

To expand our studies in the micro-scale and measure potential high-dynamic magnetic effects we performed an experiment at the low-energy muon (LEM) instrument (PSI). Highly energetic muons may fly through an extremely thin sample, therefore thin film samples are typically measured at a LEM instrument, where the muon energy can be reduced to a few keV's. Additionaly, in magnetic multilayers the magnetization varies from the surface to the bulk, and in layers of different composition. By selecting the muon energy we control the stopping depth that allows us to probe the desired volumes of our sample. For the studied sample we performed the experiment at $E_\mu = 15$ keV which gives a stopping distribution with a mean value at 51 nm. In this experiment we also used the spin-rotator module in order to perform measurements with the muon spin polarization in-plane (IPP) and out-of-plane (OOPP) with respect to the sample's surface.

Measurements were performed in ZF, LF and TF geometry for fields in the range of the skyrmion nucleation field and temperatures in the 50-570 K range. The TF measurements

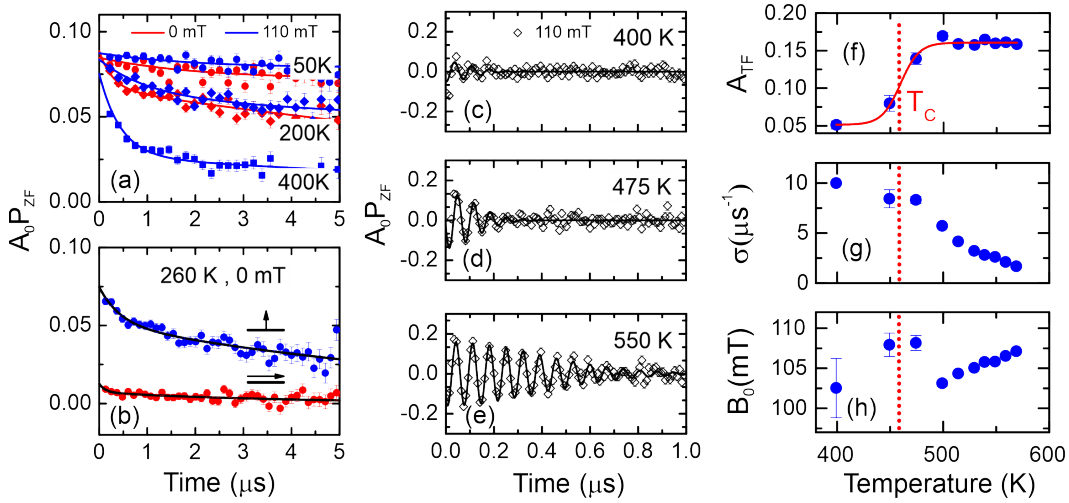

Figure 5.15: **(a)** Time spectra of ZF and LF ($B_{\mathrm{LF}} = 110$ mT) measurements at selected temperatures. **(b)** Time spectra of ZF measurements at 260 K, for out-of-plane and in-plane spin polarization with respect to the sample surface. **(c-e)** Time spectra of TF measurements at selected temperatures around T_{c}. **(f-h)** Temperature dependence of the fit parameters: asymmetry (A_{TF}), Gaussian standard deviation (σ) and average local field (B_0), for TF ($B_{\mathrm{TF}} = 110$ mT) measurements.

(400-570 K) produced an increasingly damped oscillation with cooling [Fig. 5.15(c-e)], fitted by an oscillatory component with a Gaussian relaxation. The asymmetry parameter (A_{TF}) evolution with temperature shows a transition at $T_{\mathrm{c}} = 460$ K as the field distribution (σ) widens with cooling due to the rise of internal magnetic fields [Figs. 5.15(f,g)]. From measurements of the IPP vs OOPP spectra in ZF well below T_{c} we determined that the local magnetic fields are predominantly oriented out-of-plane due to the very fast depolarization observed in the IPP geometry [Fig. 5.15(b)]. The measurements were continued in OOPP geometry for ZF and LF, in the 50-550 K temperature range. The application of a series of increasing fields in LF geometry appears to only weakly decouple the muon spins and lead towards higher asymmetries, as expected for static internal fields [Fig. 5.15(a)]. This is an indication of dynamical fields at the muon sites. The ZF and LF spectra for OOPP were fitted with a fast and a slow relaxing exponent, suggesting two distinct magnetic environments for the muon in the studied volume. The depolarization rate λ_{F} of the fast relaxing part describes mainly the field distribution. It originates from field components perpendicular to the OOPP, thus in the sample plane. The slow relaxing part is characterized by λ_{S}, which corresponds to dynamics in the system [Fig. 5.16(b,c)]. Both λ_{S} and λ_{F} exhibit broad peaks around T_{c}, at the broadening of the internal field distribution. The corresponding transition is identified by transverse magnetoresistance measurements as field polarized towards a state of elongated magnetic domains, with an intermediate SkL metastable phase depending on the applied field. At lower temperatures, λ_{S} and λ_{F} appear to form a second peak which may reflect an ordering of the elongated domains. It is noted that the asymmetry of the slow relaxing part A_{slow} is present at all temperatures and dominates with cooling [Fig. 5.16(a)], which points to persisting dynamics even at low temperatures.

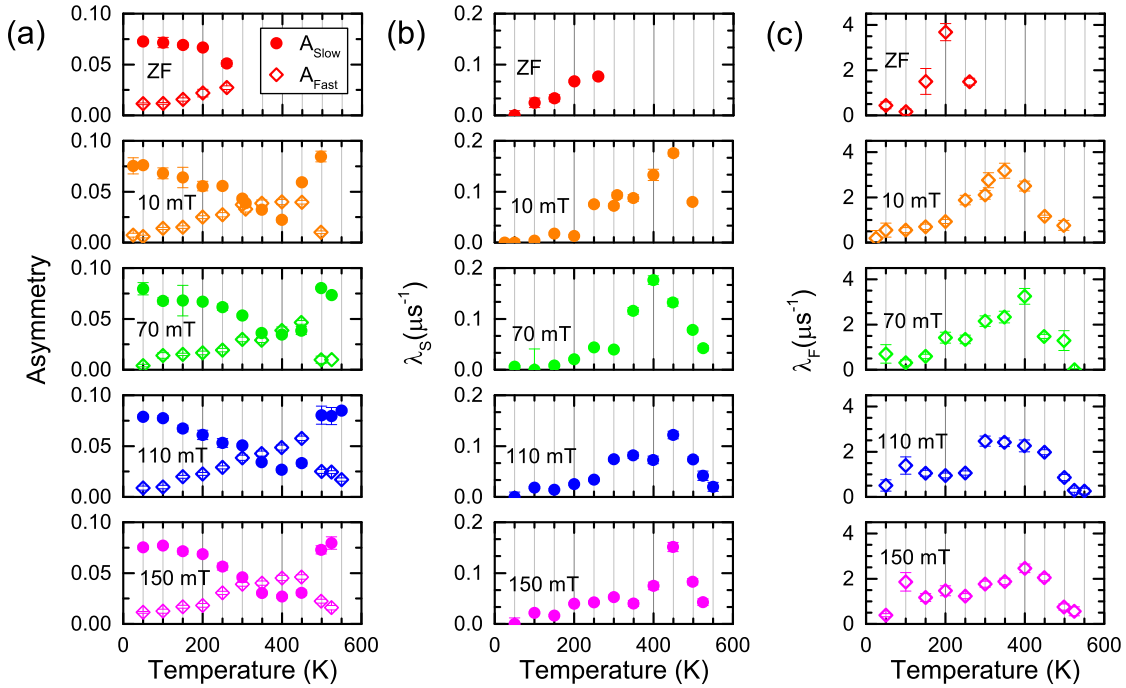

Figure 5.16: The fit parameters from ZF and LF measurements as a function of temperature. **(a)** The asymmetry of the slow (A_{slow}) and fast (A_{fast}) components, **(b)** the slow (λ_{S}) and **(c)** fast (λ_{F}) relaxation rate.

Key Results:
The magnetic phase diagram of the $Pt/Co_{40}Fe_{40}B_{20}/Ru$ multilayered superstructure was studied in the temperature range of $50<T<550$ K and applied magnetic field $0<H<250$ mT. Below the field-polarized state, a magnetic-skyrmion phase is identified, also present at room temperature, followed by phases of elongated magnetic domains. The system is characterized by high dynamics in the whole temperature range, with a weak dependence on the externally applied field.

Chapter 6

Conclusions and Outlooks

This thesis is set out to study solid materials of various form, composition and characteristic properties by positive muon spin rotation, relaxation and resonance (μ^+SR). The main focus lies on magnetic materials, however also non-magnetic materials were studied (see Paper III and articles not included in the thesis), showcasing the range of application of μ^+SR. During this time our experimental team has operated μ^+SR instruments in large scale facilities around the world and took advantage of various modules of the technique. Depending on the material system, additional experimental methods were utilized for the study of structure and magnetism in different space and time scales. Our purpose was to link the observed macroscopic properties to the microscopic interactions and mechanisms that drive them. This task is defined by the geometry, composition and correlations between elementary degrees of freedom in the material.

For the samples exhibiting electronic magnetism, our research focused on the investigation of the magnetic phases by the purely magnetic muon probe with a unique timescale and the ability to measure in true zero field. The magnetism in the complex 3D perovskite structures comes typically in multiple phases due to the interwined magnetic elements. Therefore, a microscopic investigation may contribute to our understanding of how magnetic ordering is formed. In the double perovskite $LaSr_{1-x}Ca_xNiReO_6$ (x=0,1) magnetic phases appear as high as T$\simeq$250 K, confirmed also by magnetic susceptibility measurements. The fracture of correlated magnetic moments in a dilute state develops into a magnetically ordered state at lower temperatures, dependent on the substitution of Ca with Sr cations. This exchange affects the superexchange interaction between Ni and Re magnetic sublattices, leading to a lower state either commensurate or incommensurate to the periodicity of a crystal lattice.

We move towards two dimensional systems where innate or induced anisotropies play a definitive role in the magnetic ordering. The intrinsic 2D Van der Waals compound $CrCl_3$ with a layered Cr structure has been previously considered to achieve a quasi-2D ferromagnetically ordered state. However, according to our findings with μ^+SR, if such an ordering exists it should appear only in short range. The lower state is confirmed to be antiferromagnetic, but with a possibility of 3D canting of spins, which decreases at higher temperatures. Nevertheless, the subject of the magnetic phases of $CrCl_3$ should be revisited and studied in close correlation to variations in the crystal structure.

Another way to achieve two dimensional systems is to directly fabricate thin films with selected materials. We investigated the magnetism in multilayer $Pt/Co_{40}Fe_{40}B_{20}/Ru$ superlattices expected to host intefacial chiral magnetic structures. Magnetic force microscopy and magnetotransport measurements confirm a transition to a skyrmion phase followed by a phase of elongated magnetic domains as a function of temperature and field. The μ^+SR measurements performed at a selected depth in the superstructure evidenced

persisting dynamics below transition temperature and in the range of applied fields, due to collective excitations. It is noted that signatures of dynamic processes in the muon 10^{-5}-10^{-12} time scale have been observed in all the above systems, even at the lowest studied temperature. Variations in the internal field distribution also hint towards the appearance of an additional phase of elongated ordered domains at low temperatures. However, further research is needed to support this premise. Concerning μ^+SR, a complete treatment requires measurements in TF geometry in a broader temperature range and a depth profiling of the magnetic structure.

Nuclear magnetism allows muons to also probe ion kinetics in the crystal structure. μ^+SR was therefore employed once more to study single crystals of hybrid organic-inorganic perovskites $MAPbX_3$ (X=Br,Cl). These feverishly researched, next-generation photovoltaic materials are characterized by long carrier lifetimes but a fragile structural stability. Our μ^+SR findings, over a wide temperature range and in a dark or illuminated environment, support the premise that the source of both effects are the fluctuations of the molecular cation. The results on temperature evolution of the static and dynamic field components were complimented with numerical simulations and supported by X-ray diffraction and calorimetry measurements on the structural phases. The combined results show that structural transitions are driven by the molecular fluctuations, which can be moderated by the choice of halogen anion. In the illuminated case, these fluctuations appear enhanced, indicating the interaction between photogenerated carriers and MA cations. This conclusion can be supported by measuring the photoluminescence lifetimes in these crystals. A more advanced μ^+SR study would require measurements under illumination with selected wavelengths and varied exposition time. Finally, more detailed measurements at high temperatures and in various crystallographic directions would supply us with information on the other diffusing ions.

When studying materials in the scale of atoms, the four dimensions alone can already create a hard enough puzzle to solve. Interaction between different species and degrees of freedom results in a complexity which only a local spy may untangle. However, it is our interaction with matter that creates new materials, with useful properties and exciting physics. The human degree of freedom.

Bibliography

[1] N. Martin, "Towards a better understanding of ancient and modern cement and concrete," The Classical Outlook, vol. 90, no. 4, pp. 130–133, 2015.

[2] F. Müller-Römer, "A new consideration of the construction methods of the ancient egyptian pyramids," Journal of the American Research Center in Egypt, vol. 44, pp. 113–140, 2008.

[3] T. F. Potts, "Patterns of trade in third-millennium bc mesopotamia and iran," World Archaeology, vol. 24, no. 3, pp. 379–402, 1993.

[4] W. Ling, "On the invention and use of gunpowder and firearms in china," Isis, vol. 37, no. 3/4, pp. 160–178, 1947.

[5] F. Seitz, "The tangled prelude to the age of silicon electronics," Proceedings of the American Philosophical Society, vol. 140, no. 3, pp. 289–337, 1996.

[6] R. Sennett, The Craftsman. New Haven, CT: Yale University Press, Mar. 2009.

[7] F. Seitz, The modern theory of solids. Mineola, NY: Dover Publications, Dec. 1987.

[8] G. S. Girolami, X-Ray Crystallography. Sausalito, CA: University Science Books, 1 ed., July 2015.

[9] F. Bloch, "Uber die quantenmechanik der elektronen in kristallgittern," Zeitschrift fur Physik, vol. 52, p. 555–600, July 1929.

[10] V. Fock, "Naherungsmethode zur osung des quantenmechanischen mehrkorperproblems," Zeitschrift fur Physik, vol. 61, p. 126–148, Jan. 1930.

[11] P. Fulde, Correlated electrons in quantum matter. World Scientific, 2012.

[12] M. Imada, A. Fujimori, and Y. Tokura, "Metal-insulator transitions," Reviews of Modern Physics, vol. 70, p. 1039–1263, Oct. 1998.

[13] Y. Maeno, H. Hashimoto, K. Yoshida, S. Nishizaki, T. Fujita, J. G. Bednorz, and F. Lichtenberg, "Superconductivity in a layered perovskite without copper," Nature, vol. 372, p. 532–534, Dec. 1994.

[14] A. K. Geim and K. S. Novoselov, "The rise of graphene," Nature Materials, vol. 6, p. 183–191, Mar. 2007.

[15] A. Vasiliev, O. Volkova, E. Zvereva, and M. Markina, "Milestones of low-d quantum magnetism," npj Quantum Materials, vol. 3, Mar. 2018.

[16] Z. Li, M. Ma, Z. Chen, K. Xie, and F. Ma, "Interaction between magnon and skyrmion: Toward quantum magnonics," Journal of Applied Physics, vol. 132, Dec. 2022.

[17] L. Bevaart, E. Frikkee, and L. J. de Jongh, "Neutron-scattering study of magnetic-field-induced transitions in a two-component antiferromagnetic system with competing spin anisotropies," Physical Review B, vol. 19, p. 4741–4756, May 1979.

[18] A. Yaouanc and P. D. de Reotier, Muon spin rotation, relaxation, and resonance. International Series of Monographs on Physics, London, England: Oxford University Press, Dec. 2010.

[19] N. Bohr, "Atomic structure," Nature, vol. 107, pp. 104–107, mar 1921.

[20] A. R. Pietro Carretta, Structure of Matter. Springer International Publishing, June 2015.

[21] J. C. Slater, Quantum theory of atomic structure: V. 1. Pure & Applied Physics S., New York, NY: McGraw-Hill, Dec. 1960.

[22] G. K. Woodgate, Elementary Atomic Structure. OUP Oxford, Aug. 1983.

[23] A. Kastberg, Structure of Multielectron Atoms. Springer-Verlag GmbH, Apr. 2020.

[24] H. A. Bethe, "Splitting of terms in crystals," in World Scientific Series in 20th Century Physics, pp. 1–72, WORLD SCIENTIFIC, jul 1997.

[25] J. H. Van Vleck, "Quantum mechanics-the key to understanding magnetism," Reviews of Modern Physics, vol. 50, p. 181–189, Apr. 1978.

[26] U. o. O. B. Stephen (Department of Physics, Magnetism in Condensed Matter. Oxford University Press, Oct. 2001.

[27] D. Griffiths, Introduction to elementary particles. Weinheim, Germany: Wiley-VCH Verlag, 2 ed., Aug. 2008.

[28] W. Heisenberg, "Zur theorie des ferromagnetismus," in Original Scientific Papers Wissenschaftliche Originalarbeiten, pp. 580–597, Springer Berlin Heidelberg, 1985.

[29] M. E. Fisher, "Magnetism in one-dimensional systems—the heisenberg model for infinite spin," American Journal of Physics, vol. 32, pp. 343–346, may 1964.

[30] P. W. Anderson, "New approach to the theory of superexchange interactions," Physical Review, vol. 115, pp. 2–13, jul 1959.

[31] J. Goodenough, Magnetism and the chemical bond. Huntington, N.Y: R.E. Krieger Pub. Co, 1976.

[32] K. M. Krishnan, Magnetism in Metals and Alloys. Oxford University Press, Aug. 2016.

[33] L. Šamaj and Z. Bajnok, Introduction to the Statistical Physics of Integrable Many-body Systems. Cambridge University Press, May 2013.

[34] I. Dzyaloshinsky, "A thermodynamic theory of "weak" ferromagnetism of antiferromagnetics," Journal of Physics and Chemistry of Solids, vol. 4, p. 241–255, Jan. 1958.

[35] T. Moriya, "Anisotropic superexchange interaction and weak ferromagnetism," Physical Review, vol. 120, p. 91–98, Oct. 1960.

[36] P. G. Evans and E. D. Isaacs, "Magnetic x-ray microdiffraction," Journal of Physics D: Applied Physics, vol. 39, pp. R245–R263, jul 2006.

[37] C. V. Topping and S. J. Blundell, "A.c. susceptibility as a probe of low-frequency magnetic dynamics," Journal of Physics: Condensed Matter, vol. 31, p. 013001, Nov. 2018.

[38] P. Weiss, "L'hypothèse du champ moléculaire et la propriété ferromagnétique," Journal de Physique Théorique et Appliquée, vol. 6, no. 1, pp. 661–690, 1907.

[39] A. J. Larkoski, Elementary Particle Physics: An Intuitive Introduction. Cambridge University Press, May 2019.

[40] V. Hess, "Unsolved problems in physics: Tasks for the immediate future in cosmic ray studies." https://www.nobelprize.org/prizes/physics/1936/hess/lecture/, Dec. 1936.

[41] "High energy cosmic rays striking atoms at the top of the atmosphere give the rise to showers of particles striking the Earth's surface. Des rayons cosmiques de haute energie heurtent des atomes dans la haute atmosphere et donnent ainsi naissance a des gerbes de particules projetees sur la surface terrestre." https://cds.cern.ch/record/40407. Accessed: 2024-1-13.

[42] "Psi smus beamlines." https://www.psi.ch/en/smus/beamlines. Accessed: 2024-1-13.

[43] P. K. F. Grieder, Cosmic rays at earth. Elsevier Science & Technology, July 2001.

[44] S. Swordy, "The energy spectra and anisotropies of cosmic rays," Space Science Reviews, vol. 99, no. 1/4, p. 85–94, 2001.

[45] F. Fenu, "The cosmic ray energy spectrum measured with the pierre auger observatory," Advances in Space Research, vol. 72, p. 3531–3537, Oct. 2023.

[46] S. H. Neddermeyer and C. D. Anderson, "Nature of cosmic-ray particles," Reviews of Modern Physics, vol. 11, p. 191–207, July 1939.

[47] B. Rossi and D. B. Hall, "Variation of the rate of decay of mesotrons with momentum," Physical Review, vol. 59, p. 223–228, Feb. 1941.

[48] G. Bonomi, P. Checchia, M. D'Errico, D. Pagano, and G. Saracino, "Applications of cosmic-ray muons," Progress in Particle and Nuclear Physics, vol. 112, p. 103768, May 2020.

[49] F. Jegerlehner and A. Nyffeler, "The muon g-2," Physics Reports, vol. 477, p. 1–110, June 2009.

[50] A. Keshavarzi, "The muon g-2 experiment at fermilab," EPJ Web of Conferences, vol. 212, p. 05003, 2019.

[51] T. Han, Z. Liu, L.-T. Wang, and X. Wang, "Wimps at high energy muon colliders," Physical Review D, vol. 103, Apr. 2021.

[52] T. D. Lee and C. N. Yang, "Question of parity conservation in weak interactions," Physical Review, vol. 104, p. 254–258, Oct. 1956.

[53] R. L. Garwin, L. M. Lederman, and M. Weinrich, "Observations of the failure of conservation of parity and charge conjugation in meson decays: the magnetic moment of the free muon," Physical Review, vol. 105, pp. 1415–1417, feb 1957.

[54] J. I. Friedman and V. L. Telegdi, "Nuclear emulsion evidence for parity nonconservation in the decay chain pi>mu>e," Physical Review, vol. 106, p. 1290–1293, June 1957.

[55] "Muon centres." https://muonsources.org/muon-centres/. Accessed: 2024-1-13.

[56] S. J. Blundell, R. De Renzi, T. Lancaster, and F. L. Pratt, eds., Muon spectroscopy. London, England: Oxford University Press, Nov. 2021.

[57] M. Tanabashi, K. Hagiwara, K. Hikasa, K. Nakamura, Y. Sumino, F. Takahashi, J. Tanaka, K. Agashe, G. Aielli, C. Amsler, M. Antonelli, D. Asner, H. Baer, S. Banerjee, R. Barnett, T. Basaglia, C. Bauer, J. Beatty, V. Belousov, J. Beringer, S. Bethke, A. Bettini, H. Bichsel, O. Biebel, K. Black, E. Blucher, O. Buchmuller, V. Burkert, M. Bychkov, R. Cahn, M. Carena, A. Ceccucci, A. Cerri, D. Chakraborty, M.-C. Chen, R. Chivukula, G. Cowan, O. Dahl, G. D'Ambrosio, T. Damour, D. de Florian, A. de Gouvêa, T. DeGrand, P. de Jong, G. Dissertori, B. Dobrescu, M. D'Onofrio, M. Doser, M. Drees, H. Dreiner, D. Dwyer, P. Eerola, S. Eidelman, J. Ellis, J. Erler, V. Ezhela, W. Fetscher, B. Fields, R. Firestone, B. Foster, A. Freitas, H. Gallagher, L. Garren, H.-J. Gerber, G. Gerbier, T. Gershon, Y. Gershtein, T. Gherghetta, A. Godizov, M. Goodman, C. Grab, A. Gritsan, C. Grojean, D. Groom, M. Grünewald, A. Gurtu, T. Gutsche, H. Haber, C. Hanhart, S. Hashimoto, Y. Hayato, K. Hayes, A. Hebecker, S. Heinemeyer, B. Heltsley, J. Hernández-Rey, J. Hisano, A. Höcker, J. Holder, A. Holtkamp, T. Hyodo, K. Irwin, K. Johnson, M. Kado, M. Karliner, U. Katz, S. Klein, E. Klempt, R. Kowalewski, F. Krauss, M. Kreps, B. Krusche, Y. Kuyanov, Y. Kwon, O. Lahav, J. Laiho, J. Lesgourgues, A. Liddle, Z. Ligeti, C.-J. Lin, C. Lippmann, T. Liss, L. Littenberg, K. Lugovsky, S. Lugovsky, A. Lusiani, Y. Makida, F. Maltoni, T. Mannel, A. Manohar, W. Marciano, A. Martin, A. Masoni, J. Matthews, U.-G. Meißner, D. Milstead, R. Mitchell, K. Mönig, P. Molaro, F. Moortgat, M. Moskovic, H. Murayama, M. Narain, P. Nason, S. Navas, M. Neubert, P. Nevski, Y. Nir, K. Olive, S. Pagan Griso, J. Parsons, C. Patrignani, J. Peacock, M. Pennington, S. Petcov, V. Petrov, E. Pianori, A. Piepke, A. Pomarol, A. Quadt, J. Rademacker, G. Raffelt, B. Ratcliff, P. Richardson, A. Ringwald, S. Roesler, S. Rolli, A. Romaniouk, L. Rosenberg, J. Rosner, G. Rybka, R. Ryutin, C. Sachrajda, Y. Sakai, G. Salam, S. Sarkar, F. Sauli, O. Schneider, K. Scholberg, A. Schwartz, D. Scott, V. Sharma, S. Sharpe, T. Shutt, M. Silari, T. Sjöstrand, P. Skands, T. Skwarnicki, J. Smith, G. Smoot, S. Spanier, H. Spieler, C. Spiering, A. Stahl, S. Stone, T. Sumiyoshi, M. Syphers, K. Terashi, J. Terning, U. Thoma, R. Thorne, L. Tiator, M. Titov,

N. Tkachenko, N. Törnqvist, D. Tovey, G. Valencia, R. Van de Water, N. Varelas, G. Venanzoni, L. Verde, M. Vincter, P. Vogel, A. Vogt, S. Wakely, W. Walkowiak, C. Walter, D. Wands, D. Ward, M. Wascko, G. Weiglein, D. Weinberg, E. Weinberg, M. White, L. Wiencke, S. Willocq, C. Wohl, J. Womersley, C. Woody, R. Workman, W.-M. Yao, G. Zeller, O. Zenin, R.-Y. Zhu, S.-L. Zhu, F. Zimmermann, P. Zyla, J. Anderson, L. Fuller, V. Lugovsky, and P. Schaffner, "Review of particle physics," Physical Review D, vol. 98, Aug. 2018.

[58] S. Estreicher and P. F. Meier, "Energy profiles for light impurities in simple metals," Physical Review B, vol. 27, p. 642–658, Jan. 1983.

[59] L. Michel, "Interaction between four half-spin particles and the decay of the -meson," Proceedings of the Physical Society. Section A, vol. 63, p. 514–531, May 1950.

[60] I. A. Campbell, A. Amato, F. N. Gygax, D. Herlach, A. Schenck, R. Cywinski, and S. H. Kilcoyne, "Dynamics in canonical spin glasses observed by muon spin depolarization," Physical Review Letters, vol. 72, pp. 1291–1294, feb 1994.

[61] B. Rainford, R. Cywinski, and S. Dakin, "Neutron and musr studies of spin fluctuations in ymn2 and related alloys," Journal of Magnetism and Magnetic Materials, vol. 140-144, pp. 805–806, feb 1995.

[62] X. Wan, W. J. Kossler, C. E. Stronach, and D. R. Noakes, "Cauchy magnetic field component and magnitude distribution studied by the zero-field muon spin relaxation technique," Hyperfine Interactions, vol. 122, no. 3/4, p. 233–237, 1999.

[63] R. S. Hayano, Y. J. Uemura, J. Imazato, N. Nishida, T. Yamazaki, and R. Kubo, "Zero-and low-field spin relaxation studied by positive muons," Physical Review B, vol. 20, p. 850–859, Aug. 1979.

[64] K. W. Kehr, G. Honig, and D. Richter, "Stochastic theory of spin depolarization of muons diffusing in the presence of traps," Zeitschrift fur Physik B Condensed Matter and Quanta, vol. 32, p. 49–58, Mar. 1978.

[65] A. Abragam, The principles of nuclear magnetism. International Series of Monographs on Physics, Oxford, England: Clarendon Press, Oct. 1983.

[66] A. Hillier, P. King, S. Cottrell, and J. Lord, "The musr user guide," ISIS Facility, STFC, Rutherford Appleton Laboratory, UK, 2005.

[67] S. Kilcoyne, S. Brown, S. Cottrell, S. Johnston, and C. Scott, "Musr user guide," Unknown, 1994.

[68] "ISIS EMU Muon spectrometer." https://www.isis.stfc.ac.uk/Pages/Emu.aspx.

[69] "ISIS HiFi Muon spectrometer." https://www.isis.stfc.ac.uk/Pages/HIFI.aspx.

[70] Y. Krockenberger, K. Mogare, M. Reehuis, M. Tovar, M. Jansen, G. Vaitheeswaran, V. Kanchana, F. Bultmark, A. Delin, F. Wilhelm, A. Rogalev, A. Winkler, and L. Alff, "Sr2croso6: End point of a spin-polarized metal-insulator transition by 5d band filling," Physical Review B, vol. 75, Jan. 2007.

[71] A. J. Hauser, J. R. Soliz, M. Dixit, R. E. A. Williams, M. A. Susner, B. Peters, L. M. Mier, T. L. Gustafson, M. D. Sumption, H. L. Fraser, P. M. Woodward, and F. Y. Yang, "Fully ordered sr2crreo6 epitaxial films: A high-temperature ferrimagnetic semiconductor," Physical Review B, vol. 85, Apr. 2012.

[72] S. K. Panda, Y. O. Kvashnin, B. Sanyal, I. Dasgupta, and O. Eriksson, "Electronic structure and exchange interactions of insulating double perovskite la2curuo6," Physical Review B, vol. 94, Aug. 2016.

[73] J. G. Bednorz and K. A. Muller, "Possible hight c superconductivity in the ba?la?cu?o system," Zeitschrift fur Physik B Condensed Matter, vol. 64, p. 189–193, June 1986.

[74] S. Jin, T. H. Tiefel, M. McCormack, R. A. Fastnacht, R. Ramesh, and L. H. Chen, "Thousandfold change in resistivity in magnetoresistive la-ca-mn-o films," Science, vol. 264, p. 413–415, Apr. 1994.

[75] M. Azuma, K. Takata, T. Saito, S. Ishiwata, Y. Shimakawa, and M. Takano, "Designed ferromagnetic, ferroelectric bi2nimno6," Journal of the American Chemical Society, vol. 127, p. 8889–8892, May 2005.

[76] A. Bhattacharya and S. J. May, "Magnetic oxide heterostructures," Annual Review of Materials Research, vol. 44, p. 65–90, July 2014.

[77] A. M. Glazer, "The classification of tilted octahedra in perovskites," Acta Crystallographica Section B Structural Crystallography and Crystal Chemistry, vol. 28, p. 3384–3392, Nov. 1972.

[78] A. M. Glazer, "Simple ways of determining perovskite structures," Acta Crystallographica Section A, vol. 31, p. 756–762, Nov. 1975.

[79] O. El Rhazouani, A. Slassi, Y. Ziat, and A. Benyoussef, "Competing exchange couplings in sr2crreo6 double perovskite," Physics Letters A, vol. 381, p. 1177–1180, Apr. 2017.

[80] X. Ou, F. Fan, X. Chen, T. Li, L. Jiang, A. Stroppa, X. Ouyang, and H. Wu, "Magnetic frustration in double perovskite lasrniruo6," EPL (Europhysics Letters), vol. 123, p. 57003, Oct. 2018.

[81] D. Serrate, J. M. D. Teresa, and M. R. Ibarra, "Double perovskites with ferromagnetism above room temperature," Journal of Physics: Condensed Matter, vol. 19, p. 023201, Dec. 2006.

[82] J. M. De Teresa, D. Serrate, C. Ritter, J. Blasco, M. R. Ibarra, L. Morellon, and W. Tokarz, "Investigation of the high curie temperature in sr2crreo6," Physical Review B, vol. 71, Mar. 2005.

[83] J. M. De Teresa, J. M. Michalik, J. Blasco, P. A. Algarabel, M. R. Ibarra, C. Kapusta, and U. Zeitler, "Magnetization of re-based double perovskites: Noninteger saturation magnetization disclosed," Applied Physics Letters, vol. 90, June 2007.

[84] A. T. Lee and C. A. Marianetti, "Structural and metal-insulator transitions in rhenium-based double perovskites via orbital ordering," Physical Review B, vol. 97, Jan. 2018.

[85] C. Sohn, E. Skoropata, Y. Choi, X. Gao, A. Rastogi, A. Huon, M. A. McGuire, L. Nuckols, Y. Zhang, J. W. Freeland, D. Haskel, and H. N. Lee, "Room-temperature ferromagnetic insulating state in cation-ordered double-perovskite $sr2fe1 + xre1 - xo6$ films," Advanced Materials, vol. 31, Nov. 2018.

[86] C. Claus J. Prakt Chem. 34 443 ; Annalen, 1846, 59, 234, 1845.

[87] B. Morosin and A. Narath, "X-ray diffraction and nuclear quadrupole resonance studies of chromium trichloride," The Journal of Chemical Physics, vol. 40, p. 1958–1967, Apr. 1964.

[88] I. Tsubokawa, "On the magnetic properties of a crbr3 single crystal," Journal of the Physical Society of Japan, vol. 15, p. 1664–1668, Sept. 1960.

[89] L. L. Handy and N. W. Gregory, "Structural properties of chromium(iii) iodide and some chromium(iii) mixed halides," Journal of the American Chemical Society, vol. 74, p. 891–893, Feb. 1952.

[90] C. Gong, L. Li, Z. Li, H. Ji, A. Stern, Y. Xia, T. Cao, W. Bao, C. Wang, Y. Wang, Z. Q. Qiu, R. J. Cava, S. G. Louie, J. Xia, and X. Zhang, "Discovery of intrinsic ferromagnetism in two-dimensional van der waals crystals," Nature, vol. 546, p. 265–269, Apr. 2017.

[91] K. S. Burch, D. Mandrus, and J.-G. Park, "Magnetism in two-dimensional van der waals materials," Nature, vol. 563, p. 47–52, Oct. 2018.

[92] J.-G. Park, "Opportunities and challenges of 2d magnetic van der waals materials: magnetic graphene?," Journal of Physics: Condensed Matter, vol. 28, p. 301001, June 2016.

[93] S. Sarkar and P. Kratzer, "Magnetic exchange interactions in bilayer crx3 (x=cl,br, and i): A critical assesement of dft+u approach," Physical Review B, vol. 103, June 2021.

[94] H. Zhu, Y. Gao, Y. Hou, Z. Gui, and L. Huang, "Tunable magnetic anisotropy in two-dimensional crx3/ain (x=i,br,cl) heterostructures," Physical Review B, vol. 106, Oct. 2022.

[95] L. Webster and J.-A. Yan, "Strain-tunable magnetic anisotropy in monolayer crcl3, crbr3 and cri3," Physical Review B, vol. 98, Oct. 2018.

[96] H. Wang, V. Eyert, and U. Schwingenschlögl, "Electronic structure and magnetic ordering of the semiconducting chromium trihalides crcl3, crbr3, and cri3," Journal of Physics: Condensed Matter, vol. 23, p. 116003, Mar. 2011.

[97] D. Ghazaryan, M. T. Greenaway, Z. Wang, V. H. Guarochico-Moreira, I. J. Vera-Marun, J. Yin, Y. Liao, S. V. Morozov, O. Kristanovski, A. I. Lichtenstein, M. I. Katsnelson, F. Withers, A. Mishchenko, L. Eaves, A. K. Geim, K. S. Novoselov, and A. Misra, "Magnon-assisted tunnelling in van der waals heterostructures based on crbr3," Nature Electronics, vol. 1, p. 344–349, June 2018.

[98] Z. Wang, M. Gibertini, D. Dumcenco, T. Taniguchi, K. Watanabe, E. Giannini, and A. F. Morpurgo, "Determining the phase diagram of atomically thin layered antiferromagnet crcl3," Nature Nanotechnology, vol. 14, p. 1116–1122, Nov. 2019.

[99] D. R. Klein, D. MacNeill, J. L. Lado, D. Soriano, E. Navarro-Moratalla, K. Watanabe, T. Taniguchi, S. Manni, P. Canfield, J. Fernández-Rossier, and P. Jarillo-Herrero, "Probing magnetism in 2d van der waals crystalline insulators via electron tunneling," Science, vol. 360, p. 1218–1222, June 2018.

[100] M. A. McGuire, H. Dixit, V. R. Cooper, and B. C. Sales, "Coupling of crystal structure and magnetism in the layered, ferromagnetic insulator cri3," Chemistry of Materials, vol. 27, p. 612–620, Jan. 2015.

[101] J. Meseguer-Sánchez, C. Popescu, J. L. García-Muñoz, H. Luetkens, G. Taniashvili, E. Navarro-Moratalla, Z. Guguchia, and E. J. G. Santos, "Coexistence of structural and magnetic phases in van der waals magnet cri3," Nature Communications, vol. 12, Nov. 2021.

[102] N. Bykovetz, A. Hoser, and C. L. Lin, "Critical region phase transitions in the quasi-2d magnet crcl3," AIP Advances, vol. 9, Mar. 2019.

[103] H. Wang, P. Lei, X. Mao, X. Kong, X. Ye, P. Wang, Y. Wang, X. Qin, J. Meijer, H. Zeng, F. Shi, and J. Du, "Magnetic phase transition in two-dimensional crbr3 probed by a quantum sensor," Chinese Physics Letters, vol. 39, p. 047601, Apr. 2022.

[104] F. Xue, Y. Hou, Z. Wang, and R. Wu, "Two-dimensional ferromagnetic van der waals crcl3 monolayer with enhanced anisotropy and curie temperature," Physical Review B, vol. 100, Dec. 2019.

[105] X. Lu, R. Fei, L. Zhu, and L. Yang, "Meron-like topological spin defects in monolayer crcl3," Nature Communications, vol. 11, Sept. 2020.

[106] L. Chen, J.-H. Chung, B. Gao, T. Chen, M. B. Stone, A. I. Kolesnikov, Q. Huang, and P. Dai, "Topological spin excitations in honeycomb ferromagnet cri3," Physical Review X, vol. 8, Nov. 2018.

[107] I. V. Solovyev, "Linear response based theories for dzyaloshinskii-moriya interactions," Physical Review B, vol. 107, Feb. 2023.

[108] M. Augustin, S. Jenkins, R. F. L. Evans, K. S. Novoselov, and E. J. G. Santos, "Properties and dynamics of meron topological spin textures in the two-dimensional magnet crcl3," Nature Communications, vol. 12, Jan. 2021.

[109] N. Sivadas, S. Okamoto, X. Xu, C. J. Fennie, and D. Xiao, "Stacking-dependent magnetism in bilayer cri3," Nano Letters, vol. 18, p. 7658–7664, Nov. 2018.

[110] D. Soriano, C. Cardoso, and J. Fernández-Rossier, "Interplay between interlayer exchange and stacking in cri3 bilayers," Solid State Communications, vol. 299, p. 113662, Sept. 2019.

[111] S. Jana, P. Aich, P. A. Kumar, O. K. Forslund, E. Nocerino, V. Pomjakushin, M. Månsson, Y. Sassa, P. Svedlindh, O. Karis, V. Siruguri, and S. Ray, "Revisiting goodenough-kanamori rules in a new series of double perovskites LaSr1-xCaxNiReO6," Scientific Reports, vol. 9, dec 2019.

[112] C. M. Thompson, L. Chi, J. R. Hayes, A. M. Hallas, M. N. Wilson, T. J. S. Munsie, I. P. Swainson, A. P. Grosvenor, G. M. Luke, and J. E. Greedan, "Synthesis, structure, and magnetic properties of novel b-site ordered double perovskites, srlamreo6 (m = mg, mn, co and ni)," Dalton Transactions, vol. 44, no. 23, p. 10806–10816, 2015.

[113] O. K. Forslund, K. Papadopoulos, E. Nocerino, G. Morris, B. Hitti, D. Arseneau, V. Pomjakushin, N. Matsubara, J.-C. Orain, P. Svedlindh, et al., "Intertwined magnetic sublattices in the double perovskite compound lasrnireo6," Physical Review B, vol. 102, no. 14, p. 144409, 2020.

[114] K. Papadopoulos, O. K. Forslund, E. Nocerino, F. O. L. Johansson, G. Simutis, N. Matsubara, G. Morris, B. Hitti, D. Arseneau, P. Svedlindh, M. Medarde, D. Andreica, J.-C. Orain, V. Pomjakushin, L. Börjesson, J. Sugiyama, M. Månsson, and Y. Sassa, "Influence of the magnetic sub-lattices in the double perovskite compound lacanireo6," Physical Review B, vol. 106, Dec. 2022.

[115] J. De Teresa, D. Serrate, J. Blasco, M. Ibarra, and L. Morellon, "Impact of cation size on magnetic properties of aa'2fereo6 double perovskites," Physical Review B, vol. 69, no. 14, p. 144401, 2004.

[116] N. Auth, G. Jakob, W. Westerburg, C. Ritter, I. Bonn, C. Felser, and W. Tremel, "Crystal structure and magnetism of the double perovskites a2fereo6 (a=ca, sr, ba)," Journal of Magnetism and Magnetic Materials, vol. 272-276, pp. E607–E608, may 2004.

[117] G. Popov, M. Greenblatt, and M. Croft, "Large effects of a-site average cation size on the properties of the double perovskites ba 2- x sr x mnreo 6: A d 5- d 1 system," Physical Review B, vol. 67, no. 2, p. 024406, 2003.

[118] P.-L. Ho, C.-P. Yu, Q. Zhang, K. Song, J. P. Buban, S.-Y. Choi, R. E. Dunin-Borkowski, J. Mayer, N.-H. Tai, J. Zhu, L. Jin, and X. Zhong, "Effect of cation ratio and order on magnetic circular dichroism in the double perovskite sr2fe1+xre1-xo6," Ultramicroscopy, vol. 193, pp. 137–142, oct 2018.

[119] J. B. Goodenough, "Theory of the role of covalence in the perovskite-type manganites [la,m(ii)]mno3," Physical Review, vol. 100, p. 564–573, Oct. 1955.

[120] J. Kanamori, "Superexchange interaction and symmetry properties of electron orbitals," Journal of Physics and Chemistry of Solids, vol. 10, p. 87–98, July 1959.

[121] R. Morrow, R. Mishra, O. D. Restrepo, M. R. Ball, W. Windl, S. Wurmehl, U. Stockert, B. Büchner, and P. M. Woodward, "Independent ordering of two interpenetrating magnetic sublattices in the double perovskite sr2cooso6," Journal of the American Chemical Society, vol. 135, p. 18824–18830, Dec. 2013.

[122] R. Morrow, J. W. Freeland, and P. M. Woodward, "Probing the links between structure and magnetism in sr2–xcaxfeoso6 double perovskites," Inorganic Chemistry, vol. 53, p. 7983–7992, July 2014.

[123] C. R. Wiebe, J. E. Greedan, G. M. Luke, and J. S. Gardner, "Spin-glass behavior in the s=1/2 fcc ordered perovskite sr2careo6," Physical Review B, vol. 65, Mar. 2002.

[124] H. Kato, T. Okuda, Y. Okimoto, Y. Tomioka, K. Oikawa, T. Kamiyama, and Y. Tokura, "Structural and electronic properties of the ordered double perovskites a2mreo6 (a=sr,ca; m=mg,sc,cr,mn,fe,co,ni,zn)," Physical Review B, vol. 69, May 2004.

[125] K. Lejaeghere, G. Bihlmayer, T. Björkman, P. Blaha, S. Blügel, V. Blum, D. Caliste, I. E. Castelli, S. J. Clark, A. Dal Corso, S. de Gironcoli, T. Deutsch, J. K. Dewhurst, I. Di Marco, C. Draxl, M. Dułak, O. Eriksson, J. A. Flores-Livas, K. F. Garrity, L. Genovese, P. Giannozzi, M. Giantomassi, S. Goedecker, X. Gonze, O. Grånäs, E. K. U. Gross, A. Gulans, F. Gygi, D. R. Hamann, P. J. Hasnip, N. A. W. Holzwarth, D. Iuşan, D. B. Jochym, F. Jollet, D. Jones, G. Kresse, K. Koepernik, E. Küçükbenli, Y. O. Kvashnin, I. L. M. Locht, S. Lubeck, M. Marsman, N. Marzari, U. Nitzsche, L. Nordström, T. Ozaki, L. Paulatto, C. J. Pickard, W. Poelmans, M. I. J. Probert, K. Refson, M. Richter, G.-M. Rignanese, S. Saha, M. Scheffler, M. Schlipf, K. Schwarz, S. Sharma, F. Tavazza, P. Thunström, A. Tkatchenko, M. Torrent, D. Vanderbilt, M. J. van Setten, V. Van Speybroeck, J. M. Wills, J. R. Yates, G.-X. Zhang, and S. Cottenier, "Reproducibility in density functional theory calculations of solids," Science, vol. 351, Mar. 2016.

[126] G. Prandini, A. Marrazzo, I. E. Castelli, N. Mounet, and N. Marzari, "Precision and efficiency in solid-state pseudopotential calculations," npj Computational Materials, vol. 4, Dec. 2018.

[127] L. Eyring, K. A. Gschneidner, and G. H. Lander, Handbook on the physics and chemistry of rare earths, vol. 32. Elsevier, 2002.

[128] A. T. Savici, Y. Fudamoto, I. M. Gat, T. Ito, M. I. Larkin, Y. J. Uemura, G. M. Luke, K. M. Kojima, Y. S. Lee, M. A. Kastner, R. J. Birgeneau, and K. Yamada, "Muon spin relaxation studies of incommensurate magnetism and superconductivity in stage-4 la2cuo4.11 and la1.88sr0.12cuo4," Physical Review B, vol. 66, July 2002.

[129] O. K. Forslund, H. Ohta, K. Kamazawa, S. L. Stubbs, O. Ofer, M. Månsson, C. Michioka, K. Yoshimura, B. Hitti, D. Arseneau, G. D. Morris, E. J. Ansaldo, J. H. Brewer, and J. Sugiyama, "Revisiting the a-type antiferromagnet nanio2 with muon spin rotation measurements and density functional theory calculations," Physical Review B, vol. 102, Nov. 2020.

[130] B. Aslibeiki, P. Kameli, and H. Salamati, "Reentrant spin glass behavior in la0.8sr0.2mn1-xtixo3 manganites," Solid State Communications, vol. 149, p. 1274–1277, Aug. 2009.

[131] P. Joy and S. Date, "On the low-temperature anomaly in the ac susceptibility of la0.9ca0.1mno3," Journal of Magnetism and Magnetic Materials, vol. 220, p. 106–114, Oct. 2000.

[132] A. Amato, H. Luetkens, K. Sedlak, A. Stoykov, R. Scheuermann, M. Elender, A. Raselli, and D. Graf, "The new versatile general purpose surface-muon instrument (gps) based on silicon photomultipliers for musr measurements on a continuous-wave beam," Review of Scientific Instruments, vol. 88, Sept. 2017.

[133] M. A. McGuire, G. Clark, S. KC, W. M. Chance, G. E. Jellison, V. R. Cooper, X. Xu, and B. C. Sales, "Magnetic behavior and spin-lattice coupling in cleavable van der waals layered crcl3 crystals," Physical Review Materials, vol. 1, June 2017.

[134] J. Cable, M. Wilkinson, and E. Wollan, "Neutron diffraction investigation of antiferromagnetism in crcl3," Journal of Physics and Chemistry of Solids, vol. 19, p. 29–34, Apr. 1961.

[135] B. Kuhlow, "Magnetic ordering in crcl3 at the phase transition," physica status solidi (a), vol. 72, p. 161–168, July 1982.

[136] O. K. Forslund, K. Papadopoulos, E. Nocerino, G. Di Berardino, C. Wang, J. Sugiyama, D. Andreica, A. N. Vasiliev, M. Abdel-Hafiez, M. Månsson, and Y. Sassa, "Spin dynamics in the van der waals magnet $crcl_3$," 2021.

[137] A. Kojima, K. Teshima, Y. Shirai, and T. Miyasaka, "Organometal halide perovskites as visible-light sensitizers for photovoltaic cells," Journal of the American Chemical Society, vol. 131, pp. 6050–6051, Apr. 2009.

[138] "Best research-cell efficiency chart." `https://www.nrel.gov/pv/cell-efficiency.html`. Accessed: 2023-11-08.

[139] T. N. Murakami and N. Koumura, "Development of next-generation organic-based solar cells: Studies on dye-sensitized and perovskite solar cells," Advanced Energy Materials, vol. 9, Nov. 2018.

[140] C. Liang, H. Gu, Y. Xia, Z. Wang, X. Liu, J. Xia, S. Zuo, Y. Hu, X. Gao, W. Hui, L. Chao, T. Niu, M. Fang, H. Lu, H. Dong, H. Yu, S. Chen, X. Ran, L. Song, B. Li, J. Zhang, Y. Peng, G. Shao, J. Wang, Y. Chen, G. Xing, and W. Huang, "Two-dimensional ruddlesden–popper layered perovskite solar cells based on phase-pure thin films," Nature Energy, vol. 6, pp. 38–45, Nov. 2020.

[141] X. Cheng, S. Yang, B. Cao, X. Tao, and Z. Chen, "Single crystal perovskite solar cells: Development and perspectives," Advanced Functional Materials, vol. 30, Nov. 2019.

[142] M. Bari, H. Wu, A. A. Bokov, R. F. Ali, H. N. Tailor, B. D. Gates, and Z.-G. Ye, "Room-temperature synthesis, growth mechanisms and opto-electronic properties of organic–inorganic halide perovskite ch3nh3pbx3 (x = i, br, and cl) single crystals," CrystEngComm, vol. 23, no. 18, pp. 3326–3339, 2021.

[143] R. Saxena, J. Kangsabanik, A. Kumar, A. Shahee, S. Singh, N. Jain, S. Ghorui, V. Kumar, A. V. Mahajan, A. Alam, et al., "Contrasting temperature dependence of the band gap in ch 3 nh 3 pb x 3 (x= i, br, cl): Insight from lattice dilation and electron-phonon coupling," Physical Review B, vol. 102, no. 8, p. 081201, 2020.

[144] E. Mosconi, P. Umari, and F. D. Angelis, "Electronic and optical properties of mapbx 3 perovskites (x= i, br, cl): a unified dft and gw theoretical analysis," Physical Chemistry Chemical Physics, vol. 18, no. 39, pp. 27158–27164, 2016.

[145] L. M. Herz, "Charge-carrier mobilities in metal halide perovskites: Fundamental mechanisms and limits," ACS Energy Letters, vol. 2, pp. 1539–1548, June 2017.

[146] S. D. Stranks, G. E. Eperon, G. Grancini, C. Menelaou, M. J. P. Alcocer, T. Leijtens, L. M. Herz, A. Petrozza, and H. J. Snaith, "Electron-hole diffusion lengths exceeding 1 micrometer in an organometal trihalide perovskite absorber," Science, vol. 342, pp. 341–344, Oct. 2013.

[147] Q. Dong, Y. Fang, Y. Shao, P. Mulligan, J. Qiu, L. Cao, and J. Huang, "Electron-hole diffusion lengths > 175 μm in solution grown ch3nh3pbi3 single crystals," Science, vol. 347, pp. 967–970, Feb. 2015.

[148] M. I. Saidaminov, A. L. Abdelhady, B. Murali, E. Alarousu, V. M. Burlakov, W. Peng, I. Dursun, L. Wang, Y. He, G. Maculan, A. Goriely, T. Wu, O. F. Mohammed, and O. M. Bakr, "High-quality bulk hybrid perovskite single crystals within minutes by inverse temperature crystallization," Nature Communications, vol. 6, jul 2015.

[149] G. Maculan, A. D. Sheikh, A. L. Abdelhady, M. I. Saidaminov, M. A. Haque, B. Murali, E. Alarousu, O. F. Mohammed, T. Wu, and O. M. Bakr, "Ch3nh3pbcl3 single crystals: Inverse temperature crystallization and visible-blind uv-photodetector," The Journal of Physical Chemistry Letters, vol. 6, pp. 3781–3786, sep 2015.

[150] C. Eames, J. M. Frost, P. R. F. Barnes, B. C. O'Regan, A. Walsh, and M. S. Islam, "Ionic transport in hybrid lead iodide perovskite solar cells," Nature Communications, vol. 6, June 2015.

[151] W.-J. Yin, T. Shi, and Y. Yan, "Unusual defect physics in CH3nh3pbi3 perovskite solar cell absorber," Applied Physics Letters, vol. 104, Feb. 2014.

[152] Y. Chen, H. T. Yi, X. Wu, R. Haroldson, Y. N. Gartstein, Y. I. Rodionov, K. S. Tikhonov, A. Zakhidov, X. Y. Zhu, and V. Podzorov, "Extended carrier lifetimes and diffusion in hybrid perovskites revealed by hall effect and photoconductivity measurements," Nature Communications, vol. 7, aug 2016.

[153] H. Zhu, K. Miyata, Y. Fu, J. Wang, P. P. Joshi, D. Niesner, K. W. Williams, S. Jin, and X.-Y. Zhu, "Screening in crystalline liquids protects energetic carriers in hybrid perovskites," Science, vol. 353, pp. 1409–1413, sep 2016.

[154] M. Bokdam, J. Lahnsteiner, and D. Sarma, "Exploring librational pathways with on-the-fly machine-learning force fields: Methylammonium molecules in mapbx3 (x= i, br, cl) perovskites," The Journal of Physical Chemistry C, vol. 125, no. 38, pp. 21077–21086, 2021.

[155] A. M. A. Leguy, J. M. Frost, A. P. McMahon, V. G. Sakai, W. Kockelmann, C. Law, X. Li, F. Foglia, A. Walsh, B. C. O'Regan, J. Nelson, J. T. Cabral, and P. R. F. Barnes, "The dynamics of methylammonium ions in hybrid organic–inorganic perovskite solar cells," Nature Communications, vol. 6, May 2015.

[156] R. Wasylishen, O. Knop, and J. Macdonald, "Cation rotation in methylammonium lead halides," Solid State Communications, vol. 56, pp. 581–582, Nov. 1985.

[157] A. Poglitsch and D. Weber, "Dynamic disorder in methylammoniumtrihalogenoplumbates (II) observed by millimeter-wave spectroscopy," The Journal of Chemical Physics, vol. 87, pp. 6373–6378, Dec. 1987.

[158] K.-H. Wang, L.-C. Li, M. Shellaiah, and K. W. Sun, "Structural and photophysical properties of methylammonium lead tribromide (MAPbBr3) single crystals," Scientific Reports, vol. 7, oct 2017.

[159] H.-P. Hsu, L.-C. Li, M. Shellaiah, and K. W. Sun, "Structural, photophysical, and electronic properties of CH3nh3pbcl3 single crystals," Scientific Reports, vol. 9, Sept. 2019.

[160] D. Ghosh, P. Walsh Atkins, M. S. Islam, A. B. Walker, and C. Eames, "Good vibrations: Locking of octahedral tilting in mixed-cation iodide perovskites for solar cells," ACS Energy Letters, vol. 2, no. 10, pp. 2424–2429, 2017.

[161] A. Bonadio, C. A. Escanhoela, F. P. Sabino, G. Sombrio, V. G. de Paula, F. F. Ferreira, A. Janotti, G. M. Dalpian, and J. A. Souza, "Entropy-driven stabilization of the cubic phase of mapbi 3 at room temperature," Journal of Materials Chemistry A, vol. 9, no. 2, pp. 1089–1099, 2021.

[162] P. Lin, Q. Meng, H. Chen, H. Hu, D. Fang, L. Xu, P. Wang, and C. Cui, "Variational hysteresis and photoresponse behavior of mapbx 3 (x= i, br, cl) perovskite single crystals," Journal of Physics: Condensed Matter, vol. 33, no. 28, p. 285703, 2021.

[163] C. Lin, S. Li, W. Zhang, C. Shao, and Z. Yang, "Effect of bromine substitution on the ion migration and optical absorption in mapbi3 perovskite solar cells: The first-principles study," ACS Applied Energy Materials, vol. 1, pp. 1374–1380, Feb. 2018.

[164] L. McGovern, M. H. Futscher, L. A. Muscarella, and B. Ehrler, "Understanding the stability of mapbbr3 versus mapbi3: Suppression of methylammonium migration and reduction of halide migration," The Journal of Physical Chemistry Letters, vol. 11, pp. 7127–7132, Aug. 2020.

[165] N. Rybin, D. Ghosh, J. Tisdale, S. Shrestha, M. Yoho, D. Vo, J. Even, C. Katan, W. Nie, A. J. Neukirch, and S. Tretiak, "Effects of chlorine mixing on optoelectronics, ion migration, and gamma-ray detection in bromide perovskites," Chemistry of Materials, vol. 32, p. 1854–1863, Feb. 2020.

[166] P. Scajev, R. Aleksiejunas, S. Miasojedovas, S. Nargelas, M. Inoue, C. Qin, T. Matsushima, C. Adachi, and S. Jursenas, "Two regimes of carrier diffusion in vapor-deposited lead-halide perovskites," The Journal of Physical Chemistry C, vol. 121, p. 21600–21609, Sept. 2017.

[167] X. Wang, Y. Li, Y. Xu, Y. Pan, Y. Wu, G. Li, Q. Huang, Q. Zhang, Q. Li, X. Zhang, J. Chen, and W. Lei, "Ion migrations in lead halide perovskite single crystals with different halide components," physica status solidi (b), vol. 257, Feb. 2020.

[168] B. wook Park and S. I. Seok, "Intrinsic instability of inorganic–organic hybrid halide perovskite materials," Advanced Materials, vol. 31, Feb. 2019.

[169] K. Papadopoulos, O. K. Forslund, S. Cottrell, K. Yokoyama, P. K. Nayak, F. M. A. Noa, L. Öhrström, E. Nocerino, L. Börjesson, J. Sugiyama, M. Månsson, and Y. Sassa, "Photophysical ion dynamics in hybrid perovskite mapbx3 (x=br, cl) single crystals," Advanced Physics Research, Jan. 2024.

[170] Z. Zuo, J. Ding, Y. Zhao, S. Du, Y. Li, X. Zhan, and H. Cui, "Enhanced optoelectronic performance on the (110) lattice plane of an mapbbr3 single crystal," The Journal of Physical Chemistry Letters, vol. 8, p. 684–689, Jan. 2017.

[171] E. M. Mozur and J. R. Neilson, "Cation dynamics in hybrid halide perovskites," Annual Review of Materials Research, vol. 51, p. 269–291, July 2021.

[172] T. Chen, B. J. Foley, B. Ipek, M. Tyagi, J. R. D. Copley, C. M. Brown, J. J. Choi, and S.-H. Lee, "Rotational dynamics of organic cations in the ch3nh3pbi3perovskite," Physical Chemistry Chemical Physics, vol. 17, no. 46, p. 31278–31286, 2015.

[173] A. Koda, H. Okabe, M. Hiraishi, R. Kadono, K. A. Dagnall, J. J. Choi, and S.-H. Lee, "Organic molecular dynamics and charge-carrier lifetime in lead iodide perovskite mapbi 3," Proceedings of the National Academy of Sciences, vol. 119, Jan. 2022.

[174] S. Meloni, T. Moehl, W. Tress, M. Franckevičius, M. Saliba, Y. H. Lee, P. Gao, M. K. Nazeeruddin, S. M. Zakeeruddin, U. Rothlisberger, and M. Graetzel, "Ionic polarization-induced current–voltage hysteresis in ch3nh3pbx3 perovskite solar cells," Nature Communications, vol. 7, Feb. 2016.

[175] A. Oranskaia, J. Yin, O. M. Bakr, J.-L. Brédas, and O. F. Mohammed, "Halogen migration in hybrid perovskites: The organic cation matters," The Journal of Physical Chemistry Letters, vol. 9, p. 5474–5480, Sept. 2018.

[176] N. Onoda-Yamamuro, T. Matsuo, and H. Suga, "Dielectric study of ch3nh3pbx3 (x = cl, br, i)," Journal of Physics and Chemistry of Solids, vol. 53, p. 935–939, July 1992.

[177] L. D. Barron, "Symmetry and chirality: Where physics shakes hands with chemistry and biology," Israel Journal of Chemistry, vol. 61, pp. 517–529, Aug. 2021.

[178] J. Mun, M. Kim, Y. Yang, T. Badloe, J. Ni, Y. Chen, C.-W. Qiu, and J. Rho, "Electromagnetic chirality: from fundamentals to nontraditional chiroptical phenomena," Light: Science and Applications, vol. 9, Sept. 2020.

[179] D. Smith, "New mechanisms for magnetic anisotropy in localised s-state moment materials," Journal of Magnetism and Magnetic Materials, vol. 1, pp. 214–225, Jan. 1976.

[180] A. Fert and P. M. Levy, "Role of anisotropic exchange interactions in determining the properties of spin-glasses," Physical Review Letters, vol. 44, pp. 1538–1541, June 1980.

[181] J. Lu, M. Li, and X. R. Wang, "Quantifying the bulk and interfacial dzyaloshinskii-moriya interactions," Physical Review B, vol. 101, Apr. 2020.

[182] W. Jiang, G. Chen, K. Liu, J. Zang, S. G. te Velthuis, and A. Hoffmann, "Skyrmions in magnetic multilayers," Physics Reports, vol. 704, pp. 1–49, Aug. 2017.

[183] W. Koshibae and N. Nagaosa, "Theory of skyrmions in bilayer systems," Scientific Reports, vol. 7, Feb. 2017.

[184] B. Göbel, I. Mertig, and O. A. Tretiakov, "Beyond skyrmions: Review and perspectives of alternative magnetic quasiparticles," Physics Reports, vol. 895, pp. 1–28, Feb. 2021.

[185] Y. Tokura and N. Kanazawa, "Magnetic skyrmion materials," Chemical Reviews, vol. 121, pp. 2857–2897, Nov. 2020.

[186] S. Muhlbauer, B. Binz, F. Jonietz, C. Pfleiderer, A. Rosch, A. Neubauer, R. Georgii, and P. Boni, "Skyrmion lattice in a chiral magnet," Science, vol. 323, pp. 915–919, Feb. 2009.

[187] C. Moreau-Luchaire, C. Moutafis, N. Reyren, J. Sampaio, C. A. F. Vaz, N. V. Horne, K. Bouzehouane, K. Garcia, C. Deranlot, P. Warnicke, P. Wohlhüter, J.-M. George, M. Weigand, J. Raabe, V. Cros, and A. Fert, "Additive interfacial chiral interaction in multilayers for stabilization of small individual skyrmions at room temperature," Nature Nanotechnology, vol. 11, pp. 444–448, Jan. 2016.

[188] A. Fert, V. Cros, and J. Sampaio, "Skyrmions on the track," Nature Nanotechnology, vol. 8, pp. 152–156, Mar. 2013.

[189] F. Büttner, B. Pfau, M. Böttcher, M. Schneider, G. Mercurio, C. M. Günther, P. Hessing, C. Klose, A. Wittmann, K. Gerlinger, L.-M. Kern, C. Strüber, C. von Korff Schmising, J. Fuchs, D. Engel, A. Churikova, S. Huang, D. Suzuki, I. Lemesh, M. Huang, L. Caretta, D. Weder, J. H. Gaida, M. Möller, T. R. Harvey, S. Zayko, K. Bagschik, R. Carley, L. Mercadier, J. Schlappa, A. Yaroslavtsev, L. L. Guyarder, N. Gerasimova, A. Scherz, C. Deiter, R. Gort, D. Hickin, J. Zhu, M. Turcato, D. Lomidze, F. Erdinger, A. Castoldi, S. Maffessanti, M. Porro, A. Samartsev, J. Sinova, C. Ropers, J. H. Mentink, B. Dupé, G. S. D. Beach, and S. Eisebitt, "Observation of fluctuation-mediated picosecond nucleation of a topological phase," Nature Materials, vol. 20, pp. 30–37, Oct. 2020.

[190] J.-V. Kim and M.-W. Yoo, "Current-driven skyrmion dynamics in disordered films," Applied Physics Letters, vol. 110, Mar. 2017.

[191] X. Gong, H. Y. Yuan, and X. R. Wang, "Current-driven skyrmion motion in granular films," Physical Review B, vol. 101, Feb. 2020.

[192] S. Tacchi, R. Troncoso, M. Ahlberg, G. Gubbiotti, M. Madami, J. Åkerman, and P. Landeros, "Interfacial dzyaloshinskii-moriya interaction in pt/cofeb films: effect of the heavy-metal thickness," Physical review letters, vol. 118, no. 14, p. 147201, 2017.

[193] R. Lavrijsen, A. Fernández-Pacheco, D. Petit, R. Mansell, J. H. Lee, and R. P. Cowburn, "Tuning the interlayer exchange coupling between single perpendicularly magnetized CoFeB layers," Applied Physics Letters, vol. 100, Jan. 2012.

[194] A. S. Silva, S. P. Sá, S. A. Bunyaev, C. Garcia, I. J. Sola, G. N. Kakazei, H. Crespo, and D. Navas, "Dynamical behaviour of ultrathin [CoFeB (tCoFeB)/pd] films with perpendicular magnetic anisotropy," Scientific Reports, vol. 11, Jan. 2021.

[195] W. Legrand, J.-Y. Chauleau, D. Maccariello, N. Reyren, S. Collin, K. Bouzehouane, N. Jaouen, V. Cros, and A. Fert, "Hybrid chiral domain walls and skyrmions in magnetic multilayers," Science Advances, vol. 4, July 2018.

[196] H. Z. Wu, B. F. Miao, L. Sun, D. Wu, and H. F. Ding, "Hybrid magnetic skyrmion," Physical Review B, vol. 95, May 2017.

[197] S. Flewett, E. Burgos-Parra, M. G. Strelow, Y. Sassi, C. Léveillé, F. Ajejas, N. Reyren, and N. Jaouen, "General treatment of off-specular resonant soft x-ray

magnetic scattering using the distorted-wave born approximation: Numerical algorithm and experimental studies with hybrid chiral domain structures," Physical Review B, vol. 103, May 2021.

[198] M. Belmeguenai, H. Bouloussa, Y. Roussigné, M. S. Gabor, T. Petrisor, C. Tiusan, H. Yang, A. Stashkevich, and S. M. Chérif, "Interface dzyaloshinskii-moriya interaction in the interlayer antiferromagnetic-exchange coupled pt/CoFeB/ru/CoFeB systems," Physical Review B, vol. 96, Oct. 2017.

[199] M. Fattouhi and M. E. Hafidi, "Computational insight on magnetic skyrmions existence in pt/CoFeB/ru/CoFeB nanodisks," Journal of Magnetism and Magnetic Materials, vol. 528, p. 167853, June 2021.

[200] R. Chen, X. Wang, H. Cheng, K.-J. Lee, D. Xiong, J.-Y. Kim, S. Li, H. Yang, H. Zhang, K. Cao, M. Kläui, S. Peng, X. Zhang, and W. Zhao, "Large dzyaloshinskii-moriya interaction and room-temperature nanoscale skyrmions in CoFeB/MgO heterostructures," Cell Reports Physical Science, vol. 2, p. 100618, Nov. 2021.

[201] Y. Zhou, R. Mansell, S. Valencia, F. Kronast, and S. van Dijken, "Temperature dependence of the dzyaloshinskii-moriya interaction in ultrathin films," Physical Review B, vol. 101, Feb. 2020.

[202] A. S. Samardak, A. V. Davydenko, A. G. Kolesnikov, A. Y. Samardak, A. G. Kozlov, B. Pal, A. V. Ognev, A. V. Sadovnikov, S. A. Nikitov, A. V. Gerasimenko, I. H. Cha, Y. J. Kim, G. W. Kim, O. A. Tretiakov, and Y. K. Kim, "Enhancement of perpendicular magnetic anisotropy and dzyaloshinskii–moriya interaction in thin ferromagnetic films by atomic-scale modulation of interfaces," NPG Asia Materials, vol. 12, July 2020.